2011

Particulate dispersion in a turbulent serpentine channel

Xin Huang
Iowa State University

Particulate dispersion in a turbulent serpentine channel

by

Xin Huang

A dissertation submitted to the graduate faculty

in partial fulfillment of the requirements for the degree of

DOCTOR OF PHILOSOPHY

Major: Aerospace Enginnering

Program of Study Committee:

Paul Durbin, Major Professor

Glenn Luecke

Alric Rothmayer

Shankar Subramaniam

Zhi Jian Wang

Iowa State University

Ames, Iowa

2011

TABLE OF CONTENTS

LIST OF TABLES v

LIST OF FIGURES vi

ACKNOWLEDGEMENTS xiv

ABSTRACT xv

CHAPTER 1. INTRODUCTION 1

1.1 Motivation 1

1.2 CFD Modeling of Multiphase Flows 2

1.2.1 Fluid Phase Simulation 2

1.2.2 Particle Phase Simulation 3

1.2.3 Research Review 4

1.3 Thesis Organization 6

CHAPTER 2. NUMERICAL METHODOLOGIES 7

2.1 DNS Solver for the Fluid Phase 7

2.1.1 Governing Equations 7

2.1.2 Spatial and Temporal Discretization 8

2.1.3 Fractional Step Algorithm 10

2.1.4 Poisson Equation 11

2.1.5 Boundary Conditions 11

2.1.6 Grid Resolution 13

2.1.7 Validation 13

2.2 LPT Method for the Particle Phase 15

2.2.1 Equations of Motion 16

2.2.2 Stokes Number . . . 18
2.2.3 Time Integration and Velocity Interpolation . . . 18
2.2.4 Boundary Conditions . . . 21
2.2.5 Estimation of Surface Erosion . . . 22
2.2.6 Parallelization Strategy . . . 23
2.2.7 Verification . . . 23
2.3 Parallel Performance . . . 25
2.4 Summary . . . 26

CHAPTER 3. PARTICLE MOTION IN A PLANE TURBULENT CHANNEL . . . 28

3.1 Fluid Phase in a Plane Turbulent Channel . . . 28
3.2 Particle Phase in a Plane Turbulent Channel . . . 30
3.2.1 Particle Properties . . . 30
3.2.2 Initialization . . . 31
3.2.3 Tracking Time Step . . . 31
3.2.4 Instantaneous Distribution and Mean Concentration . . . 33
3.2.5 Velocity Statistics . . . 34
3.2.6 Turbophoresis . . . 35
3.3 Summary . . . 36

CHAPTER 4. PARTICLE MOTION IN A U-SHAPED TURBULENT CHANNEL . . . 44

4.1 Particle Distribution in the Mean Flow . . . 44
4.2 Particle Distribution in the Turbulent Flow . . . 49
4.3 Grid Resolution and Time Convergence Study . . . 56
4.4 Particle Velocity in the Turbulent Flow . . . 62
4.5 Particle-Wall Collision Modeling . . . 78
4.6 Particle Accumulation adjacent to Channel Walls . . . 86
4.7 Surface Erosion on Channel Walls . . . 93

4.8 Particle Preferential Distribution in the Spanwise Direction 102
4.9 Summary 103
CHAPTER 5. CONCLUSION 114
5.1 Conclusion 114
5.2 Suggestion on Future Work 114
BIBLIOGRAPHY 115

LIST OF TABLES

Table 3.1 Particle Properties 31

Table 4.1 The maximum fluid phase turbophoretic force and the corresponding centrifugal acceleration at Stations 2, 3 and 4. 91

LIST OF FIGURES

Figure 2.1 Computational cell with staggered grid. 9

Figure 2.2 Periodic boundary condition in the streamwise direction for the fluid phase. 12

Figure 2.3 Geometry of the U-shaped channel. 13

Figure 2.4 A spanwise cross-section of the U-shaped channel. 14

Figure 2.5 Instantaneous spanwise vorticities in a spanwise cross-section. 15

Figure 2.6 Mean velocity vectors in the U-shaped channel. 15

Figure 2.7 The streamwise velocity component of the fluid at Stations 1, 2, 3, 4 and 5 in the U-shaped channel. d represents distance from inner wall, with 0 being inner wall and 2 being outer wall 16

Figure 2.8 Skin friction coefficient in the U-shaped channel. 17

Figure 2.9 Quadrilateral to square mapping. 20

Figure 2.10 Periodic boundary condition in the streamwise direction for the particle phase. 22

Figure 2.11 Analytical solutions and numerical simulations of particle trajectories in a steady velocity field with a simplified drag coefficient. 24

Figure 2.12 Speedup of the DNS solver. *npx* and *npy* are the numbers of processors in the streamwise and wall-normal directions, respectively. 26

Figure 2.13 Speedup of the LPT module. *npx* and *npy* are the numbers of processors in the streamwise and wall-normal directions, respectively. 27

Figure 3.1 Geometry of the plane channel. 29

Figure 3.2 Fluid mean streamwise velocity in the plane turbulent channel ($Re_\tau = 180$). 29

Figure 3.3 Fluid root mean square velocity fluctuations in the plane turbulent channel ($Re_\tau = 180$). 30

Figure 3.4 Particle maximum concentration in the plane turbulent channel at successive time intervals, obtained with different tracking time steps. ($St^+ = 1.45$) 32

Figure 3.5 Particle mean concentration across the half channel height in the plane turbulent channel, obtained with different tracking time steps. ($St^+ = 1.45$) 33

Figure 3.6 Particle root mean square velocity fluctuations across the half channel height in the plane turbulent channel, obtained with different tracking time steps. ($St^+ = 1.45$) 37

Figure 3.7 Particle distribution after 180 flow through times in the plane turbulent channel. Particles are projected onto a spanwise cross section. $St^+ = 1.45, 5.79, 11.57, 23.14, 34.71, 46.29, 57.86, 69.43$ (plots a-h) 38

Figure 3.8 Particle mean concentration across the half channel height in the plane turbulent channel. 39

Figure 3.9 Particle mean streamwise velocity across the half channel height in the plane turbulent channel. 40

Figure 3.10 Particle root mean square velocity fluctuations in the streamwise direction across the half channel height in the plane turbulent channel. . . . 41

Figure 3.11 Particle root mean square velocity fluctuations in the wall-normal direction across the half channel height in the plane turbulent channel. . 42

Figure 3.12 Particle root mean square velocity fluctuations in the spanwise direction across the half channel height in the plane turbulent channel. 42

Figure 3.13 Particle turbophoretic force across the half channel height in the plane turbulent channel. 43

Figure 3.14 Particle turbophoretic velocity across the half channel height in the plane turbulent channel. 43

Figure 4.1 Sample streamlines in the mean flow inside the U-shaped channel. . . . 45

Figure 4.2 Sample trajectories of particles in the mean flow inside the U-shaped channel. $St_b = 0.125, 0.5, 1, 2, 3, 4, 5, 6$ (plots a-h) 47

Figure 4.3 Equilibrium distribution of particles in the mean flow inside the U-shaped channel. $St_b = 0.125, 0.5, 1, 2, 3, 4, 5, 6$ (plots a-h) 48

Figure 4.4 Sample trajectories of particles in the DNS turbulent flow inside the U-shaped channel. $St_b = 0.125, 0.5, 1, 2, 3, 4, 5, 6$ (plots a-h) 52

Figure 4.5 Instantaneous distribution of particles in the DNS turbulent flow inside the U-shaped channel. $St_b = 0.125, 0.5, 1, 2, 3, 4, 5, 6$ (plots a-h) 53

Figure 4.6 Contours of particle mean concentration in the DNS turbulent flow inside the U-shaped channel. $St_b = 0.125, 0.5, 1, 2, 3, 4, 5, 6$ (plots a-h) . . 54

Figure 4.7 Particle mean concentration profiles in logarithm in the DNS turbulent flow inside the U-shaped channel. $St_b = 0.125, 0.5, 1, 2, 3, 4, 5, 6$ (plots a-h) 55

Figure 4.8 Relative standard deviations of particle mean concentration over 5 flow through times. ($St_b = 0.5$) 57

Figure 4.9 Relative standard deviations of particle mean concentration over 8 flow through times. ($St_b = 0.5$) 58

Figure 4.10 Particle mean concentration at the entrance on MESH-C1, MESH-C2, MESH-C3 and MESH-C4. d represents distance from inner wall, with 0 being inner wall and 2 being outer wall. ($St_b = 0.5$) 59

Figure 4.11 Particle mean streamwise velocity at the entrance on MESH-C1, MESH-C2, MESH-C3 and MESH-C4. d represents distance from inner wall, with 0 being inner wall and 2 being outer wall. ($St_b = 0.5$) 60

Figure 4.12 Particle mean concentration at the entrance averaged over 12, 24 and 48 flow through times. d represents distance from inner wall, with 0 being inner wall and 2 being outer wall. ($St_b = 0.5$) 60

Figure 4.13 Particle mean streamwise velocity at the entrance averaged over 12, 24 and 48 flow through times. d represents distance from inner wall, with 0 being inner wall and 2 being outer wall. ($St_b = 0.5$) 61

Figure 4.14 Particle and fluid mean velocity vectors in the DNS turbulent flow inside the U-shaped channel. $St_b = 0.125, 0.5, 1, 2, 3, 4, 5, 6$ (plots a-h) 68

Figure 4.15 Particle mean velocity component U^+ contour in the DNS turbulent flow inside the U-shaped channel. $St_b = 0.125, 0.5, 1, 2, 3, 4, 5, 6$ (plots a-h) 69

Figure 4.16 Particle mean velocity component V^+ contour in the DNS turbulent flow inside the U-shaped channel. $St_b = 0.125, 0.5, 1, 2, 3, 4, 5, 6$ (plots a-h) 70

Figure 4.17 Contours of fluid mean velocity components (U^+, V^+) and fluid phase turbulent kinetic energy (tke) in the DNS turbulent flow inside the U-shaped channel. 71

Figure 4.18 Contour lines of particle streamwise velocity component U^+ superimposed on the flooded contour of particle concentration in the DNS turbulent flow inside the U-shaped channel. $St_b = 3, 6$ (plots e,h) 72

Figure 4.19 Particle mean streamwise velocity profiles at the exit of the curved section in the DNS turbulent flow inside the U-shaped channel. $St_b = 0.125, 0.5, 1, 2, 3, 4, 5, 6$ (plots a-h) 73

Figure 4.20 Particle mean streamwise velocity profiles at the entrance in the DNS turbulent flow inside the U-shaped channel. $St_b = 0.125, 0.5, 1, 2, 3, 4, 5, 6$ (plots a-h) 74

Figure 4.21 Particle mean streamwise velocity profiles at the entrance of the curved section in the DNS turbulent flow inside the U-shaped channel. $St_b = 0.125, 0.5, 1, 2, 3, 4, 5, 6$ (plots a-h) 75

Figure 4.22 Particle mean streamwise velocity profiles at the middle position of the curved section in the DNS turbulent flow inside the U-shaped channel. $St_b = 0.125, 0.5, 1, 2, 3, 4, 5, 6$ (plots a-h) 76

Figure 4.23 Particle phase turbulent kinetic energy (tke) contour in the DNS turbulent flow inside the U-shaped channel. $St_b = 0.125, 0.5, 1, 2, 3, 4, 5, 6$ (plots a-h) 77

Figure 4.24 Contours of particle mean concentration in the U-shaped channel with inelastic reflection. $St_b = 0.125, 0.5, 1, 2, 3, 4, 5, 6$ (plots a-h) 80

Figure 4.25 Particle mean concentration profiles in logarithm in the U-shaped channel with inelastic reflection. $St_b = 0.125, 0.5, 1, 2, 3, 4, 5, 6$ (plots a-h) . 81

Figure 4.26 Particle concentration on SURFACE-1 with elastic and inelastic reflection at $St_b = 0.125$. 82

Figure 4.27 Particle concentration on SURFACE-1 with elastic and inelastic reflection at $St_b = 0.5$. 82

Figure 4.28 Particle concentration on SURFACE-1 with elastic and inelastic reflection at $St_b = 1$. 83

Figure 4.29 Particle concentration on SURFACE-1 with elastic and inelastic reflection at $St_b = 2$. 83

Figure 4.30 Particle concentration on SURFACE-1 with elastic and inelastic reflection at $St_b = 4$. 84

Figure 4.31 Particle concentration on SURFACE-1 with elastic and inelastic reflection at $St_b = 6$. 84

Figure 4.32 SURFACE-1 in the S-shaped channel. 85

Figure 4.33 Fluid phase turbophoretic force across the channel width in the plane channel and at Stations 4, 1 and 2 in the U-shaped channel. y represents distance from lower wall, with 0 being lower wall and 2 being upper wall. 89

Figure 4.34 Turbophoretic velocity of $St_b = 0.125$ and the fluid mean convection velocity in the wall-normal direction at $\Delta y^+ = 23$ away from the upper wall in the straight section of the S-shaped channel, with $S/\pi = 4.0$ being the entrance and $S/\pi = 6.0$ being the exit. 90

Figure 4.35 Fluid phase turbophoretic force across the channel width in the plane channel and at Stations 2, 3 and 4 in the U-shaped channel. y represents distance from inner wall, with 0 being inner wall and 2 being outer wall 91

Figure 4.36 Fluid mean streamwise velocity at $\Delta y^+ = 0.47$ away from SURFACE-1. 92

Figure 4.37 Erosion rate along the channel walls. $St_b = 0.125, 0.5, 1, 2, 3, 4, 5, 6$ (plots a-h) 96

Figure 4.38 Erosion rate $(ER - t)$, collision rate $(N - t)$, incident angle (α) and impact velocity (V^+_{imp}) at $\alpha \leq 15°$ (diamond) and at $\alpha > 15°$ (filled square) along SURFACE-1. $(St_b = 0.5)$ 97

Figure 4.39 Erosion rate $(ER - t)$, collision rate $(N - t)$, incident angle (α) and impact velocity (V^+_{imp}) at $\alpha \leq 15°$ (diamond) and at $\alpha > 15°$ (filled square) along SURFACE-1. $(St_b = 2.0)$ 98

Figure 4.40 Erosion rate $(ER - t)$, collision rate $(N - t)$, incident angle (α) and impact velocity (V^+_{imp}) at $\alpha \leq 15°$ (diamond) and at $\alpha > 15°$ (filled square) along SURFACE-1. $(St_b = 4.0)$ 99

Figure 4.41 Erosion rate $(ER - t)$, collision rate $(N - t)$, incident angle (α) and impact velocity (V^+_{imp}) at $\alpha \leq 15°$ (diamond) and at $\alpha > 15°$ (filled square) along SURFACE-1. $(St_b = 6.0)$ 100

Figure 4.42 Erosion rate along SURFACE-1 assuming elastic reflection (diamond) and inelastic reflection (filled square). $St_b = 0.5, 2, 4, 6$ (plots b-h) . . . 101

Figure 4.43 Particle instantaneous distribution inside the S-shaped channel assuming elastic (top plot) and inelastic (bottom plot) particle-wall collision. $(St_b = 0.5)$ 104

Figure 4.44 Particle instantaneous distribution inside the S-shaped channel assuming elastic (top plot) and inelastic (bottom plot) particle-wall collision. ($St_b = 2.0$) 105

Figure 4.45 Particle instantaneous distribution inside the S-shaped channel assuming elastic (top plot) and inelastic (bottom plot) particle-wall collision. ($St_b = 4.0$) 106

Figure 4.46 Particle instantaneous distribution inside the S-shaped channel assuming elastic (top plot) and inelastic (bottom plot) particle-wall collision. ($St_b = 6.0$) 107

Figure 4.47 Tangential components of fluid velocity fluctuations along planes at $y^+ = 5$ from the inner and outer walls of the U-shaped channel. 108

Figure 4.48 Fluid streamwise velocity fluctuations in the $x-z$ plane at $y^+ = 5$ above the lower wall in the straight section. The dark grey color represents low-speed regions. 108

Figure 4.49 Particles in the proximity of the lower wall ($0 \leq y^+ \leq 5$) superimposed on the fluid streamwise velocity fluctuations at $y^+ = 5$ assuming inelastic particle-wall collision. ($St_b = 0.5$) 109

Figure 4.50 Particles in the proximity of the lower wall ($0 \leq y^+ \leq 5$) superimposed on the fluid streamwise velocity fluctuations at $y^+ = 5$ assuming inelastic particle-wall collision. ($St_b = 2.0$) 109

Figure 4.51 Particles in the proximity of the lower wall ($0 \leq y^+ \leq 5$) superimposed on the fluid streamwise velocity fluctuations at $y^+ = 5$ assuming inelastic particle-wall collision. ($St_b = 4.0$) 110

Figure 4.52 Particles in the proximity of the lower wall ($0 \leq y^+ \leq 5$) superimposed on the fluid streamwise velocity fluctuations at $y^+ = 5$ assuming inelastic particle-wall collision. ($St_b = 6.0$) 110

Figure 4.53 Vorticity magnitude at $y^+ = 5$ and $y^+ = 50$ from the channel walls of the S-shaped channel. The contour level is set up independently to visualize the vortex structures. 111

Figure 4.54 Channel wall erosion rate over 1/6 flow through times assuming elastic particle-wall collision. $St_b = 0.5, 2, 4, 6$ (plots b-h) 112

Figure 4.55 Channel wall erosion rate over 12 flow through times assuming elastic particle-wall collision. $St_b = 0.5, 2, 4, 6$ (plots b-h) 113

ACKNOWLEDGEMENTS

First and foremost, I would like to express my sincere appreciation to Dr. Paul Durbin for his guidance and patience throughout this research. I would also like to thank my committee members Dr. Glenn Luecke, Dr. Alric Rothmayer, Dr. Shankar Subramaniam and Dr. Zhi Jian Wang for their effort and time. I would additionally like to thank Dr. Tom Shih for serving on my committee during the first four years. Last, but not the least, I would like to thank my parents, other family members and my friends for their love and support.

ABSTRACT

In a turbulent channel flow, an initially uniform distribution of particles evolves into a non-uniform distribution. In a straight turbulent channel, both turbulent eddies in the core region and turbophoresis in the viscous sublayer are responsible for the non-uniform distribution. In a curved channel, the dominant cause is particle inertia, but turbulent diffusion still plays an important role. Particulate dispersion in an infinite serpentine channel is studied using direct numerical simulation coupled with Lagrangian particle tracking. Particle Stokes numbers range from 0.125 to 6.0. Above the lowest Stokes number, particles form into a plume that leaves the inner bend at the entrance of the curved section. Turbulence then disperses the plume. Heavier particles move across the channel and reflect from the outer bend, forming a high concentration layer near the outer wall. The heaviest particles reflect again from the wall and are dispersed across the channel by turbulence. An empirical formula is used to analyze the propensity for particle impacts to erode the channel walls. The region of the maximum erosion is neither where the maximum number of impacts is the largest nor where the impact velocity is the highest. The impact angle determines where the erosion is the largest. Instantaneous distributions show that particles with small Stokes numbers accumulate in streaks near the wall, but particles with large Stokes numbers tend to form puffs in the middle of the channel and have less tendency to cluster into wall streaks.

CHAPTER 1. INTRODUCTION

1.1 Motivation

Turbulent flows that contain solid particles are commonly encountered in nature (e.g. air pollution and volcanic eruptions) and engineering applications (e.g. fluidized beds and petroleum transportation). In the past decade, computational fluid dynamics (CFD) has been increasingly used in the design of systems involving particle-laden flows [Metally *et al.* (1995), Huang *et al.* (2003), Apte *et al.* (2003), Mazur *et al.* (2004)]. For example, in the pipeline systems for petroleum transportation, sand particles are suspended in the petroleum fluids. These particles impact the pipeline systems and remove material from them, which may result in significant wear of the pipeline systems. To avoid the leakage that may be caused by erosion, the motion of suspended particles is simulated using CFD, along with which the surface erosion rate can be estimated.

Usually, erosion is most severe where the flow is redirected, such as in the bends. The fluid streamlines follow curved trajectories along which the pressure gradient toward the center of the curvature balances the centrifugal acceleration. Solid particles with finite inertia are not subjected to the radial fluid pressure gradient; hence, they depart from the fluid streamlines and impact the outer walls. The impact due to the particle inertia is called as direct impact in Edwards *et al.* (2001). Almost all the flows that carry particles are turbulent flows. In turbulent flows, turbulent eddies can transport particles toward walls, and the impact due to the turbulent dispersion is called random impingement. The direct impact may be the dominant cause of the wear erosion, but the influence of the random impingement cannot be ignored. The relative influence of the flow redirection and turbulent dispersion on particle motion is often uncertain and needs further investigation.

This thesis documents the CFD simulation results of particulate motion in an infinite serpentine channel. The purpose of this thesis is to investigate the roles of particle inertia, turbophoresis, wall impact and random turbulent convection on particle distribution. The results may be used in the future development and validation of particle-laden flow modeling.

1.2 CFD Modeling of Multiphase Flows

The CFD simulations of particle-laden flows (or, more generally, multiphase flows) are classified into two groups: Eulerian-Eulerian and the Eulerian-Lagrangian. The two groups differ in the treatment of the particle phase. In the Eulerian-Eulerian approach, the particle phase is considered as one or more continua, and the velocity of the particle phase at each mesh point is solved. In the Eulerian-Lagrangian approach, particles are treated as individual objects, and the movement of each particle is tracked. Despite the difference in the particle-phase modeling, the fluid phase is treated as a continuum in both approaches.

1.2.1 Fluid Phase Simulation

The motion of fluids is simulated by solving the Navier-Stokes equations, including the mass conservation equation, with specific initial and boundary conditions. For turbulent flows, the Navier-Stokes equations are three-dimensional and unsteady, which can only be solved numerically. There are three major numerical methods: RANS (Reynolds-Averaged Navier-Stokes), LES (Large Eddy Simulation) and DNS (Direct Numerical Simulation). In RANS, an ensemble version of Navier-Stokes equations is solved for the mean flow field, and the correlations of turbulent fluctuations are modeled. In LES, the small turbulent fluctuations are modeled but the large turbulent eddies are resolved. In DNS, the Navier-Stokes equations are solved without any model, and the entire range of turbulent fluctuations is resolved. To capture the turbulence at all spatial and time scales, find grid resolutions and small time steps are required, which makes DNS computational expensive. The direct numerical simulation may not be feasible in engineering applications, but it is useful to provide benchmark data for the development and validation of models in RANS and LES.

The turbulent flow in an infinite serpentine channel was previously investigated using direct numerical simulation by Laskowski (2005). A simulation using RANS with 2-layer $k-\epsilon$ model was also carried out, and large disparity in turbulent kinetic energy was observed between the RANS and DNS simulations. No simulation was conducted using LES, but the value of the turbulent kinetic energy from LES would fall in between those from the DNS and RANS simulations.

It is well known that turbulence plays an important role on particle dispersion in multiphase flows. In wall-bounded turbulent flows, particles have a tendency to move toward the wall, and turbophoresis is responsible for the deposition of intermediate-sized particles in the near wall region [Caporaloni *et al.* (1975)]. The simulation results of particle motion in turbulent channel flows depend largely on the range of velocity fluctuations that are resolved in the fluid phase. The previous study of particle motion in turbulent channel flows showed that LES simulations underestimate particle deposition velocity due to the lack of subgrid fluctuations [Kuerten and Vreman (2005), Marchioli *et al.* (2008a)]. In this thesis, direct numerical simulation is adopted to fully resolve the turbulent fluctuations.

1.2.2 Particle Phase Simulation

When the fluid phase is solved using direct numerical simulation, the Lagrangian particle tracking method is commonly adopted for the particle phase. The movement of each individual particle is tracked, and particle motion is governed by Newton's second law.

In a viscous fluid, particles may be subjected to a variety of forces, and the most important forces are Stokes drag, added mass, Basset force, Magnus lift and Saffman lift [Crowe *et al.* (1998)]. The Stokes drag is the viscous resistance exerted by the fluid on a particle that moves faster or slower than its surrounding fluid. The added mass and the Basset force are associated with the acceleration and deceleration of particles. When a particle moves ahead of or behind the fluid, it will expel the surrounding fluid. The added mass is caused by the inertia of the expelled fluid, and the Basset force is caused by the temporal delay in boundary layer development. Both the Magnus and Saffman lift forces are due to particle rotation. The Magnus lift is caused by the pressure difference on particle surface when a particle is forced to

rotate in a uniform velocity flow field. The Saffman lift accounts for particle rotation that is introduced by the velocity gradient in the carrier fluid. Other possible forces include pressure gradient forces and gravity. The importance of each force depends on the flow and some of them may be neglected in the simulation.

The interaction between the carrier fluid and the suspended particles is always mutual, thus the fluid phase may be altered due to the presence of particles. When particle loading is very low and particle size is small, the influence of particles on the carrier fluid is negligible. The simulation of the dilute particle-laden flow is classified as one-way coupling, in which the governing equations of the fluid phase are unchanged. As particle loading increases, the forces of particles on the carrier fluid cannot be neglected. In the simulation, the governing equations of the fluid phase are modified to include forces from particles, and the coupling is two-way. In very dense particle-laden flows, the interaction between particles becomes prominent, which may affect the motion of both the particle and fluid phases. In addition to the mutual interaction between the fluid and particle phase, particle-particle collisions are modeled, and the simulation is called as four-way coupling. In general, the degree of phase coupling is determined by the volume fraction of particles. According to Elghobashi (1991), one-way coupling is appropriate when the volume fraction is smaller than 10^{-6} and four-way coupling is necessary when the volume fraction is larger than 10^{-3}.

1.2.3 Research Review

The first multiphase flow simulation using direct numerical simulation coupled with the Lagrangian particle tracking method was performed by Riley and Patterson (1974). The motion of particles in a decaying isotropic turbulence was simulated; and one purpose of the study was to investigate the Lagrangian velocity autocorrelation coefficients which were difficult to obtain from experiments and Eulerian-Eulerian simulations. Since then, many DNS simulations of particle motion in isotropic turbulent flows have been performed to explore the physical mechanisms, to provide data for model validation, and to give guidance on experiment measurements [Elghobashi and Truesdell (1992), Yeung (1994), Malik and Vassilicos (1999), Sundaram and Collins (1997), Salazar *et al.* (2008)]. In isotropic turbulent flows, inertia particles preferen-

tially accumulate in regions of low vorticity and high strain rate [Maxey (1987), Squires and Eaton (1991)].

In turbulent channel flows, the phenomenon of particle preferential concentration was also observed near the centerline in experiments [Fessler *et al.* (1994)] and in simulations [Haarlem *et al.* (1998)]. Besides this preferential concentration phenomenon, particles have a tendency to accumulate near the wall. In the core region, the large turbulent eddies transport particles toward the viscous sublayer. In the viscous sublayer, particle motion may be dominated by different mechanism depending on particle size (or, more precisely, particle relaxation time). When particles are heavy, they acquire enough momentum from the large eddies in the core region to penetrate the viscous sublayer. Very small particles are dominated by Brownian diffusion in the viscous sublayer, and no significant deposition occurs. For particles of intermediate size, their deposition velocity increases rapidly with particle relaxation time. The transport mechanism is recognized as turbophoresis, which is driven by the gradient of root-mean-square velocity fluctuations in the wall-normal direction. In the simulation using the Eulerian-Eulerian approach, the turbophoretic force on particles needs to be modeled [Guha (1997), Young and Leeming (1997)]. In the direct numerical simulation coupled with the Lagrangian particle tracking method, the influence of turbophoresis is captured implicitly [McLaughlin (1989), Brooke *et al.* (1992), Brooke *et al.* (1994)].

After particles accumulate in the viscous sublayer, they further gather into low-speed streaks where the fluid velocity is lower than the mean streamwise velocity [Rashidi *et al.* (1990), Pedinotti *et al.* (1992)]. The formation of particle streaks is associated with the elongated turbulent structures in the viscous sublayer, which has been extensively investigated using direct numerical simulation [Rouson and Eaton (2001), Marchioli and Soldati (2002), Narayanan *et al.* (2003), Picciotto *et al.* (2003), Sardina *et al.* ((2011)]. Direct numerical simulation coupled with Lagrangian particle tracking has proved to be useful in the study of particle preferential concentration in plane turbulent channel flows, and also in straight turbulent pipe flows [Marchioli *et al.* (2003)].

In engineering applications, the straight pipes or channels are usually connected with elbows or bends. In the bend where the flow is redirected, particles accumulate near the outer side

due to inertia, and the accumulated particles may form rope-like structures. This preferential concentration phenomenon is called particle roping, and it can cause various issues in pneumatic conveying systems, such as uneven coal injection to the burners or preferential surface erosion. In addition to the experimental study, CFD simulation has been used to investigate particle distribution and surface erosion in elbows and bends [Yilmaz and Levy (2001), Chen *et al.* (2004), Kuan *et al.* (2007)]. However, there are some aspects that need further study. First, despite the large number of investigations in 90° bends and elbows, only a few simulations in 180° bends were performed [Hidayat and Rasmuson (2005), El-Behery *et al.* (2009)]. Second, almost all of the simulations used RANS for the fluid phase, and discrepancies were observed between simulation results and experimental data [Njobuenwu *et al.* (2009)].

1.3 Thesis Organization

With the advance in computational capacity, it is now possible to apply direct numerical simulation for particle-laden flows in more complex geometry than plane channels. For example, Laskowski (2005) carried out the direct numerical simulation of flow in an infinite serpentine channel, which consists of straight channels and 180° bends. In this thesis, the particle-laden flow in the same infinite serpentine channel is investigated using direction numerical simulation coupled with Lagrangian particle tracking.

The remainder of this thesis is organized as follows. In Chapter 2 are the numerical methodologies used in the direct numerical simulation and the Lagrangian particle tracking code. Chapter 3 presents the simulation results of particle motion in a plane channel, which was carried out for the purpose of validation. The simulation results of particle motion in the infinite serpentine channel are presented and discussed in Chapter 4. In Chapter 5 are the concluding remarks and suggestions for future work.

CHAPTER 2. NUMERICAL METHODOLOGIES

The numerical methodologies adopted are direct numerical simulation for the fluid phase and Lagrangian particle tracking for the particle phase. The direct numerical simulation (DNS) code was developed and validated by Wu *et al.* (1999) and Zaki and Durbin (2005), thus only a brief overview of the DNS code is presented in the first section of this chapter. In this project, a parallel Lagrangian particle tracking (LPT) module was developed and implemented into the DNS code. The details of the development and implementation are given in the second section. The last section of this chapter discusses the parallel efficiency of the DNS solver and the LPT module.

2.1 DNS Solver for the Fluid Phase

The DNS solver was developed for the three dimensional unsteady incompressible flow. The governing equations are given in the primitive variable form, followed by the methods of spatial and temporal discretization and the fractional step algorithm. Boundary conditions applied on a U-shaped channel are explained. Simulation results are presented and compared with those from Laskowski (2005), in which the same simulation was carried out in an S-shaped channel.

2.1.1 Governing Equations

For the three dimensional incompressible flow of Newtonian fluid, the pressure and three velocity components are solved from a mass conservation equation and three momentum conservation equations. In the channel flow, these four equations are usually normalized with the bulk velocity u_b and the half channel height δ. The non-dimensional equations in the index

form are written as

$$\frac{\partial u_i}{\partial x_i} = 0 \tag{2.1}$$

$$\frac{\partial u_i}{\partial t} + u_j \frac{\partial u_i}{\partial x_j} = -\frac{\partial p}{\partial x_i} + \frac{1}{Re_b}\frac{\partial}{\partial x_j}\mu\left(\frac{\partial u_i}{\partial x_j} + \frac{\partial u_j}{\partial x_i}\right) \tag{2.2}$$

where $Re_b = \rho u_b \delta/\mu$ is the bulk velocity Reynolds number.

2.1.2 Spatial and Temporal Discretization

The governing equations are solved with the fractional step method on a non-orthogonal curvilinear grid. The spatial discretization is based on the staggered-grid finite volume method developed by Rosenfeld *et al.* (1991). The primitive variables are volume fluxes across each face of the computational cell and the pressure at the center of the computational cell, as shown in Figure 2.1. The volume flux U^q $(q = \xi, \eta, \zeta)$ is defined as

$$U^\xi = \mathbf{S}^\xi \cdot \mathbf{u}, \quad U^\eta = \mathbf{S}^\eta \cdot \mathbf{u}, \quad U^\zeta = \mathbf{S}^\zeta \cdot \mathbf{u} \tag{2.3}$$

where $\mathbf{u}$ is the Cartesian velocity and $\mathbf{S}^q$ $(q = \xi, \eta, \zeta)$ is the area tensor. The area tensor is defined as

$$\mathbf{S}^\xi = \frac{\partial \mathbf{r}}{\partial \eta} \times \frac{\partial \mathbf{r}}{\partial \zeta}, \quad \mathbf{S}^\eta = \frac{\partial \mathbf{r}}{\partial \zeta} \times \frac{\partial \mathbf{r}}{\partial \xi}, \quad \mathbf{S}^\zeta = \frac{\partial \mathbf{r}}{\partial \xi} \times \frac{\partial \mathbf{r}}{\partial \eta} \tag{2.4}$$

Here $\mathbf{r}(\xi, \eta, \zeta)$ is the coordinate in the curvilinear system [Rosenfeld *et al.* (1991)].

Integrating the governing equations (2.1) and (2.2) over a control volume V gives

$$\iint_{\mathbf{S}} \mathbf{u} \cdot d\mathbf{S} = 0 \tag{2.5}$$

$$\iiint_V \frac{\partial \mathbf{u}}{\partial t} dV = \iint_{\mathbf{S}} \mathbf{T} \cdot d\mathbf{S}, \tag{2.6}$$

where

$$\mathbf{T} = -\mathbf{u}\mathbf{u} - p\mathbf{I} + \frac{1}{Re_b}[\nabla \mathbf{u} + \nabla \mathbf{u}^T]. \tag{2.7}$$

The surface integrals are the sum over each face of the control volume. Equation (2.5) is approximated with volume fluxes as

$$U_e^\xi - U_w^\xi + U_s^\eta - U_n^\eta + U_b^\zeta - U_f^\zeta = 0 \tag{2.8}$$

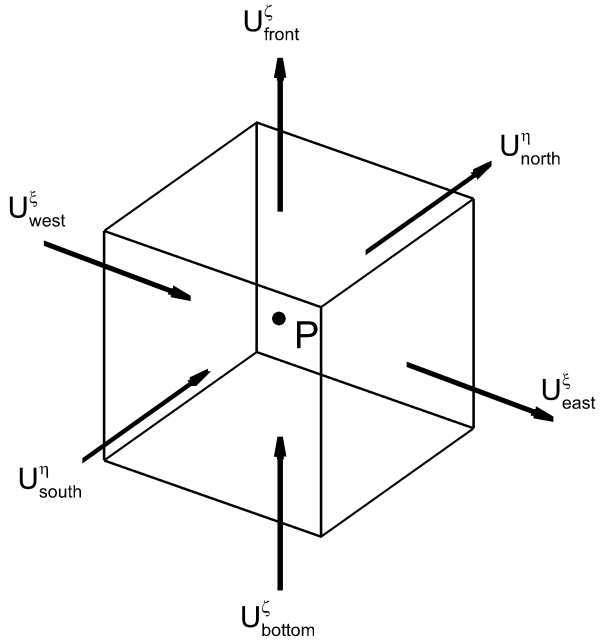

Figure 2.1 Computational cell with staggered grid.

An approximation of Equation (2.6) over an arbitrary control volume V is

$$V\frac{\partial \mathbf{u}}{\partial t} = \sum_l \mathbf{S}^l \cdot \mathbf{T} = \mathbf{F} \tag{2.9}$$

where $\mathbf{F}$ is the total flux through the control volume. On the staggered mesh, the momentum conservation equations in the ξ, η and ζ directions are approximated over different control volumes with their central nodes at U^ξ, U^η and U^ζ respectively. Multiplying both sides of Equation (2.9) by $\mathbf{S}^q_{ccp}$ $(q = \xi, \eta, \zeta)$, which are the area tensors at the center of the cells, the equation can be rewritten in terms of volume flux U^q $(q = \xi, \eta, \zeta)$:

$$V^q\frac{\partial U^q}{\partial t} = \mathbf{S}^q_{ccp} \cdot \mathbf{S}^l \cdot \mathbf{T} = H^q(U^k) + R^q(p) + D^q_{imp}(U^k) + D^q_{exp}(U^k) \tag{2.10}$$

where $H^q(U^k)$ is the nonlinear convection term

$$H^q(U^k) = -\mathbf{S}^q_{ccp} \cdot \sum_l \mathbf{S}^l \cdot \mathbf{uu} \tag{2.11}$$

and $R^q(p)$ is the pressure term

$$R^q(p) = -\mathbf{S}^q_{ccp} \cdot \sum_l \mathbf{S}^l \cdot p\mathbf{I} \tag{2.12}$$

The diffusion term $D^q(U^k) = \mathbf{S}^q_{ccp} \cdot \sum_l \mathbf{S}^l \cdot [\nabla \mathbf{u} + \nabla \mathbf{u}^T]/Re_b$ is split into an explicit term D^q_{exp} which consists of $\partial^2/\partial\xi^2 + \partial^2/\partial\eta^2 + \partial^2/\partial\zeta^2$ and an implicit term D^q_{imp} which consists of the rest. The Cartesian velocity $\mathbf{u}$ in H^q and D^q can be recovered from the volume fluxes using

$$\mathbf{u} = \mathbf{S}_\xi U^\xi + \mathbf{S}_\eta U^\eta + \mathbf{S}_\zeta U^\zeta \tag{2.13}$$

where $\mathbf{S}_m$ $(m = \xi, \eta, \zeta)$ is the reciprocal of the area tensor $\mathbf{S}^q$ $(q = \xi, \eta, \zeta)$ with $\mathbf{S}_m \cdot \mathbf{S}^q = \delta_{mq}$(Kronecker delta). The velocity gradient is evaluated with

$$\nabla \mathbf{u} = \frac{1}{V} \iint_{\mathbf{S}} \mathbf{u} d\mathbf{S} \tag{2.14}$$

A 2nd-order explicit Adams-Bashforth scheme is used for $H^q(U^k)$ and $D^q_{exp}(U^k)$; Euler implicit is invoked for $R^q(p)$; and Crank-Nicolson is applied to $D^q_{imp}(U^k)$. The temporal discretization of Equation (2.10) is

$$\begin{aligned} V^q \frac{(U^q)^{n+1} - (U^q)^n}{\Delta t} &= \frac{1}{2}[3H^q(U^k)^n - H^q(U^k)^{n-1}] + R^q(p)^{n+1} + \frac{1}{2}[3D^q_{exp}(U^k)^n - D^q_{exp}(U^k)^{n-1}] \\ &\quad + \frac{1}{2}[D^q_{imp}(U^k)^{n+1} + D^q_{imp}(U^k)^n] \end{aligned} \tag{2.15}$$

2.1.3 Fractional Step Algorithm

Equations (2.8) and (2.15) are solved using the fractional step method, which involves the following three sets of equations:

$$\begin{aligned} V^q \frac{\hat{U}^q - (U^q)^n}{\Delta t} &= \frac{1}{2}[3H^q(U^k)^n - H^q(U^k)^{n-1}] + \frac{1}{2}[3D^q_{exp}(U^k)^n - D^q_{exp}(U^k)^{n-1}] \\ &\quad + \frac{1}{2}[D^q_{imp}(\hat{U}^q) + D^q_{imp}(U^k)^n] \end{aligned} \tag{2.16}$$

$$\begin{aligned} &\frac{R^\xi_e(\phi)^{n+1}}{V^\xi_e} - \frac{R^\xi_w(\phi)^{n+1}}{V^\xi_w} + \frac{R^\eta_n(\phi)^{n+1}}{V^\eta_n} - \frac{R^\eta_s(\phi)^{n+1}}{V^\eta_s} + \frac{R^\zeta_f(\phi)^{n+1}}{V^\zeta_f} - \frac{R^\zeta_b(\phi)^{n+1}}{V^\zeta_b} \\ &\qquad = -\frac{\hat{U}^\xi_e - \hat{U}^\xi_w + \hat{U}^\eta_n - \hat{U}^\eta_s + \hat{U}^\zeta_f - \hat{U}^\zeta_b}{\Delta t} = -Q \end{aligned} \tag{2.17}$$

$$(U^q)^{n+1} = \hat{U}^q + \frac{\Delta t}{V^q} R^q(\phi)^{n+1} \tag{2.18}$$

Equations (2.16) are the momentum equations without the pressure term. They are solved for intermediate volume flux variables $\hat{U}^q$ $(q = \xi, \eta, \zeta)$, which do not satisfy the mass conservation

law. The pressure term p^{n+1} is approximated with ϕ^{n+1} from Equation (2.17), and the error associated with this approximation is $O(\Delta t)$. In Equations (2.18), ϕ^{n+1} is used to project the intermediate variables $\hat{U}^q$ $(q = \xi, \eta, \zeta)$ onto a divergence free space to find the volume flux U^q $(q = \xi, \eta, \zeta)$ at time step $n + 1$.

2.1.4 Poisson Equation

The DNS code is developed for flows in geometries that are curvilinear in the $\xi - \eta$ plane only. The third spatial dimension ζ is normal to the $\xi - \eta$ plane. With periodic boundary conditions and uniformly distributed grids in the spanwise direction, Equation (2.17) is rewritten as

$$C_{\xi,\eta}(\phi) + V^{\zeta}\frac{\partial^2 \phi}{\partial \zeta^2} = Q \tag{2.19}$$

which is a Poisson equation that can be solved using fast Fourier transform. The Fourier transform of Equation (2.19) is

$$C_{\xi,\eta}(\hat{\phi}(\xi, \eta, m)) - V^{\zeta}k_m^2\hat{\phi}(\xi, \eta, m) = \hat{Q}(\xi, \eta, m) \tag{2.20}$$

where $k_m = \sqrt{2[1 - cos(\pi m/N_\zeta)]}/\Delta\zeta$ $(m = 0, 1, N_\zeta - 2)$ is the modified wave number for 2nd order central differencing [Ferziger and Peric (2001)]. N_ζ is the number of nodes in the ζ direction and $\Delta\zeta$ is the grid spacing.

2.1.5 Boundary Conditions

To simulate the turbulent flow in an infinite serpentine channel, the computational domain can be an S-shaped channel or a U-shaped channel. The boundary conditions used in the simulation with an S-shaped channel are given in detail by Laskowski (2005). Periodic boundary conditions are applied to the velocity and the pressure in the spanwise direction, the no-slip boundary condition is specified at both walls, and the convection boundary condition is used at the outlet. The periodicity inside the infinite serpentine channel is imposed by recycling the velocity from a symmetry plane, near the exit, to the inlet. In the streamwise direction, the volume fluxes at time step n are used as boundary values for the intermediate variables, which results in the Neumann boundary condition for the pressure. The pressure is a solution

to the Poisson equation without any symmetry. This creates the mean pressure drop required to produce the prescribed bulk flow rate.

A U-shaped channel, which is half of the S-shaped channel, is adopted in the present simulation to reduce the computational cost. The boundary conditions with the U-shaped and the S-shaped channels are the same, except at the inlet. Figure 2.2 shows a spanwise cross-section of the S-shaped channel. Points $A1$, $B1$ and $C1$ are on one curve while points An,Bn and Cn are on the other side. The velocity at points from $C1$ to Cn is copied to points from $A1$ to An for periodicity. The S-shaped channel consists of two U-shaped channels and the exit region of the first U-shaped channel overlaps with the inlet area of the second U-shaped channel. Point $B1$ at the inlet of the second U-shaped channel corresponds to point An in the first U-shaped channel. The velocity at points from $B1$ to Bn is reflected in the streamwise direction to provide the boundary values for points from An to $A1$. For example, the velocity of point An is computed from the velocity of point $B1$ as:

$$u_{An} = -u_{B1}, \quad v_{An} = v_{B1}, \quad w_{An} = w_{B1} \tag{2.21}$$

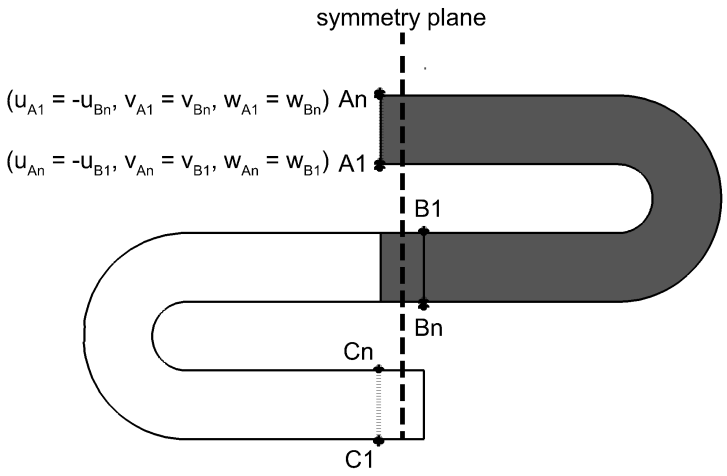

Figure 2.2 Periodic boundary condition in the streamwise direction for the fluid phase.

2.1.6 Grid Resolution

Figure 2.3 presents the geometry of the U-shaped channel and Figure 2.4 shows a spanwise cross-section of the U-shaped channel. The length in the spanwise is $3\pi\delta$. Grid resolution tests were conducted using the S-shaped channel in Laskowski (2005), and the mesh size adopted for $Re_b = 2800$ was $768 \times 128 \times 256$ in the streamwise, wall-normal and spanwise directions. The same grid resolution is adopted in the U-shaped channel, but the number of mesh points in the streamwise is reduced to 384. Grids are uniformly distributed in the spanwise direction and along the centerline in the streamwise direction. In the wall-normal direction, grids are stretched by a hyperbolic tangent stretching function and the distance from the inner wall is

$$d_j = 1.0 - \frac{\tanh(\gamma(1 - \frac{2(j-1)}{jmax-1}))}{\tanh(\gamma)} \quad j = 1, 2, ..., jmax \tag{2.22}$$

where the strecthing parameter γ is 1.6.

Figure 2.3 Geometry of the U-shaped channel.

2.1.7 Validation

Figure 2.5 displays the instantaneous spanwise vorticities in a spanwise cross-section. Figure 2.6 presents the mean velocity vectors that are averaged over time and in the spanwise

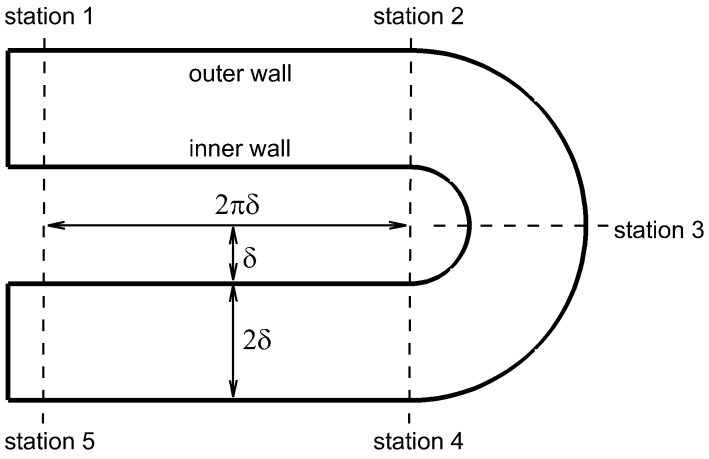

Figure 2.4 A spanwise cross-section of the U-shaped channel.

direction. The insert shows a slender separation bubble. Figure 2.7 presents the profiles of the streamwise velocity component at Stations 1, 2, 3, 4 and 5, as shown in Figure 2.4. d represents the distance from the inner wall, with 0 being the inner wall and 2 being the outer wall. The velocity u^+ is normalized with the averaged friction velocity u^*, which is defined as

$$u^* = \sqrt{\frac{1}{2}\frac{\int c_f ds}{\int ds}} u_b \tag{2.23}$$

where c_f is the skin friction coefficient and s is the distance along channel walls. Figure 2.8 delineates the skin friction coefficient along the inner and outer walls. The averaged friction velocity is $0.081u_b$, and the corresponding friction velocity Reynolds number $Re_\tau = \rho u^* \delta/\mu$ is about 226. The profile of the skin friction coefficient is in good agreement with Laskowski and Durbin (2007). The streamwise velocity component profiles also agree with those in Laskowski (2005) though the magnitude of the normalized velocity is different. The difference in the magnitude is caused by the reference velocity u^*. In Laskowski (2005), the magnitude of the reference velocity is $0.064u_b$, which is actually the friction velocity in a plane channel at $Re_b = 2800$.

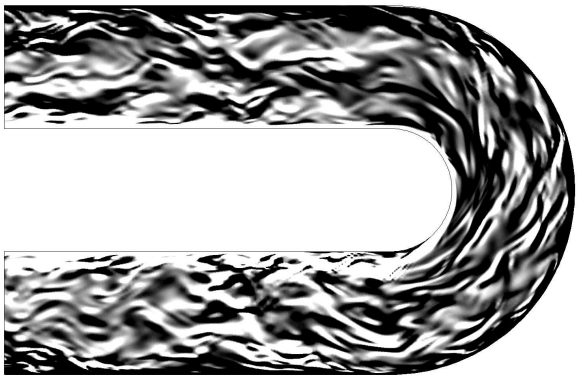

Figure 2.5 Instantaneous spanwise vorticities in a spanwise cross-section.

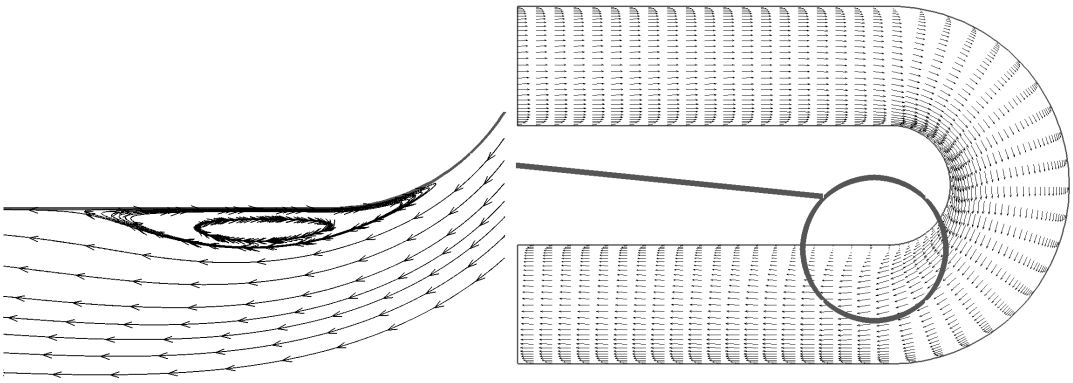

Figure 2.6 Mean velocity vectors in the U-shaped channel.

2.2 LPT Method for the Particle Phase

The particle phase is solved using the Lagrangian particle tracking (LPT) approach under the one-way coupling condition. The governing equations of particle motion are given, followed by the definition of Stokes number and the methods of time integration and velocity interpolation. The boundary conditions and the parallelization strategy for the particle phase are explained. A verification case of the LPT module is presented.

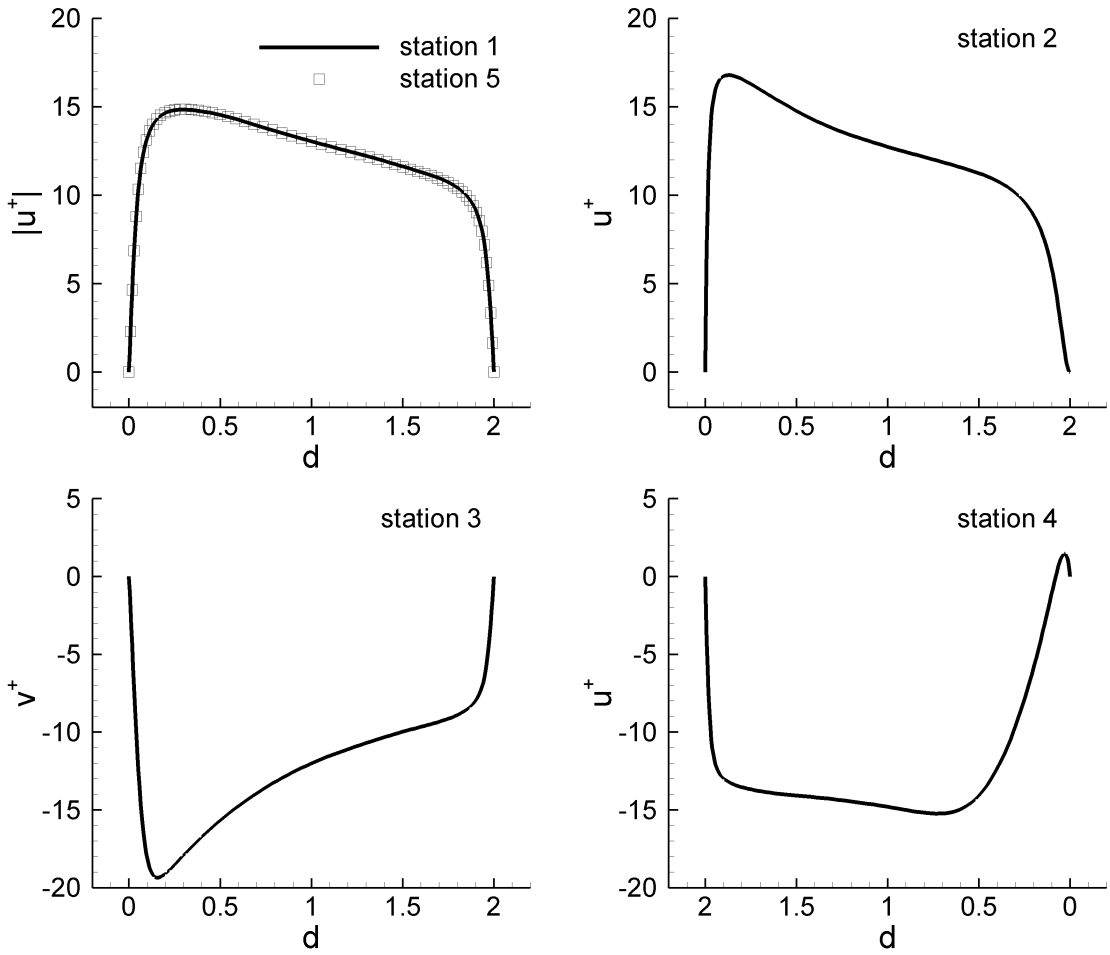

Figure 2.7 The streamwise velocity component of the fluid at Stations 1, 2, 3, 4 and 5 in the U-shaped channel. d represents distance from inner wall, with 0 being inner wall and 2 being outer wall

2.2.1 Equations of Motion

Simulating particle motion in a turbulent flow is extremely difficult if particle-particle collision is included or momentum exchange from particles to the fluid is considered. These two interactions may be neglected if the particle loading is small. The flow with spherical particles is considered to be dilute if the distance between the centers of particles is greater than three times of the particle diameter, which requires particle volume concentration to be less than 0.02 [Michaelides (2006)]. The equations of the fluid phase are then unchanged and particle motion can be described with a set of ordinary differential equations including only forces from the fluid and gravity. The effect of gravity is not of interest here and is omitted. However, forces

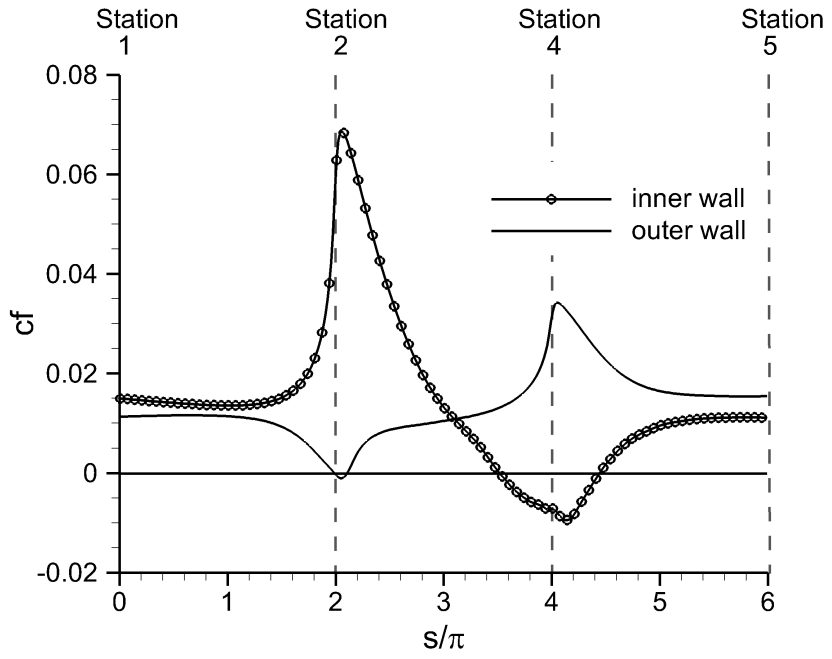

Figure 2.8 Skin friction coefficient in the U-shaped channel.

from the fluid phase on particles are still very complicated. To further simplify the problem, particle density ρ_p is chosen to be much larger than fluid density ρ_f. For heavy particles with $\rho_f/\rho_p \ll 1$, Basset force is negligible. Magnus lift can be ignored if particle diameter d_p is small. With all the above simplifications, the only significant force on particles from the fluid is Stokes drag, and the equations of motion for rigid and spherical particles are reduced to

$$\frac{d\mathbf{x}_p}{dt} = \mathbf{u}_p \tag{2.24}$$

$$\frac{d\mathbf{u}_p}{dt} = \frac{3}{4}\frac{C_d}{d_p}\frac{\rho_f}{\rho_p}|\mathbf{u}_f - \mathbf{u}_p|(\mathbf{u}_f - \mathbf{u}_p) \tag{2.25}$$

where $\mathbf{u}_p$ is particle velocity and $\mathbf{u}_f$ is the fluid velocity at particle position $\mathbf{x}_p$. The drag coefficient C_d is an empirical correction for finite particle Reynolds number $Re_p = d_p\,|\mathbf{u}_f - \mathbf{u}_p|\,/\nu$. For $Re_p < 800$,

$$C_d = \frac{24}{Re_p}(1 + 0.15Re_p^{0.687}) \tag{2.26}$$

is commonly used [Crowe *et al.* (1998), Apte *et al.* (2003), Breuer *et al.* (2006)].

2.2.2 Stokes Number

Stokes number St is a non-dimensional parameter that characterizes particle response to the fluid. It is defined as the ratio of particle relaxation time $\tau_p = \rho_p d_p^2/(18\mu)$ to flow residence time τ_f. If $St \ll 1$, particle relaxation time is much shorter than flow residence time and particles will follow the flow. For particles with $St \gg 1$, the influence of the fluid on particles is small, thus particles will keep their initial trajectories.

In a straight turbulent channel flow, the flow residence time is the turbulent time scale $\tau^+ = \nu/u^{*2}$ since turbulence is responsible for the non-uniform distribution of particles. The corresponding Stokes number is defined as

$$St^+ = \frac{\rho_p d_p^2 u^{*2}}{18\rho_f \nu^2} \tag{2.27}$$

In a serpentine channel, the curved bend is the dominant cause of the non-uniform distribution of particles, thus the flow residence time should be the time for flow to pass the curved section. It is estimated with the bulk flow time scale $\tau_b = \delta/u_b$, and the corresponding Stokes number is

$$St_b = \frac{\rho_p d_p^2 u_b}{18\rho_f \nu \delta} \tag{2.28}$$

The ratio of St^+ to St_b is

$$\frac{St^+}{St_b} = \frac{\tau_p/\tau^+}{\tau_p/\tau_b} = \frac{u^{*2}\delta}{u_b \nu} = \frac{Re_\tau^2}{Re_b} \tag{2.29}$$

2.2.3 Time Integration and Velocity Interpolation

Particle tracking is performed after each fluid phase update, and the tracking time step Δt_p is chosen equal to or smaller than fluid phase time step Δt_f. If a particle travels more than one cell during one time step, its movement is recalculated with a reduced time step, such as one half of the previous time step. The equations of particle motion (2.24 and 2.25) are solved using a fourth-order multi-variable Runge-Kutta scheme. The particle position and velocity at t_{n+1} are updated using

$$\mathbf{x}_{p,n+1} = \mathbf{x}_{p,n} + \frac{1}{6}\Delta t_p(\mathbf{K}_{x1} + 2\mathbf{K}_{x2} + 2\mathbf{K}_{x3} + \mathbf{K}_{x4}) \tag{2.30}$$

$$\mathbf{u}_{p,n+1} = \mathbf{u}_{p,n} + \frac{1}{6}\Delta t_p(\mathbf{K}_{u1} + 2\mathbf{K}_{u2} + 2\mathbf{K}_{u3} + \mathbf{K}_{u4}) \tag{2.31}$$

with

$$\mathbf{K}_{x1} = \mathbf{u}_{p,n} \tag{2.32}$$

$$\mathbf{K}_{u1} = \frac{3}{4}\frac{C_d}{d_p}\frac{\rho_f}{\rho_p}\left|\mathbf{u}_{f,n}(\mathbf{x}_{p,n}) - \mathbf{u}_{p,n}\right|\left[\mathbf{u}_{f,n}(\mathbf{x}_{p,n}) - \mathbf{u}_{p,n}\right] \tag{2.33}$$

$$\mathbf{K}_{x2} = \mathbf{u}_{p,n} + \frac{1}{2}\mathbf{K}_{u1}\Delta t_p \tag{2.34}$$

$$\begin{aligned}\mathbf{K}_{u2} = {} & \frac{3}{4}\frac{C_d}{d_p}\frac{\rho_f}{\rho_p}\left|\mathbf{u}_{f,n}(\mathbf{x}_{p,n} + \frac{1}{2}\mathbf{K}_{x1}\Delta t_p) - (\mathbf{u}_{p,n} + \frac{1}{2}\mathbf{K}_{u1}\Delta t_p)\right| \\ & \left[\mathbf{u}_{f,n}(\mathbf{x}_{p,n} + \frac{1}{2}\mathbf{K}_{x1}\Delta t_p) - (\mathbf{u}_{p,n} + \frac{1}{2}\mathbf{K}_{u1}\Delta t_p)\right]\end{aligned} \tag{2.35}$$

$$\mathbf{K}_{x3} = \mathbf{u}_{p,n} + \frac{1}{2}\mathbf{K}_{u2}\Delta t_p \tag{2.36}$$

$$\begin{aligned}\mathbf{K}_{u3} = {} & \frac{3}{4}\frac{C_d}{d_p}\frac{\rho_f}{\rho_p}\left|\mathbf{u}_{f,n}(\mathbf{x}_{p,n} + \frac{1}{2}\mathbf{K}_{x2}\Delta t_p) - (\mathbf{u}_{p,n} + \frac{1}{2}\mathbf{K}_{u2}\Delta t_p)\right| \\ & \left[\mathbf{u}_{f,n}(\mathbf{x}_{p,n} + \frac{1}{2}\mathbf{K}_{x2}\Delta t_p) - (\mathbf{u}_{p,n} + \frac{1}{2}\mathbf{K}_{u2}\Delta t_p)\right]\end{aligned} \tag{2.37}$$

$$\mathbf{K}_{x4} = \mathbf{u}_{p,n} + \mathbf{K}_{u3}\Delta t_p \tag{2.38}$$

$$\begin{aligned}\mathbf{K}_{u4} = {} & \frac{3}{4}\frac{C_d}{d_p}\frac{\rho_f}{\rho_p}\left|\mathbf{u}_{f,n}(\mathbf{x}_{p,n} + \mathbf{K}_{x3}\Delta t_p) - (\mathbf{u}_{p,n} + \mathbf{K}_{u3}\Delta t_p)\right| \\ & \left[\mathbf{u}_{f,n}(\mathbf{x}_{p,n} + \mathbf{K}_{x3}\Delta t_p) - (\mathbf{u}_{p,n} + \mathbf{K}_{u3}\Delta t_p)\right]\end{aligned} \tag{2.39}$$

The fluid velocity $\mathbf{u}_f$ in Equation 2.25 is evaluated at the center of the spherical particle with tri-linear interpolation:

$$\begin{aligned}\mathbf{u}_f(\mathbf{x}_p) = {} & \mathbf{u}_f^{i,j,k}(1-\xi_p)(1-\eta_p)(1-\zeta_p) + \mathbf{u}_f^{i,j,k+1}(1-\xi_p)(1-\eta_p)\zeta_p \\ & + \mathbf{u}_f^{i+1,j,k}\xi_p(1-\eta_p)(1-\zeta_p) + \mathbf{u}_f^{i+1,j,k+1}\xi_p(1-\eta_p)\zeta_p \\ & + \mathbf{u}_f^{i,j+1,k}(1-\xi_p)\eta_p(1-\zeta_p) + \mathbf{u}_f^{i,j+1,k+1}(1-\xi_p)\eta_p\zeta_p \\ & + \mathbf{u}_f^{i+1,j+1,k}\xi_p\eta_p(1-\zeta_p) + \mathbf{u}_f^{i+1,j+1,k+1}\xi_p\eta_p\zeta_p\end{aligned} \tag{2.40}$$

With the present level of grid resolution, tri-linear interpolation is satisfactory; indeed, the flow code uses linear interpolation in solving the momentum equations. Apte *et al.* (2003) and Breuer *et al.* (2006) used tri-linear interpolation with a coarser, LES resolution.

An issue with the staggered mesh in the DNS solver is that the fluid velocity components (u_f,v_f,w_f) are computed at different locations. Thus, in the computation of u_p,v_p and w_p, the set of coefficients (ξ_p, η_p, ζ_p) is obtained in the computational cell of u_f,v_f and w_f, respectively. To estimate ξ_p and η_p, the quadrilateral mesh in the $x-y$ plane is mapped to a square, as

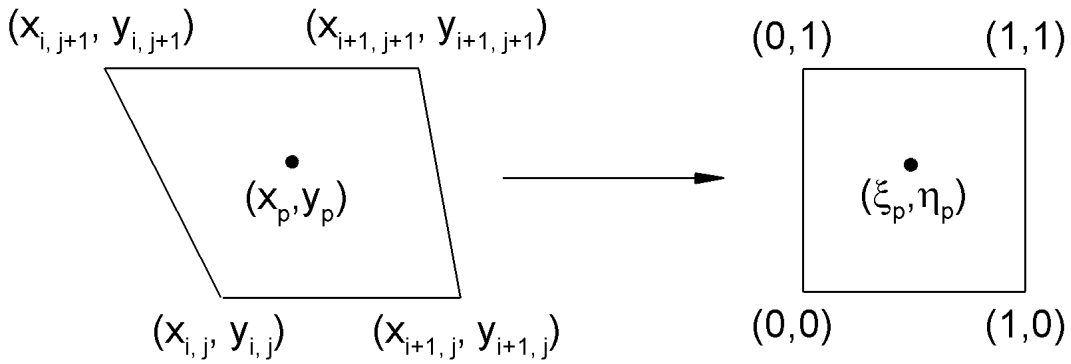

Figure 2.9 Quadrilateral to square mapping.

shown in Figure 2.9. The particle position in the computational space, ξ_p and η_p, is computed using

$$\xi_p = \begin{cases} -\frac{C_3}{C_2} & (C_1 = 0) \\ \frac{C_2 + \sqrt{C_2^2 - 4C_1C_3}}{2C_1} & (C_1 \neq 0) \end{cases} \tag{2.41}$$

and

$$\eta_p = \begin{cases} -\frac{D_3}{D_2} & (D_1 = 0) \\ \frac{D_2 - \sqrt{D_2^2 - 4D_1D_3}}{2D_1} & (D_1 \neq 0) \end{cases} \tag{2.42}$$

which are derived from a mapping function given in Tannehill *et al.* (1997). Here

$$\begin{aligned} C_1 &= (x_{i,j} - x_{i+1,j} + x_{i+1,j+1} - x_{i,j+1})(x_{i+1,j} - x_{i,j}) \\ &\quad -(y_{i,j} - y_{i+1,j} + y_{i+1,j+1} - y_{i,j+1})(y_{i+1,j} - y_{i,j}) \\ C_2 &= (y_{i,j} - y_{i+1,j} + y_{i+1,j+1} - y_{i,j+1})(y_p - y_{i,j}) \\ &\quad -(x_{i,j} - x_{i+1,j} + x_{i+1,j+1} - x_{i,j+1})(x_p - x_{i,j}) \\ &\quad +(x_{i+1,j} - x_{i,j})(y_{i,j+1} - y_{i,j}) - (y_{i+1,j} - y_{i,j})(x_{i,j+1} - x_{i,j}) \\ C_3 &= (x_{i,j+1} - x_{i,j})(y_p - y_{i,j}) - (y_{i,j+1} - y_{i,j})(x_p - x_{i,j}) \end{aligned}$$

and

$$\begin{aligned} D_1 &= (x_{i,j} - x_{i+1,j} + x_{i+1,j+1} - x_{i,j+1})(x_{i,j+1} - x_{i,j}) \\ &\quad -(y_{i,j} - y_{i+1,j} + y_{i+1,j+1} - y_{i,j+1})(y_{i,j+1} - y_{i,j}) \\ D_2 &= (y_{i,j} - y_{i+1,j} + y_{i+1,j+1} - y_{i,j+1})(y_p - y_{i,j}) \\ &\quad -(x_{i,j} - x_{i+1,j} + x_{i+1,j+1} - x_{i,j+1})(x_p - x_{i,j}) \\ &\quad -(x_{i+1,j} - x_{i,j})(y_{i,j+1} - y_{i,j}) + (y_{i+1,j} - y_{i,j})(x_{i,j+1} - x_{i,j}) \\ D_3 &= (x_{i+1,j} - x_{i,j})(y_p - y_{i,j}) - (y_{i+1,j} - y_{i,j})(x_p - x_{i,j}) \end{aligned}$$

If a particle moves across the boundary at an intermediate step of the Runge-Kutta integration, the fluid velocity at the particle location is extrapolated from the first cell adjacent to the boundary. The boundary conditions, such as wall reflection, are only invoked at the end of the Runge-Kutta integration.

2.2.4 Boundary Conditions

In the particle phase, boundary conditions are applied to particles that are out of the computational domain at the end of the Runge-Kutta integration. The boundary conditions in the particle phase should be consistent with those in the fluid phase. In the streamwise and spanwise directions, periodic boundary conditions are adopted for the particle phase. The treatment of the periodic boundary condition between the inlet and the outlet is similar to that in the fluid phase. An example is given in Figure 2.10. The particle at position A, closer to the outer wall at the exit, is recycled to position B, closer to the inner wall at the inlet, with its streamwise velocity component reversed.

If a particle striks the wall at the end of the Runge-Kutta integration, it is reflected using

$$\breve{\mathbf{u}}_p = -e_n \left(\tilde{\mathbf{u}}_p \cdot \hat{\mathbf{n}}\right) \hat{\mathbf{n}} + e_t \left(\tilde{\mathbf{u}}_p \cdot \hat{\mathbf{t}}\right) \hat{\mathbf{t}} \tag{2.43}$$

where $\hat{\mathbf{n}}$ is the surface normal and $\hat{\mathbf{t}}$ is the plane tangent. e_n and e_t are the coefficients of restitution in the wall normal and tangential directions. $\tilde{\mathbf{u}}_p$ and $\breve{\mathbf{u}}_p$ are particle velocity before and after the impact. The incident velocity $\tilde{\mathbf{u}}_p$ is neither the velocity of the particle at the beginning of the Runge-Kutta update nor the velocity at the end. It is estimated with the

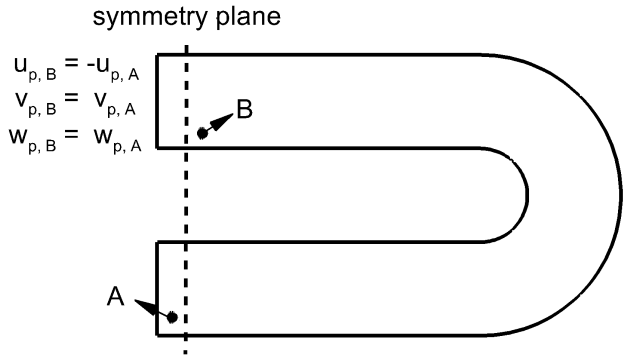

Figure 2.10 Periodic boundary condition in the streamwise direction for the particle phase.

mean velocity of the particle during that time step. At the end of the time step, the particle velocity is updated to $\breve{\mathbf{u}}_p$.

2.2.5 Estimation of Surface Erosion

The surface erosion is evaluated by accumulating the mass removed by particle-wall collisions from each computational cell on the channel walls. The ratio of the mass removed during one particle-wall impact to the mass of the impinging particle is defined as erosion ratio ER. It is estimated with an empirical formula given in Ahlert (1994):

$$ER = AF_s V_{imp}^{1.73} f(\alpha) \tag{2.44}$$

with

$$f(\alpha) = \begin{cases} 0.227\alpha - 0.384\alpha^2 & (\alpha < \pi/12) \\ 0.0315\cos^2\alpha\sin\alpha + 0.0036\sin^2\alpha + 0.0253 & (\alpha \geq \pi/12) \end{cases} \tag{2.45}$$

Here, V_{imp} is the impact velocity and α is the incident angle relative to the surface tangent. A and F_s are constants related to particle material and shape. This formula primarily represents the non-liner dependence of erosion ratio upon angle of incidents and impact velocity. High velocities make a disproportionate contribution and the erosion may not be the greatest where the maximum number of impacts occurs.

2.2.6 Parallelization Strategy

The computational domain is partitioned in both the streamwise and wall-normal directions. Every processor solves its local flow field and obtains information on three overlapping lines of grids from each neighboring processor. The particle phase update needs the fluid velocity at particle locations, thus each processor only stores and tracks particles in its sub-domain. If a particle moves across the inter-processor boundary, it enters the overlapping area first. At the end of each particle phase update, all processors check for particles in the overlapping area, and search for new hosting processors to accept those particles. Particles are rearranged into groups with respect to their new hosts. To transfer particles between neighboring processors, two MPI communications are requested. In the first MPI communication, each processor is informed about the number of particles that it will receive from other processors. This is a preliminary for the second MPI communication, in which particles are sent from their previous hosts and received by their new hosts.

2.2.7 Verification

To verify the implementation of the parallel Lagrangian particle tracking module, the first attempt is to seek possible analytical solutions to particle motion equations 2.24 and 2.25. With a simplified drag coefficient $C_d = 24/Re_p$, Equation 2.25 is rewritten in terms of Stokes number St_b as

$$\frac{d\mathbf{u}_p}{dt} = \frac{1}{St_b}(\mathbf{u}_f - \mathbf{u}_p) \tag{2.46}$$

An analytical solution to Equations (2.24) and (2.46) can be obtained in the following steady velocity field:

$$u_f(x, y, z) = 0.2 \tag{2.47}$$

$$v_f(x, y, z) = -0.05y \tag{2.48}$$

$$w_f(x, y, z) = 0 \tag{2.49}$$

with a wall placed at $y = 0$. Particles are released at $(x_p, y_p, z_p)(t = 0) = (1, 1, \pi)$ with the initial velocity $(u_p, v_p, w_p)(t = 0) = (0.2, -0.5, 0)$. The trajectory of a particle with $St_b < 5.0$

is given exactly by:

$$x_p(t) = 1 + 0.2t \tag{2.50}$$

$$y_p(t) = \left| \frac{0.5 + \lambda_2}{\lambda_2 - \lambda_1} \exp(\lambda_1 t) + \frac{-0.5 - \lambda_1}{\lambda_2 - \lambda_1} \exp(\lambda_2 t) \right| \tag{2.51}$$

$$z_p(t) = \pi \tag{2.52}$$

where

$$\lambda_{1,2} = \frac{-1 \pm \sqrt{1 - 0.2St_b}}{2St_b} \tag{2.53}$$

and the absolute value in Equation (2.51) implements the elastic reflection boundary condition at $y = 0$.

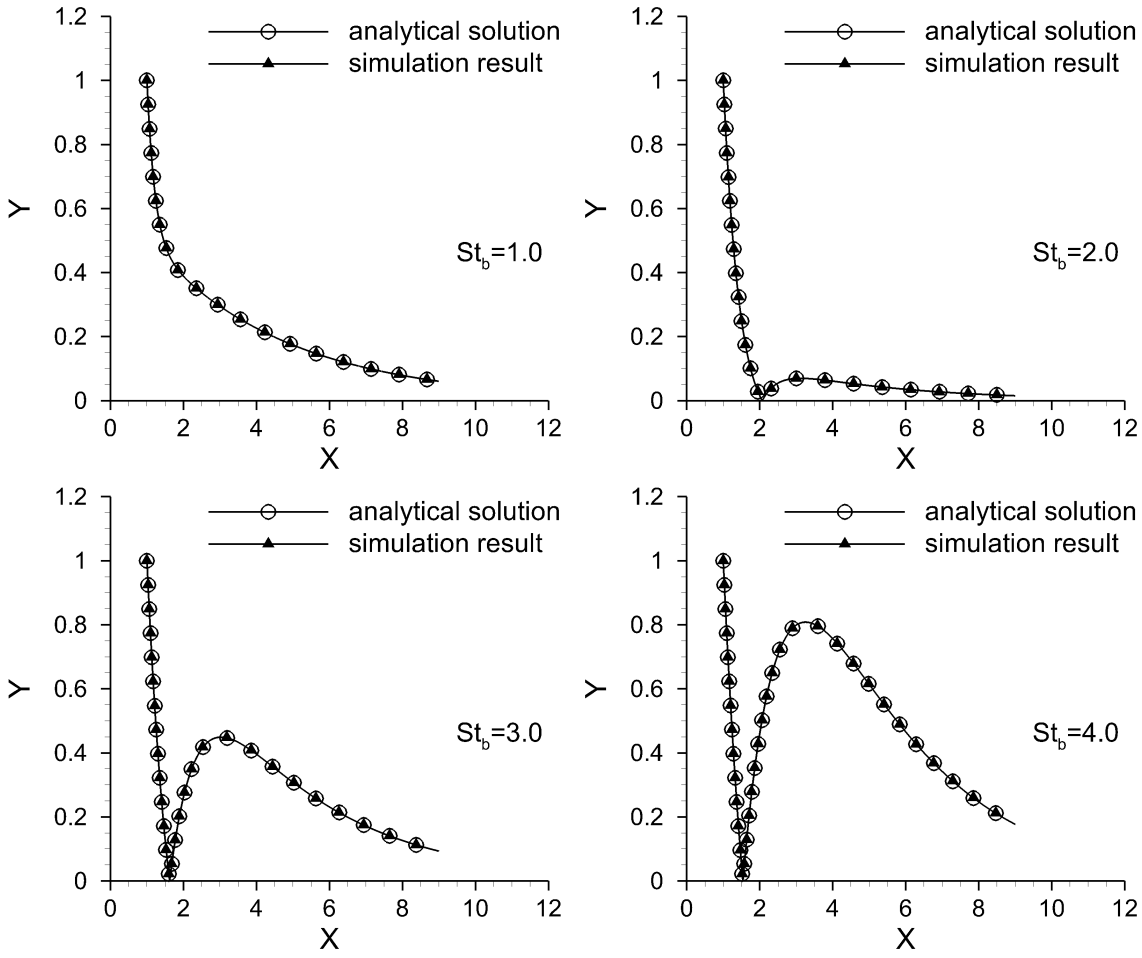

Figure 2.11 Analytical solutions and numerical simulations of particle trajectories in a steady velocity field with a simplified drag coefficient.

Figure 2.11 presents the analytical solutions of $St_b = 1.0$, 2.0, 3.0 and 4.0 and the corresponding trajectories from numerical simulations. The numerical results and the analytical solutions are nearly identical. In the numerical simulation, the dimensions of the computational domain are $4\pi \times 2 \times 2\pi$ with mesh size $128 \times 128 \times 128$ in x, y and z directions. The computational domain is partitioned using 4 processors in the x direction and 4 in the y direction. The tracking time step is $\Delta t_p = 2 \times 10^{-3}$ and the number of time step tracked is 2×10^4. Particles are initialized with a tendency to hit the wall, but they are decelerated by the fluid as they move toward the wall. By the end of the simulation ($t = 40$), the particle of $St_b = 1.0$ has not reached the wall. For $St_b \geq 2.0$, particles collide with the wall once, and the location of the collision shifts in the downstream direction as the Stokes number increases. In this simulation, not only the methods of time integration and velocity interpolation but also the implementation of wall boundary conditions and MPI parallelization are verified.

2.3 Parallel Performance

Both the DNS code and the LPT module are parallelized with MPI. In parallel computing, the speedup is defined as the ratio of clock time with one processor to multiple processors, and the parallel efficiency is defined as the ratio of the speedup to the number of processors. Figure 2.12 presents the speedup of the DNS solver with mesh size $384 \times 128 \times 256$. Because the computational domain is partitioned in both the streamwise and cross-stream directions, there may be multiple choice of partition for the same number of total processors. The three curves represent three partition options: the number of processors in the streamwise direction (npx) is constant at 16; the number of processors in the wall-normal direction (npy) is constant at 8; the ratio of npx to npy is 2. Generally, the parallel efficiency is 1/2. It is reduced by the computation and communication time of the overlapping cells. For example, with 16 processors in the streamwise direction and 8 in the wall-normal direction, the number of overlapping cells is nearly 10% of the total number of computational cells. The number of overlapping cells varies with the numbers of processors in the streamwise and wall-normal directions, which explains the slight difference in the speedup among different partition options.

Figure 2.13 presents the speedup of particle phase solver, which is evaluated by tracking

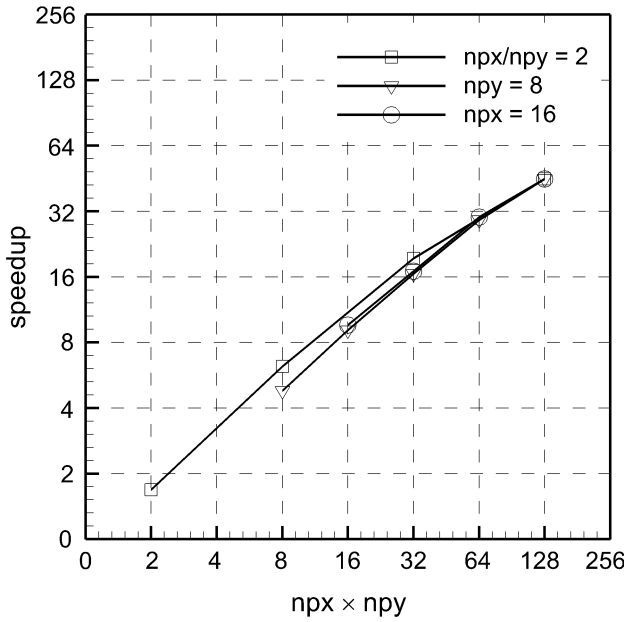

Figure 2.12 Speedup of the DNS solver. *npx* and *npy* are the numbers of processors in the streamwise and wall-normal directions, respectively.

1.2×10^6 particles of various Stokes numbers in a frozen flow field inside the U-shaped channel. Due to the non-uniform distribution of particles, some processors have much heavier loading of particles than the others, which has a negative effect on the parallel efficiency. The efficiency drops below 1/2 when the number of processors increases to 32.

2.4 Summary

This chapter introduced the direct numerical simulation (DNS) code for the fluid phase and the Lagrangian particle tracking (LPT) module for the particle phase. A U-shaped channel was adopted with a special treatment of the boundary conditions. Simulation results, such as skin friction coefficient, agreed with those in Laskowski and Durbin (2007) and Laskowski (2005). The LPT module with a simplified drag coefficient was verified in a steady velocity field. The simulation results were in good agreement with the analytical solutions. This verification case does not include the effect of turbulence on particles, which may require high resolutions. Further validation will be described in the next chapter.

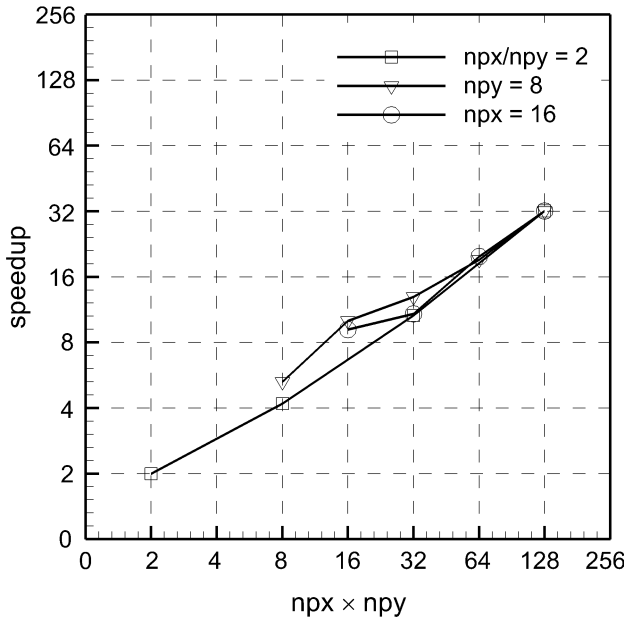

Figure 2.13 Speedup of the LPT module. *npx* and *npy* are the numbers of processors in the streamwise and wall-normal directions, respectively.

CHAPTER 3. PARTICLE MOTION IN A PLANE TURBULENT CHANNEL

The Lagrangian particle tracking (LPT) module has been verified in a steady velocity field. This chapter provides the validation of the LPT module for particles of various Stokes numbers in a plane turbulent channel flow. The initialization in the particle phase simulation is explained, followed by the study of the tracking time step resolution. Simulation results, such as mean concentration, are presented and compared to those in Marchioli *et al.* (2008b), which is an international collaboration. Turbophoresis, a mean drift on particles toward the wall, is adopted as an explanation for the accumulation of particles in the near wall region.

3.1 Fluid Phase in a Plane Turbulent Channel

The dimensions of the plane channel are $4\pi\delta \times 2\delta \times 2\pi\delta$, as shown in Figure 3.1, with mesh size $128 \times 128 \times 128$ in the streamwise, wall-normal and spanwise directions. The mesh is uniformly distributed in the streamwise and spanwise directions, and is stretched in the wall-normal direction with the same spacing as the mesh in the U-shaped channel. At the first wall-adjacent cell, $y^+ = 0.752$. The friction velocity Reynolds number is $Re_\tau = u_*\delta/\nu = 180$. This corresponds to the bulk velocity Reynolds number $Re_b = U_b\delta/\nu = 2800$, which is used in the U-shaped channel.

Figure 3.2 shows the fluid mean streamwise velocity in wall units. The simulation result matches the linear curve in the viscous sublayer

$$u^+ = y^+ \tag{3.1}$$

and satisfies the logarithmic law of wall in the log layer

$$u^+ = \frac{1}{\kappa}\log(y^+) + B \tag{3.2}$$

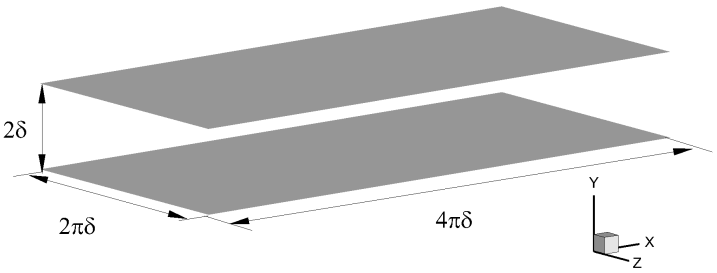

Figure 3.1 Geometry of the plane channel.

with $\kappa = 0.41$ and $B = 5.5$ [Durbin *et al.* (2001)]. Figure 3.3 shows the fluid root mean square (RMS) velocity fluctuations in the streamwise, wall-normal and spanwise directions. The results agree with those from other simulations at $Re_\tau = 180$.

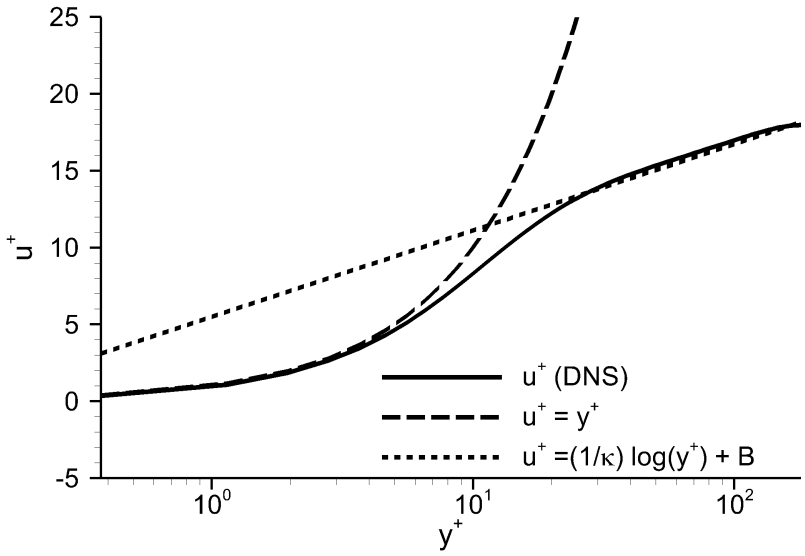

Figure 3.2 Fluid mean streamwise velocity in the plane turbulent channel ($Re_\tau = 180$).

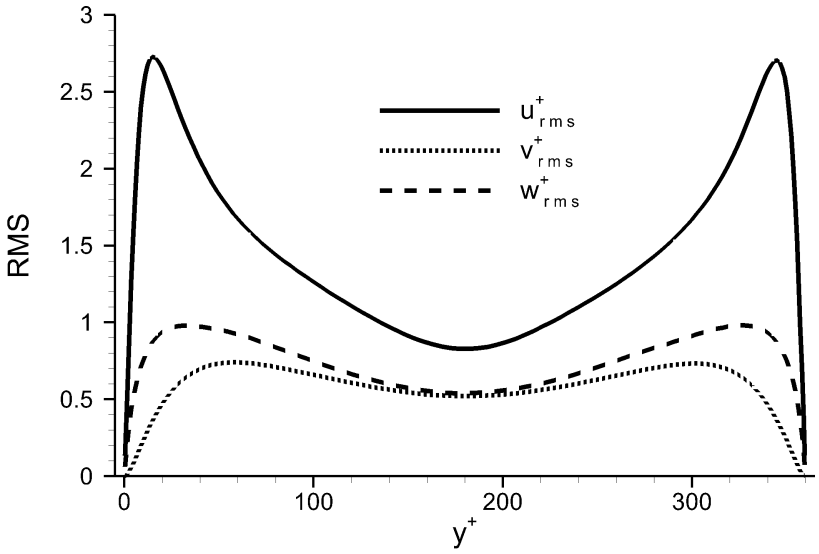

Figure 3.3 Fluid root mean square velocity fluctuations in the plane turbulent channel ($Re_\tau = 180$).

3.2 Particle Phase in a Plane Turbulent Channel

3.2.1 Particle Properties

The Stokes numbers St_b, base on $Re_b = 2800$, range from 0.125 to 6.0, and the corresponding Stokes numbers St^+, based on $Re_\tau = 180$, range from 1.45 to 69.43. The density and diameter of each Stokes number are listed in Table 3.1. Particle diameter is chosen to be smaller than the size of the first mesh adjacent to the wall, which is $y^+ = 0.752$. The number of particles for each Stokes number is 10^5, as used by ASU and TUE groups in Marchioli *et al.* (2008b). When particles are uniformly distributed throughout the channel, the volume concentration is about 3.3×10^{-7} for particles with diameter $d_p^+ = 0.18$ and 2.7×10^{-6} for those with $d_p^+ = 0.36$. For particle phase statistics, the plane channel is uniformly divided into 800 wall-parallel slabs, and the thickness of each slab is $\Delta y_s^+ = 0.45$. These statistical slabs can be coarsened depending on the required resolution during post-processing.

Table 3.1 Particle Properties

Set	St_b	St^+	d_p/δ	d_p^+	ρ_p/ρ_f
1	0.125	1.45	0.001	0.18	804
2	0.5	5.79	0.002	0.36	804
3	1.0	11.57	0.002	0.36	1607
4	2.0	23.14	0.002	0.36	3214
5	3.0	34.71	0.002	0.36	4821
6	4.0	46.29	0.002	0.36	6429
7	5.0	57.86	0.002	0.36	8036
8	6.0	69.43	0.002	0.36	9643

3.2.2 Initialization

At the beginning of the simulation, particles are uniformly distributed throughout the channel with their velocity equal to the local fluid velocity. In a laminar flow, particle concentration would remain uniform. In the plane turbulent channel, the initially uniform distribution of particles evolves into a non-uniform distribution with time. The non-uniform distribution becomes fully developed after more than one hundred flow through times of the channel. At that time, the effect of particle initial velocity is negligible [Apte *et al.* (2003), Marchioli *et al.* (2008b)].

3.2.3 Tracking Time Step

The time step used in the DNS solver is $\Delta t_f = 2 \times 10^{-3}$ (or $\Delta t_f^+ = 0.023$). Particle movements are calculated using the flow field from each DNS update, therefore the tracking time step Δt_p is either equal to or smaller than the fluid phase time step Δt_f. In the study of tracking time step resolution, particles with the lowest Stokes number ($St^+ = 1.45$) are tracked using the following four time steps: Δt_f, $\frac{1}{2}\Delta t_f$, $\frac{1}{4}\Delta t_f$ and $\frac{1}{8}\Delta t_f$.

At the beginning, 10^5 particles are uniformly distributed throughout the channel. The volume concentration of particles in each statistical slab is denoted as the initial concentration C_0. The uniform distribution then evolves into a non-uniform distribution, and the concentration is the highest inside the first statistical slab adjacent to the wall. Figure 3.4 presents the ratio of the maximum concentration C_{max} to the initial concentration C_0 at successive time intervals. Despite the difference in the exact magnitude, there is general consistency in the evolution of

C_{max}/C_0 among all tracking time steps. The difference in the magnitude indicates that the movements of individual particles may be sensitive to the tracking time steps. However, the motion of individual particles in a short time interval is not of interest.

Figure 3.5 shows the profiles of particle mean concentration C/C_0 averaged over 40 flow through times after $t^+ = 15,000$. The mean concentration C/C_0 has a peak at $y^+ < 1$, and the difference in the maximum C/C_0 caused by the tracking time step is less than 2%. Besides the mean concentration, other important statistics are particle root mean square (RMS) velocity fluctuations. Figure 3.6 presents the profiles of particle RMS in the streamwise, wall-normal and spanwise directions. Again, the tracking time step has nearly no influence on particle RMS statistics for $St^+ = 1.45$. As St^+ increases, particle response time to the fluid velocity fluctuations becomes longer, and the update of particle movements are less sensitive to the tracking time step. Therefore, for $1.45 \leq St^+ \leq 69.43$, particle phase statistics are independent of the tracking time step if it is equal to or smaller than the fluid solver time step. For the simulation presented in the rest of this chapter, the particle tracking time step is half of the time step in the fluid solver.

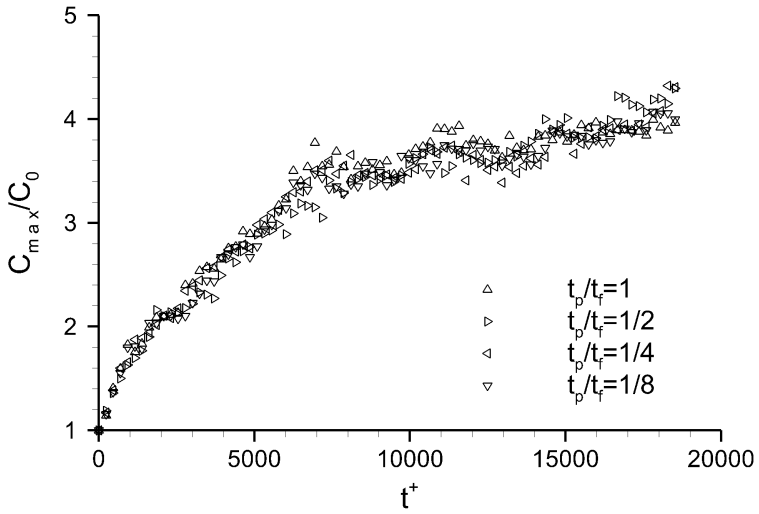

Figure 3.4 Particle maximum concentration in the plane turbulent channel at successive time intervals, obtained with different tracking time steps. ($St^+ = 1.45$)

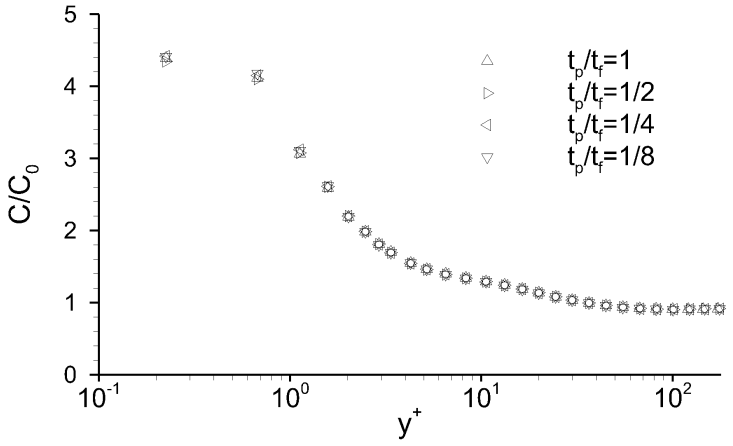

Figure 3.5 Particle mean concentration across the half channel height in the plane turbulent channel, obtained with different tracking time steps. ($St^+ = 1.45$)

3.2.4 Instantaneous Distribution and Mean Concentration

In the present simulation, particles of various Stokes numbers are computed simultaneously within a single flow simulation. For each Stokes number, 10^5 particles are uniformly initialized throughout the channel. Figure 3.7 shows the snapshots of particle distribution at $t^+ \approx 26,000$, which is about 180 flow through times. The z coordinate is projected onto a spanwise cross-section by placing a dot at the x-y coordinate. According to Figure 3.4, the non-uniform distribution of particles has become fully developed at $t^+ \approx 20,000$. At $St^+ = 1.45$ (plot a), particle distribution seems to be uniform across the channel height. As St^+ increases from 5.79 to 23.14 (plots b-d), particle loading away from the wall becomes more and more diluted. As St^+ increases from 34.71 to 69.43 (plots e-h), the change in particle distribution is barely discernible. Figure 3.8 shows the profiles of the mean concentration averaged over 115 flow through times after $t^+ \approx 26,000$. The horizontal scale is logarithmic to expand the wall region. For each Stokes number, the concentration has a peak, rising steeply in the region of $y^+ < 1$. The concentration profiles of $St^+ \leq 23.14$ are in general agreement with those shown in Figure 6 of Marchioli *et al.* (2008b). In their simulations, the flow friction velocity Reynolds number Re_τ is 150, and particle Stokes numbers St^+ are 1, 5 and 25. As St^+ increases from 1 to 25, the maximum concentration C_{max}/C_0 rises from about 4 to about 250.

Although the concentration in the region of $y^+ < 1$ rises rapidly at $1.45 \leq St^+ \leq 23.14$, it

only increases slightly as St^+ increases from 23.14 to 69.43. These are in qualitative agreement with the experimental data of particle deposition velocity in the fully developed turbulent pipe flow, which is summarized in McCoy and Hanratty (1977) and Young and Leeming (1997). Ignoring the influence of particle reflection from the walls, particle concentration adjacent to the wall rises with the deposition velocity of particles. In Young and Leeming (1997), the particle deposition curve is nominally divided into three regimes: diffusional deposition, diffusion-impaction and inertia-moderated. Particles with $0.3 < St^+ < 20$ are in the diffusion-impaction regime, and the deposition velocity increases several orders of magnitude as St^+ increases from 0.3 to 20. Particles with $St^+ > 20$ are in the inertia-moderated regime, and the deposition velocity is nearly constant as St^+ increases from 20 to 70.

3.2.5 Velocity Statistics

Beside of the mean concentration, the statistics of particle velocity at $1.45 \leq St^+ \leq 23.14$ are also in agreement with those in Marchioli *et al.* (2008b). Figure 3.9 shows the profiles of particle mean streamwise velocity and fluid mean streamwise velocity, which is the average of the fluid streamwise velocity at the locations of particles. At $St^+ = 1.45$, the particle mean streamwise velocity u^+ matches with the fluid u^+. At $St^+ = 34.7$ and $St^+ = 69.43$, the particle u^+ is lower than the fluid u^+ in the core region, and the difference becomes larger with the Stokes number. Figures 3.10-3.12 present the profiles of particle phase root mean square (RMS) velocity fluctuations in the streamwise, wall-normal and spanwise directions. In the streamwise direction (Figure 3.10), the particle RMS is higher than the fluid RMS at $y^+ \leq 100$. The peak value of $St^+ = 1.45$ is close to the maximum in the fluid phase. For $5.79 \leq St^+ \leq 69.43$, the peak value varies slightly with the Stokes number, and it is about 10% larger than the fluid phase maximum. In the wall-normal and spanwise directions (Figures 3.11 and 3.12), the profiles of $St^+ = 1.45$ are nearly identical to those of the fluid. The magnitude of the particle RMS diminishes with the Stokes number. As St^+ increases from 1.45 to 69.43, the maximum RMS drops approximately 50%.

3.2.6 Turbophoresis

In the plane turbulent channel, the accumulation of particles in the near wall region may be caused by turbulent diffusion plus turbophoresis. Young and Leeming (1997) invoked a two-fluid model by representing the particle phase as a continuum. In the fluid phase, a pressure gradient, transverse to the flow direction, exists to balance the gradient of turbulent normal stress. Specifically

$$\partial_y P = -\rho \partial_y \overline{v^2} \tag{3.3}$$

The dilute particle phase experiences no pressure force but a drag from the fluid phase. Thus the turbulent normal stress gradient must be balanced by a mean movement in the cross-streamwise direction. The mean momentum equation of the particle phase in the plane turbulent channel has the form

$$D_t V_p + \frac{V_p}{\tau_p} = -\partial_y \overline{v_p^2} + \dots \tag{3.4}$$

where V_p is the particle mean velocity in the wall-normal direction. A non-dimensional form of the normal stress gradient on the right side is defined as turbophoretic force:

$$F^+_{turbo} = -\frac{d\overline{v_p^{+2}}}{dy^+} \tag{3.5}$$

Figure 3.14 shows the profiles of particle turbophoretic force across the half channel height. For all Stokes numbers, the turbophoretic force is negative at $y^+ < 60$, where particles are drifted toward the wall. Balancing the drag force on the left side of Equation 3.4 with the normal stress gradient on its right side shows that

$$V^+_P \approx St^+ F^+_{turbo} = V^+_{turbo} \tag{3.6}$$

Thus, particle mean velocity in the wall normal direction can be approximated by $St^+ F^+_{turbo}$, which is defined as turbophoretic velocity V^+_{turbo}. Figure 3.14 displays the profiles of particle turbophoretic velocity across the half channel height. For all Stokes numbers, the turbophoretic velocity has its peak value at $y^+ \approx 20$, and the magnitude of the peak value becomes larger as St^+ increases from 1.45 to 69.43. The magnitude of V^+_{turbo} rises more rapidly at $1.45 \leq St^+ \leq 23.14$ than at $23.14 \leq St^+ \leq 69.43$, which agrees with the change of the near-wall concentration in Figure 3.8.

3.3 Summary

Particle motion in a plane turbulent channel was simulated using the DNS solver with the LPT module. The initial uniform distribution of particles evolved into a non-uniform distribution. For the range of Stokes numbers simulated, particle phase statistics were independent of the tracking time step if it was equal to or smaller than the fluid solver time step. Simulation results were in general agreement with Marchioli *et al.* (2008b) and Young and Leeming (1997). Building on this validation, the next chapter applies the DNS solver and the LPT module to simulate particle motion in a turbulent U-shaped channel.

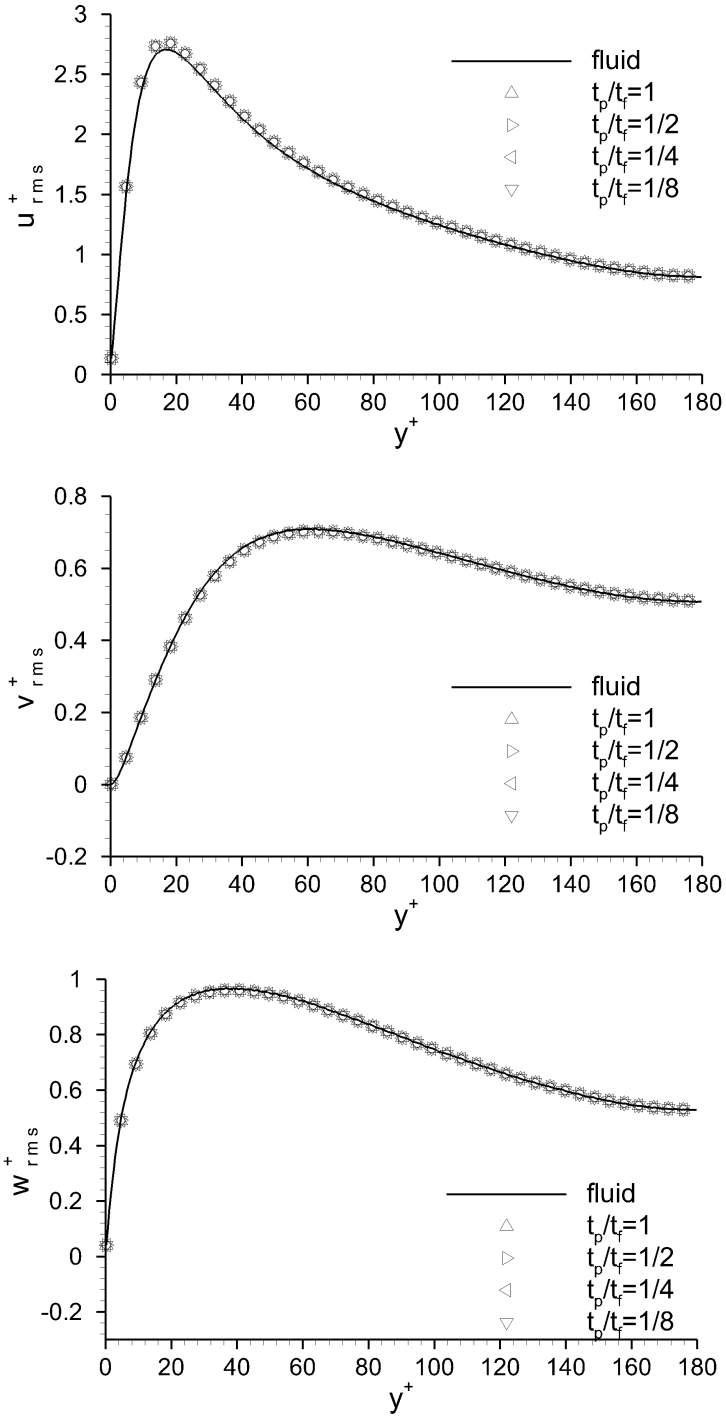

Figure 3.6 Particle root mean square velocity fluctuations across the half channel height in the plane turbulent channel, obtained with different tracking time steps. ($St^+ = 1.45$)

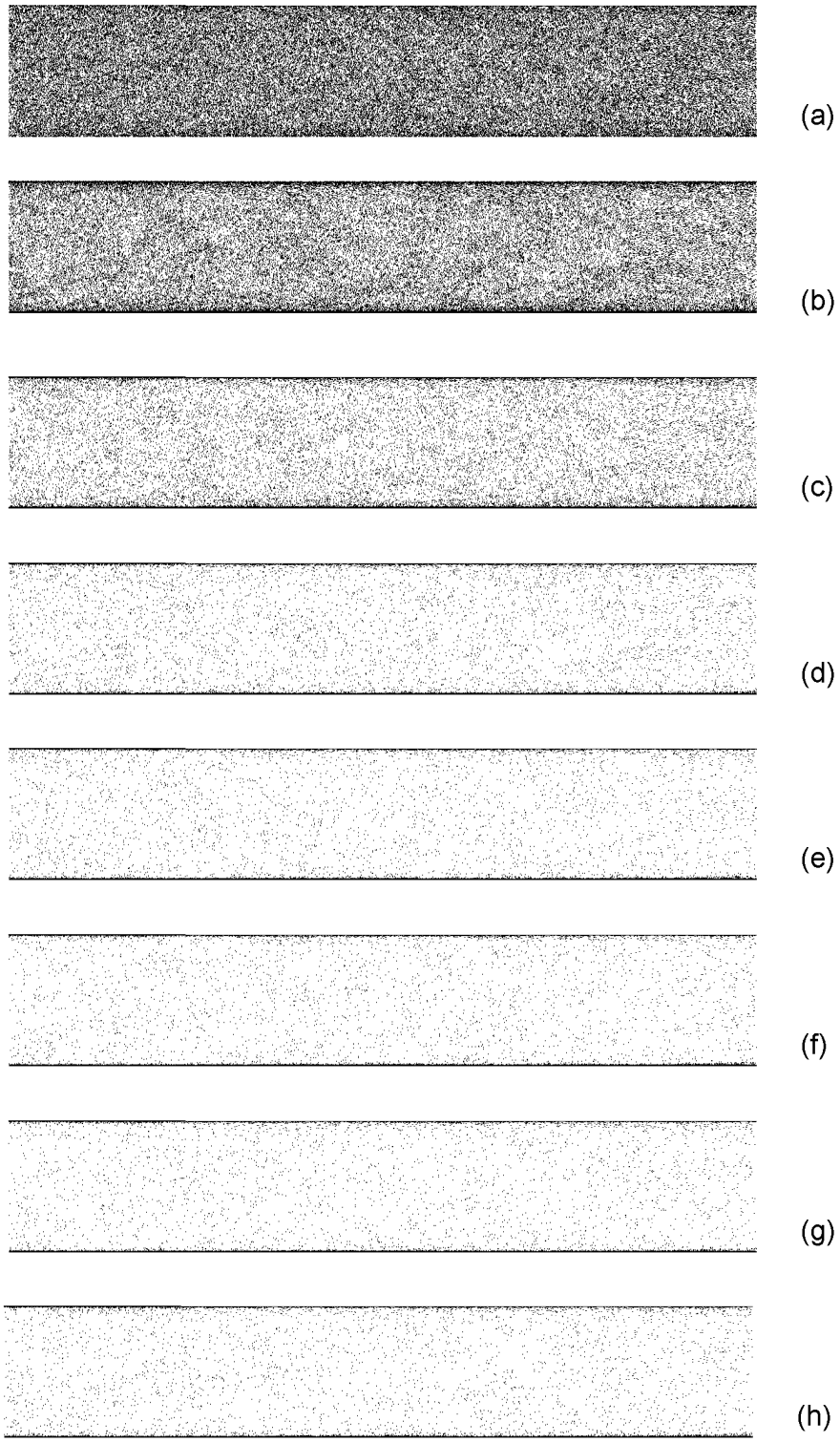

Figure 3.7 Particle distribution after 180 flow through times in the plane turbulent channel. Particles are projected onto a spanwise cross section. $St^+ = 1.45, 5.79, 11.57, 23.14, 34.71, 46.29, 57.86, 69.43$ (plots a-h)

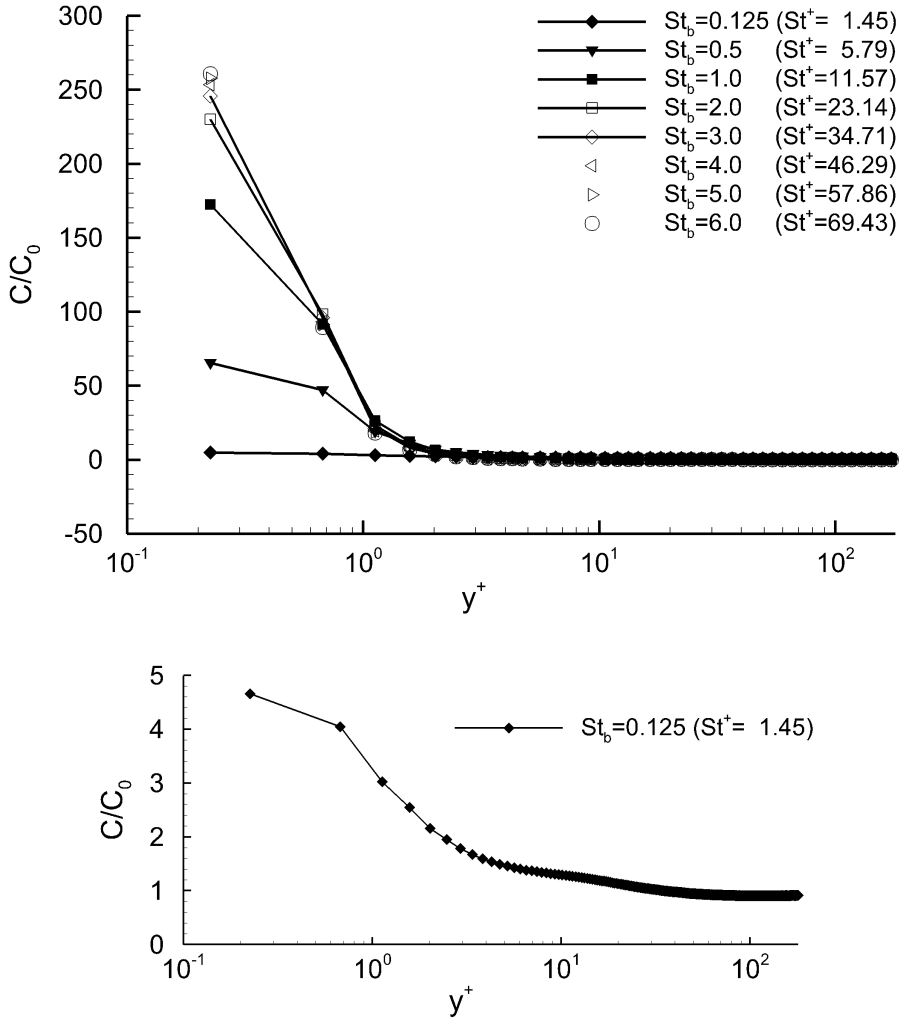

Figure 3.8 Particle mean concentration across the half channel height in the plane turbulent channel.

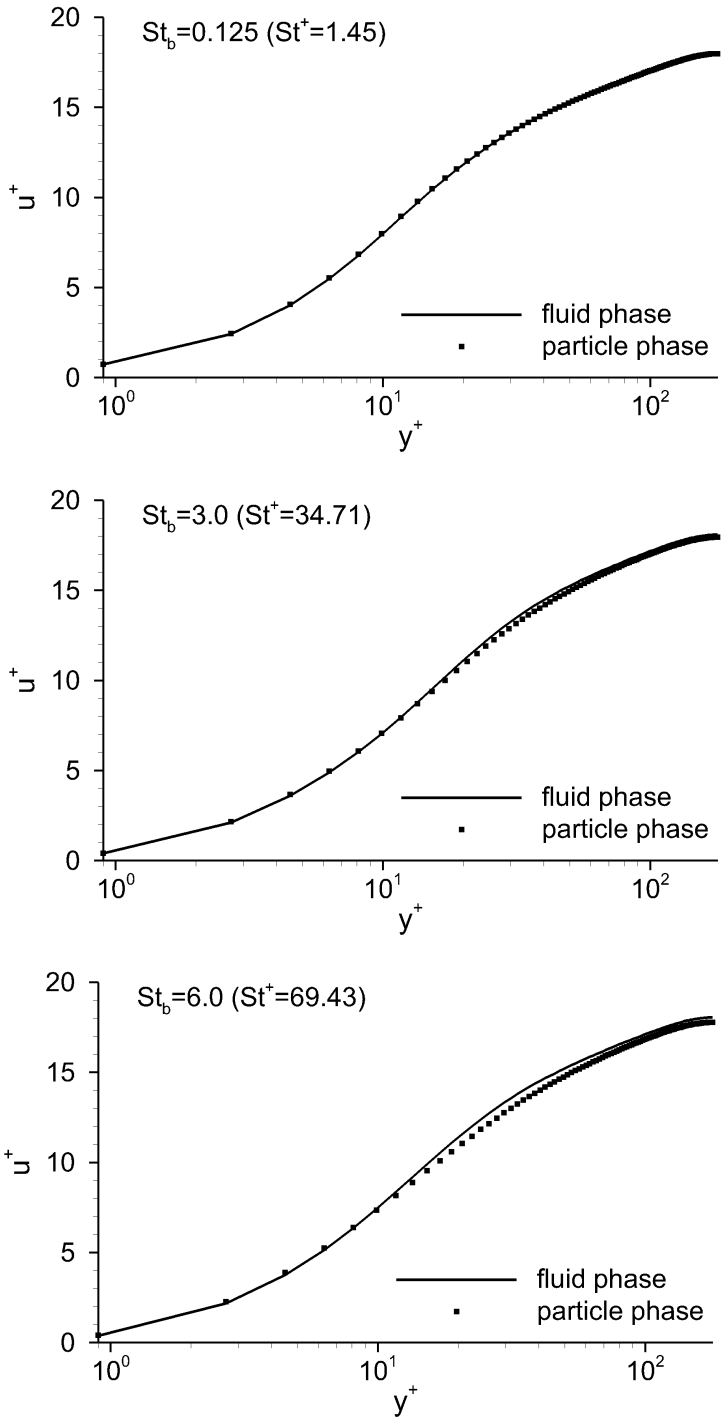

Figure 3.9 Particle mean streamwise velocity across the half channel height in the plane turbulent channel.

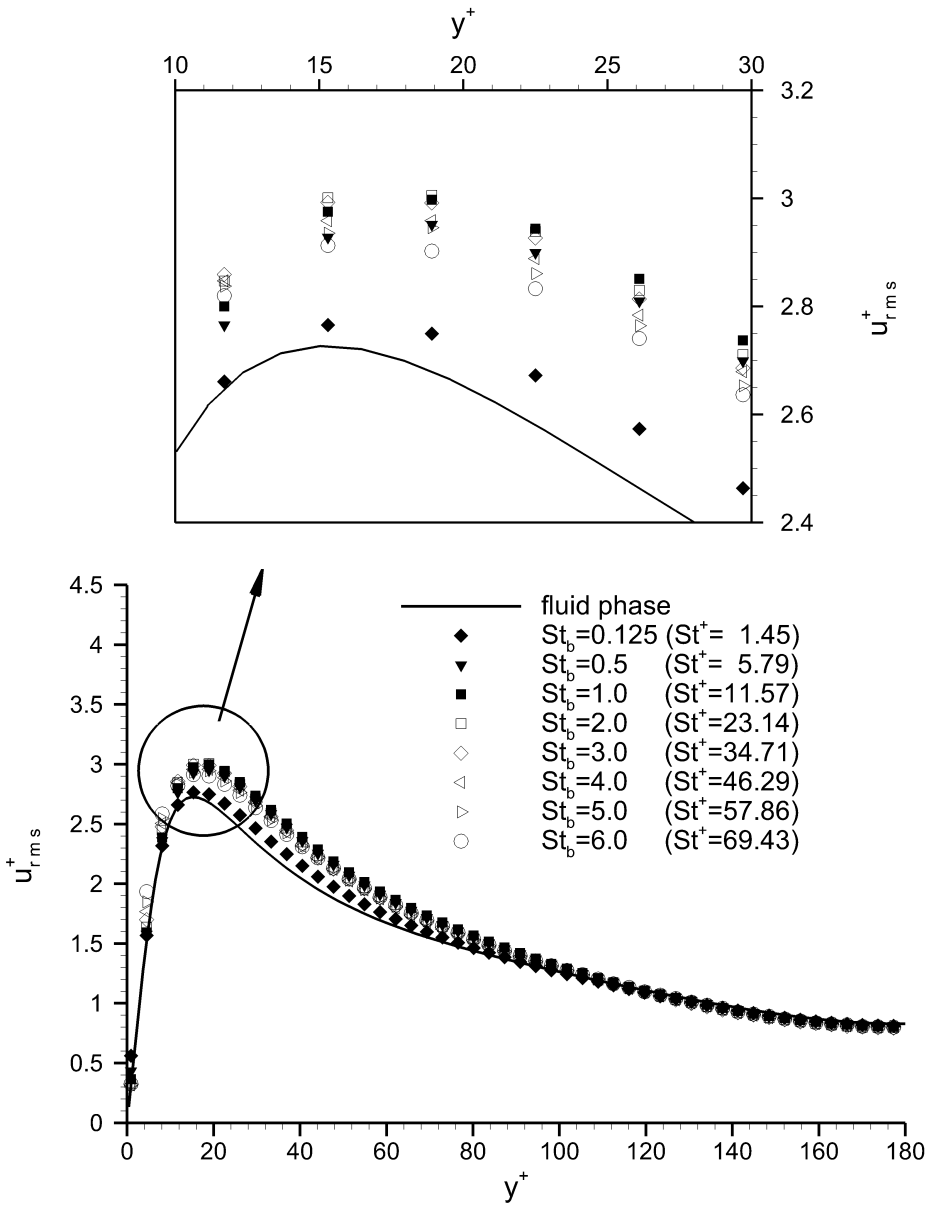

Figure 3.10 Particle root mean square velocity fluctuations in the streamwise direction across the half channel height in the plane turbulent channel.

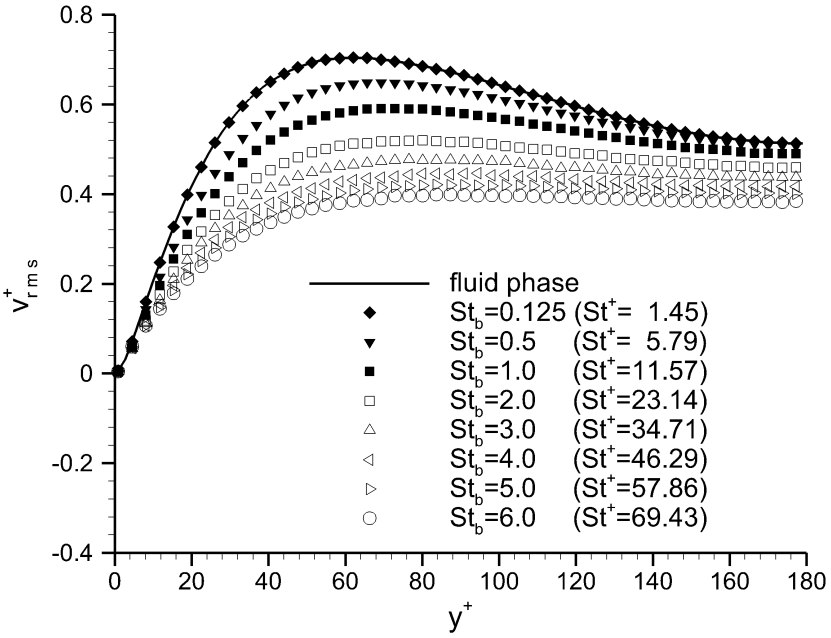

Figure 3.11 Particle root mean square velocity fluctuations in the wall-normal direction across the half channel height in the plane turbulent channel.

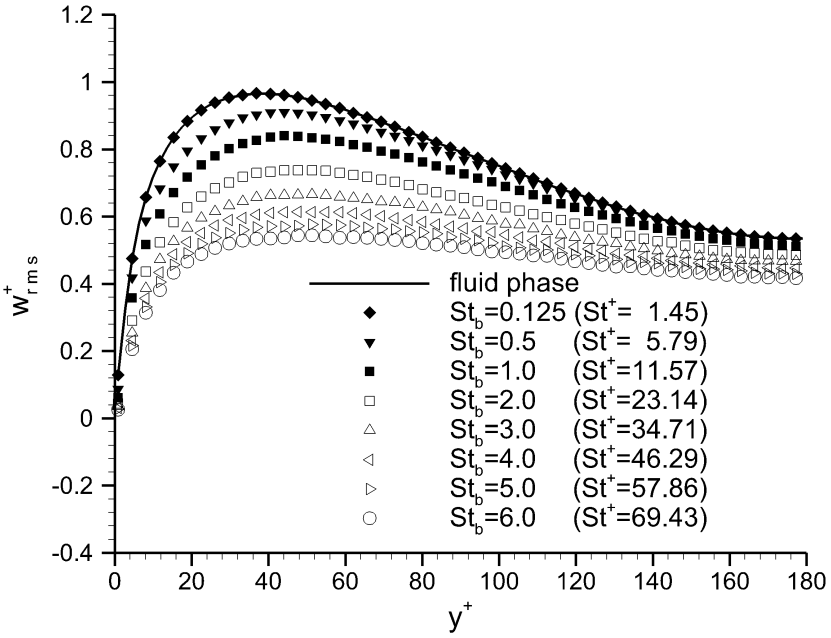

Figure 3.12 Particle root mean square velocity fluctuations in the spanwise direction across the half channel height in the plane turbulent channel.

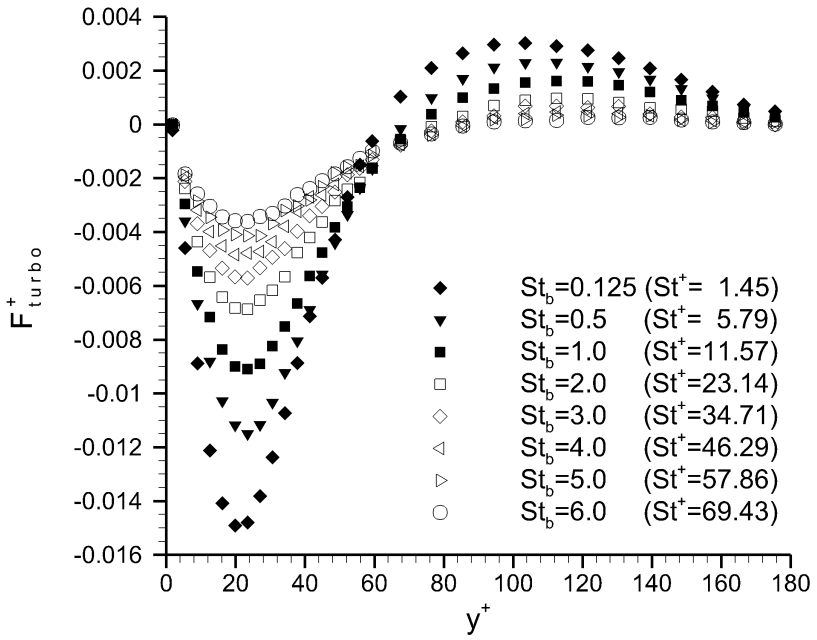

Figure 3.13 Particle turbophoretic force across the half channel height in the plane turbulent channel.

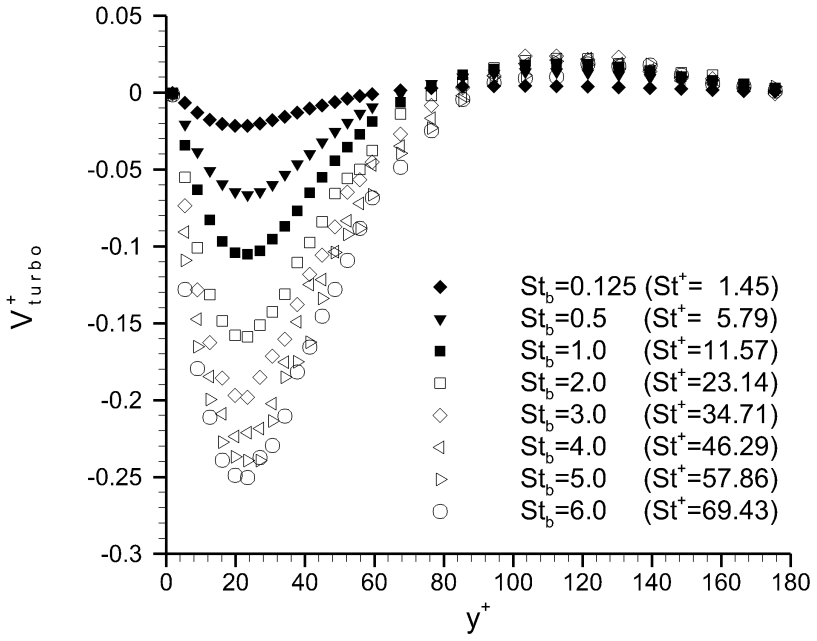

Figure 3.14 Particle turbophoretic velocity across the half channel height in the plane turbulent channel.

CHAPTER 4. PARTICLE MOTION IN A U-SHAPED TURBULENT CHANNEL

This chapter presents the simulation results of particles, with Stokes number St_b ranging from 0.125 to 6.0, inside a U-shaped turbulent channel. First, the equilibrium distribution of particles in the mean flow, without turbulence, is discussed. Then, the distribution of particles in the turbulent flow is presented, followed by the statistics of particle mean velocity and turbulent kinetic energy. The influence of particle-wall collision is examined, and the cause of particle accumulation in the near wall region is discussed. After that, the surface erosion on channel walls caused by particle-wall collisions is reported. Finally, particle preferential distribution in the spanwise direction is presented.

4.1 Particle Distribution in the Mean Flow

In a plane channel, the near-wall high concentration of particles is caused by turbophoresis, as discussed in the previous chapter. In a U-shaped channel, turbophoresis may still play an important role in the straight sections, but particle inertia becomes dominant in the curved section. To isolate the effect of particle inertia from turbulent convection, particle motion in a mean flow, without turbulence, was simulated. Sample streamlines of the mean flow are displayed in Figure 4.1. Figure 4.2 shows examples of the trajectories of particles that are released from various positions in the inlet plane, with their velocity equal to the velocity of the local fluid. All particles, except those released near the outer wall, travel through the U-shaped channel within 4 flow through times. Particles released near the outer wall move quite slowly and have not left the curved section after 23 flow through times, as shown in plot a ($St_b = 0.125$).

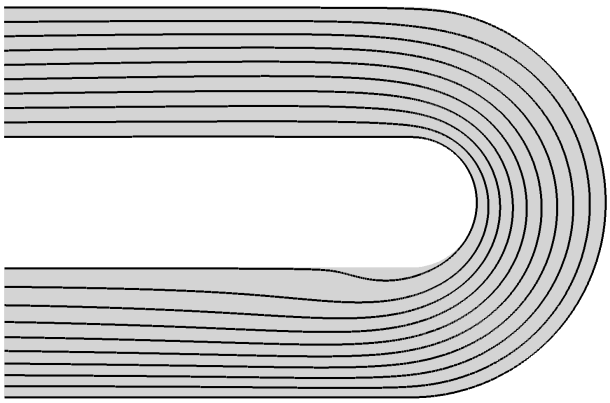

Figure 4.1 Sample streamlines in the mean flow inside the U-shaped channel.

Without turbulent disturbances, particles of all Stokes numbers (plots a-h) move along the streamlines of the mean flow until they enter the curved section. In the curved section, particles are subjected to Stokes drag and centrifugal acceleration. While the centrifugal acceleration throws particles toward the outer wall, the Stokes drag has the tendency to keep particles with the flow. The centrifugal force is dominant near the inner bend, thus particles are thrown away from the inner bend at all Stokes numbers (plots a-h). Particles of larger Stokes numbers can move farther away from the inner bend, because the influence of the Stokes drag diminishes as St_b increases. In fact, for $St_b \geq 1.0$ (plots c-h), all particles are thrown onto the outer bend by centrifugal acceleration. For these Stokes numbers, the centrifugal acceleration is still dominant near the outer bend and the Stokes drag cannot prevent particles from impacting the outer wall. For $St_b \leq 0.5$ (plots a-b), the Stokes drag becomes comparable to the centrifugal acceleration near the outer bend, which reduces both the number and the intensity of collisions between particles and the outer wall. At $St_b = 0.5$ (plot b), about 2/3 of particles impact the outer wall at small impingement angles and the collisions are too weak to expel particles away from the wall. At $St_b = 0.125$ (plot a), no particle-wall collision is seen, though particles that are released within a certain proximity to the outer wall could be thrown onto it. The trajectories of particles after the collisions depend on the coefficient of restitution. In this simulation, elastic reflection is assumed and the coefficient of restitution is 1.0.

The sample trajectories in Figure 4.2 were simulated as a demonstration and particles

were removed after they exited from the U-shaped channel. A simulation of particles inside an infinite serpentine channel was carried out using the U-shaped channel with the periodic boundary condition in the streamwise direction as described in Chapter 2. At the beginning for each Stokes number, 10^5 particles were uniformly distributed inside the U-shaped channel. Figure 4.3 displays a snapshot of particle distribution after 38 flow through times for each Stokes number. The z coordinate is projected onto a spanwise cross-section by placing a dot at the x-y coordinate. At $St_b = 0.125$ (plot a), particles accumulate and form a line near the center of the U-shaped channel. To understand this result, the S-shaped channel in Figure 2.2 should be recalled. The outer wall of the first U-shaped channel becomes the inner wall of the second U-shaped channel. Centrifugal acceleration throws particles toward this wall (the outer wall) in the first U-shaped channel and then away from this wall (the inner wall) in the second U-shaped channel. As particles move through the infinite serpentine channel, they accumulate to an equilibrium trajectory near the center of the U-shaped channel. The equilibrium trajectory shifts toward the walls as St_b increases from 0.125 (plot a) to 0.5 (plot b). At $St_b = 1.0$ (plot c), the accumulated particles impact the outer bend at the exit of the curved section, and the collisions disperse particles into multiple trajectories. These trajectories are adjacent to each other, except in the curved section. At $St_b = 2.0$ (plot d), the equilibrium trajectories become scattered and particles collide with the outer wall multiple times due to the curvature of the bend. As St_b increases from 2.0 to 6.0 (plots d-h), particle-wall collisions become more severe and particles disperse into more trajectories. At $St_b = 6.0$ (plot h), the equilibrium trajectories spread across the straight section. In general, centrifugal acceleration causes particles to cluster while particle-wall collision causes particle trajectories to disperse. The primary purpose of this simulation, however, was to show the consequences of particle inertia in the absence of turbulence. The simulation results of particle motion in the mean flow will be compared with those in the turbulent flow in order to explore the effect of turbulence on particle motion in the U-shaped channel.

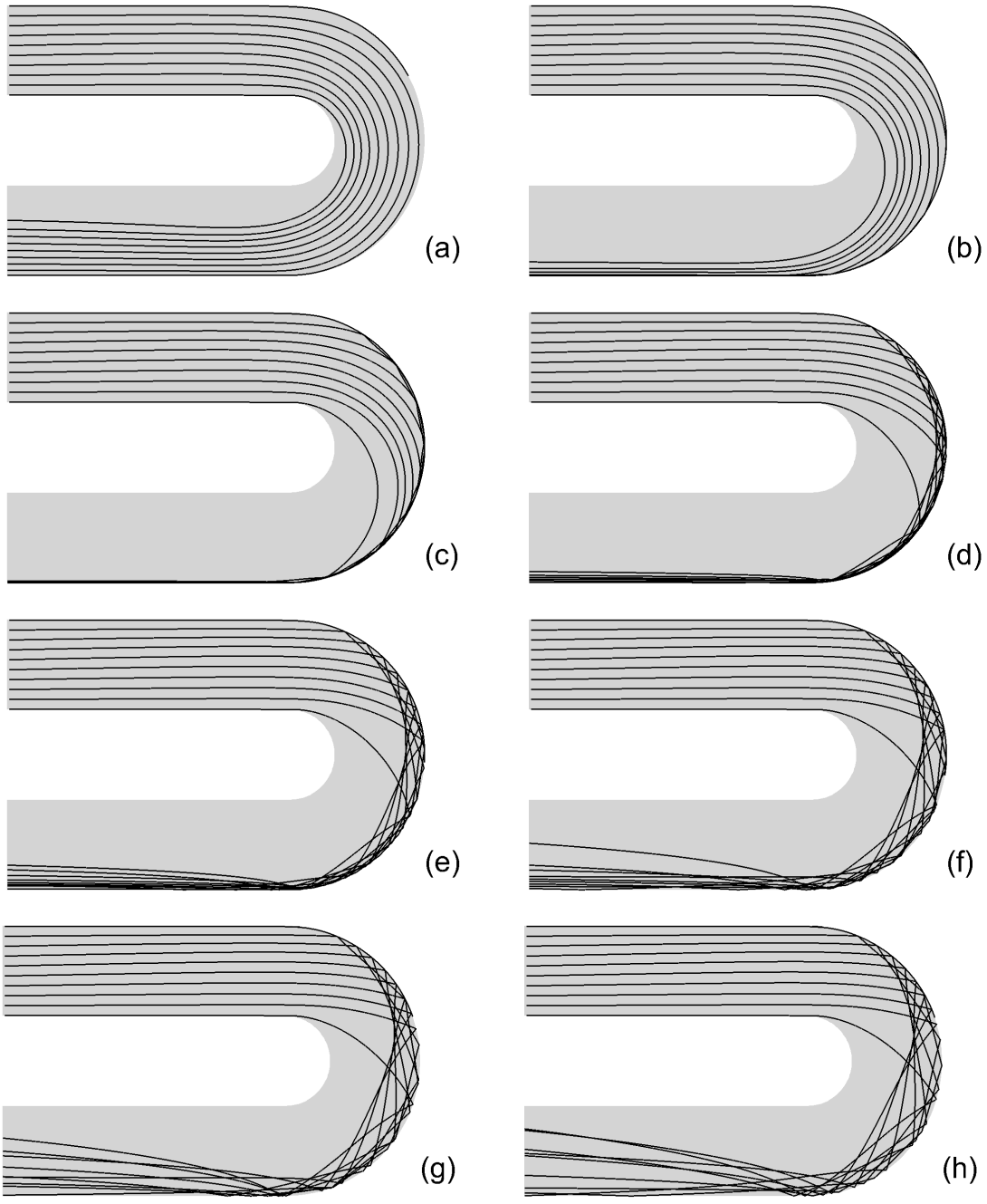

Figure 4.2 Sample trajectories of particles in the mean flow inside the U-shaped channel. $St_b = 0.125, 0.5, 1, 2, 3, 4, 5, 6$ (plots a-h)

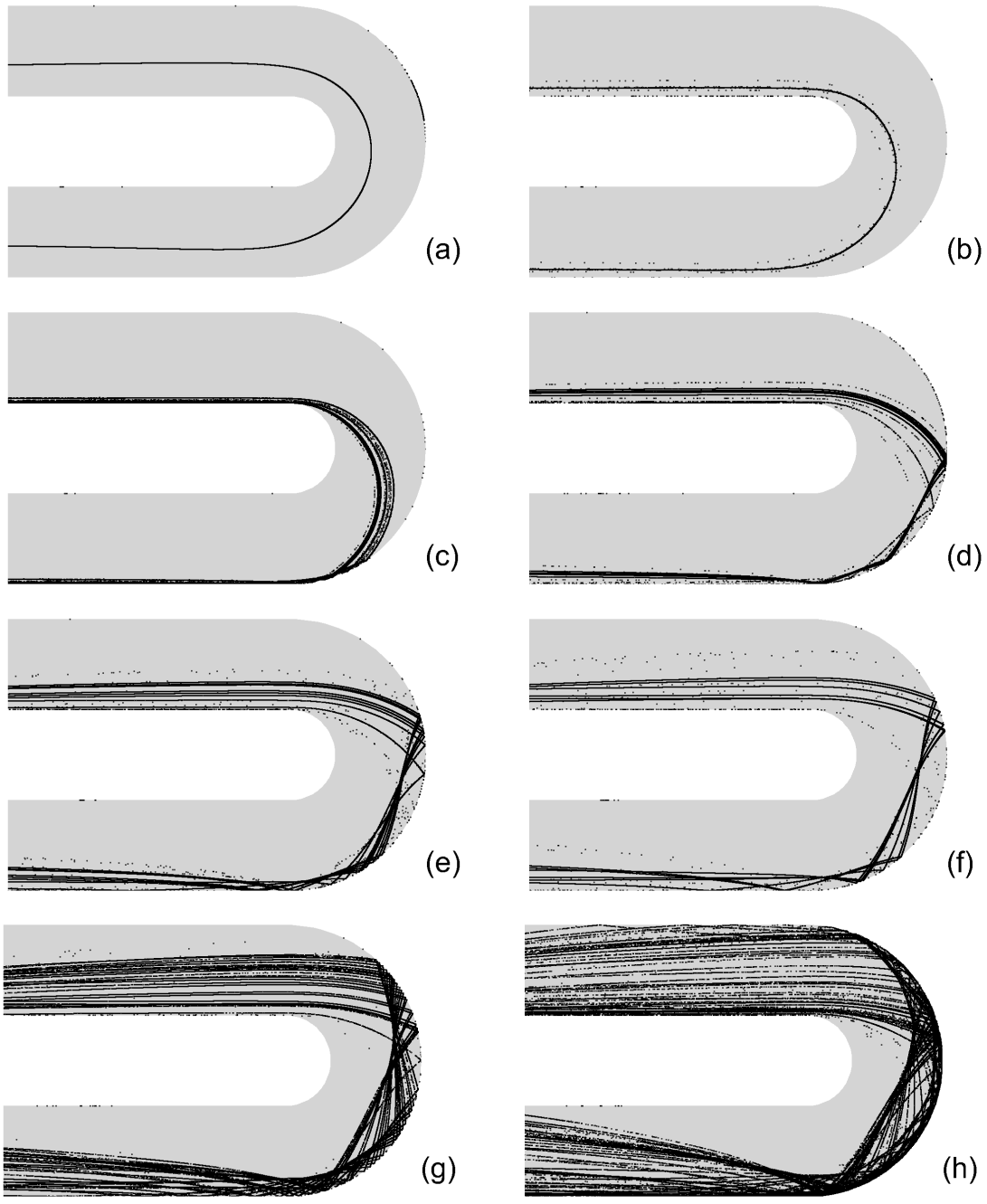

Figure 4.3 Equilibrium distribution of particles in the mean flow inside the U-shaped channel. $St_b = 0.125, 0.5, 1, 2, 3, 4, 5, 6$ (plots a-h)

4.2 Particle Distribution in the Turbulent Flow

The first indication of turbulent influence on particle motion is revealed by comparing sample trajectories of particles in the mean flow (Figure 4.2) and those in the turbulent flow (Figure 4.4). In Figure 4.2, particles with $St_b \leq 1.0$ (plots a-c) are accumulated by the centrifugal acceleration in the absence of turbulence. At $St_b = 1.0$ (plot c), the centrifugal acceleration throws all particles onto the outer bend. In Figure 4.4, by contrast, particles of $St_b \leq 1.0$ (plots a-c) are dispersed by turbulence and their trajectories become chaotic. Due to the disturbance in the flow, some particles of $St_b = 1.0$ (plot c) travel through the U-shaped channel without any interaction with the walls. However, the perturbation from the flow cannot prevent particles of $St_b \geq 2.0$ (plots d-h) from impacting the outer wall. Particle trajectories at $St_b \geq 2.0$ are, nevertheless, affected by turbulence, so they are more erratic in Figure 4.4 than in Figure 4.2.

Although the trajectories in Figure 4.4 illustrate the chaos in particle movement caused by turbulent disturbances, the number of sample trajectories is too few to investigate the effect of turbulence on particle motion. Thus, 10^5 particles of each Stokes number were tracked in the instantaneous turbulent flow field from direct numerical simulation. Figure 4.5 presents a snapshot of particle distribution after 40 flow through times for each Stokes number. At this moment, the patterns of particle distribution have developed from the initial uniform distribution. A comparison between Figures 4.3 and 4.5 reveals that the turbulence disperses particles of different Stokes numbers to various degrees and prevents particles from accumulating to an equilibrium trajectory. Therefore, convecting particles by the mean flow (e.g. Edwards *et al.* (2001)) does not provide a good model for particle transport in this flow.

In Figure 4.5, the number of particles in the core region of the channel lessens as St_b increases from 0.125 to 1.0 (plots a-c) but rises as St_b increases from 2.0 to 6.0 (plots d-h). The instantaneous distribution of particles is lumpy, possibly because of preferential concentration in convergence regions of the eddy field. This is not seen in the mean concentration shown in Figure 4.6. Particle concentration is computed as the number density of particles inside each cell of a uniformly spaced grid. In each plot of Figure 4.6, the mean concentration is averaged from

2940 snapshots of particle instantaneous distribution collected during 24 flow through times. At the beginning, particles are uniformly distributed and the initial concentration C_0 is constant throughout the channel. The ratio of C to C_0 is larger than 1.0 where particle concentration is higher than the initial concentration, and is smaller than 1.0 where particle concentration is lower than the initial concentration. Thus, C/C_0 is defined as a non-dimensional concentration and will be referred to as 'particle concentration' in the rest of this chapter.

At all Stokes numbers (plots a-h), particles accumulate near the inner wall in the first straight section of the U-shaped channel, where the mean concentration is observed to be higher than 1.0. As the accumulated particles move into the curved section, they form one or more plumes. At $St_b = 0.125$ (plot a), turbulence spreads the plume at the entrance of the curved section. At $St_b = 0.5$ (plot b), a plume with concentration higher than 1.0 is formed. As St_b increases from 0.5 to 2.0 (plots b-d), the plume shifts upward in the curved section. At $St_b = 2.0$ (plot d), a second plume appears on top of the first one. This is due to the thick layer of particles accumulated on the inner wall in the first straight section. Particles on the top of the near-wall high concentration move much faster than those adjacent to the wall, so they are carried by inertia in a nearly straight beam onto the outer bend. As St_b increases from 2.0 to 6.0 (plots d-h), the second plume lengthens while the first one shrinks. Particles within the plumes are dispersed by turbulence as they leave the inner bend. However, the centrifugal acceleration is dominant and a region adjacent to the inner bend is consistently devoid of particles. As St_b increases from 2.0 to 6.0 (plots d-h), this zero-concentration region expands, and so does the high concentration region adjacent to the outer bend.

Inside the particle accumulation along the outer bend, the mean concentration may vary by orders of magnitude, which is not exhibited in Figure 4.6. A better view of the high concentration regions is shown in Figure 4.7, which presents the profiles of $log(C/C_0 + 1)$ at locations around the U-shaped channel. For $St_b \geq 2.0$ (plots d-h), the concentration in the region adjacent to the outer bend does not decrease monotonically in the wall-normal direction. At $St_b = 2.0$ (plot d), particle-wall collisions on the upper part of the outer bend repel particles away from the outer bend and produce a band of high concentration parallel to the near-wall accumulation. Particles in both high concentration regions are dispersed by turbulence, but

the concentration in the space between them is still lower. As St_b increases from 2.0 to 6.0 (plots d-h), the band shifts toward the center of the curved section. For $St_b \geq 3.0$ (plots e-h), particle-wall collisions on the lower part of the outer bend create a second band of high concentration between the first one and the near-wall accumulation.

In the straight section after the curved section, particle concentration is higher near the lower wall due to the accumulation of particles near the outer bend in the curved section. By recalling the S-shaped channel in Figure 2.2, the lower wall in the second straight section connects to the lower wall in the first straight section. Thus the accumulation on the lower wall at the entrance of the U-shaped channel continues the accumulation on the lower wall at the exit. As St_b increases from 0.125 to 1.0 (plots a-c), the concentration along the lower walls rises from the order of 10 to the order of 100. It diminishes to the order of 10 as St_b increases from 1.0 to 6.0 (plots c-h). Along the upper wall, high concentration regions are only observed at $St_b \leq 1.0$ (plots a-c), which may be caused by turbophoresis. The possible cause of particle accumulation along the walls will be further discussed after particle velocity is investigated.

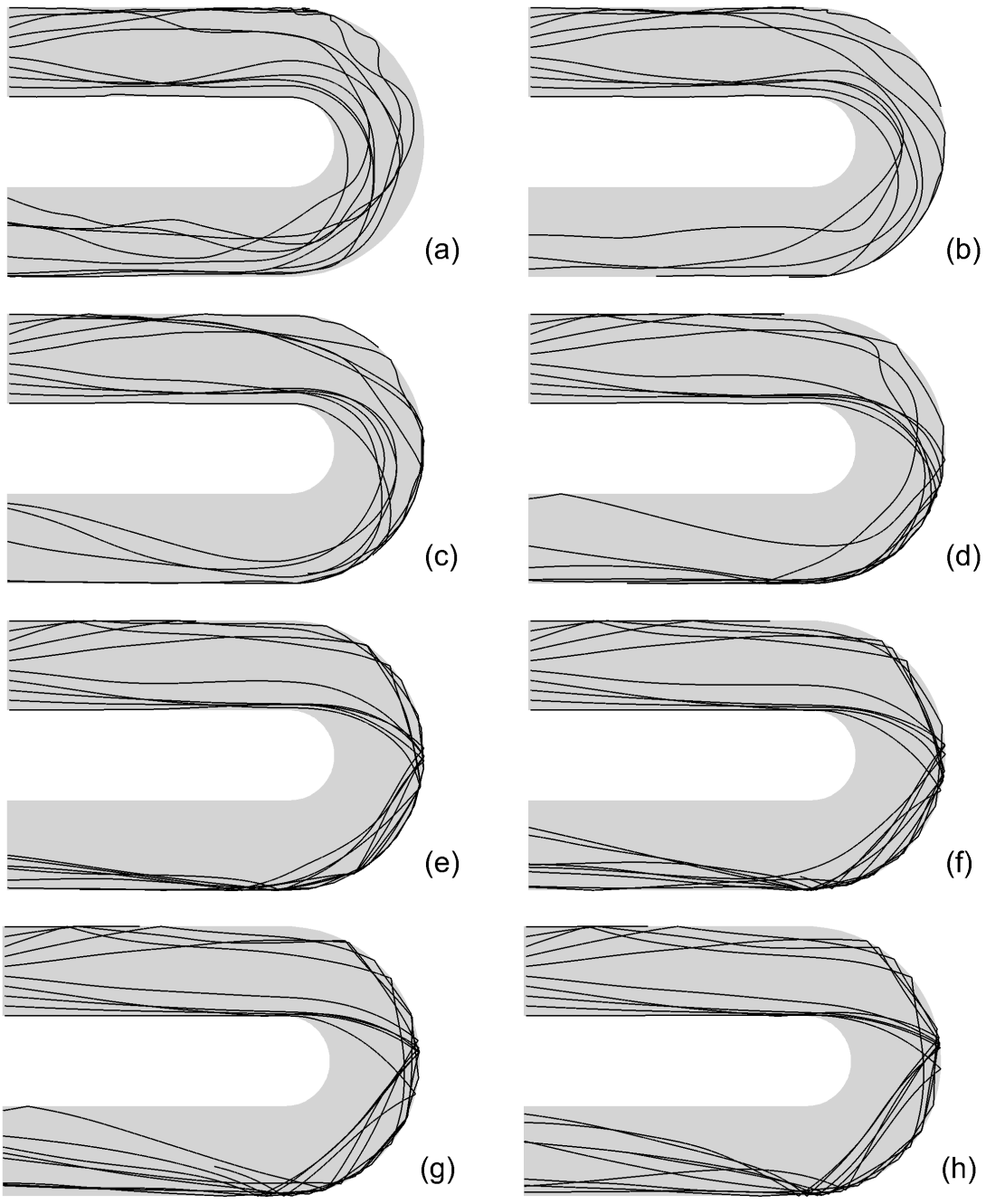

Figure 4.4 Sample trajectories of particles in the DNS turbulent flow inside the U-shaped channel. $St_b = 0.125, 0.5, 1, 2, 3, 4, 5, 6$ (plots a-h)

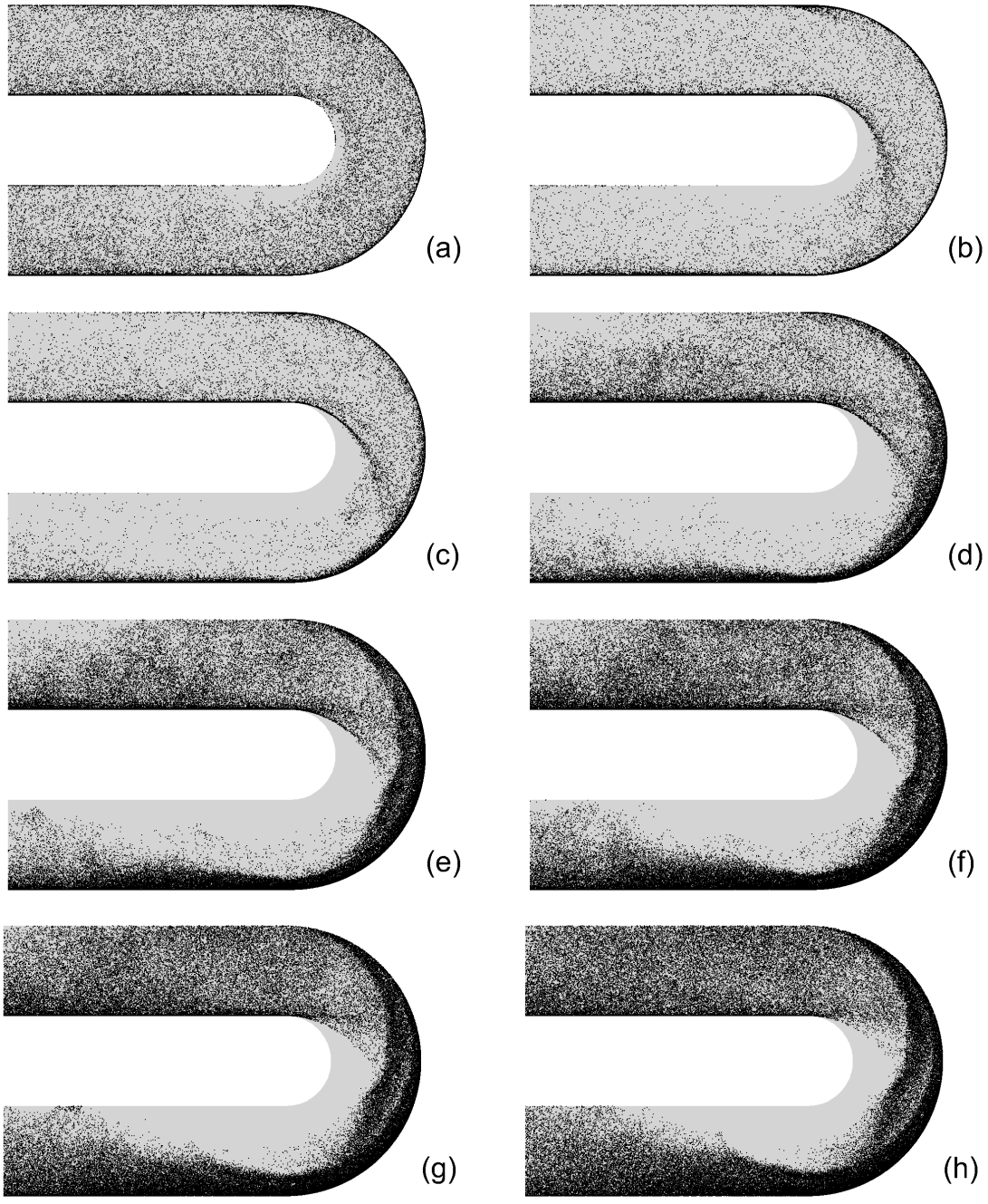

Figure 4.5 Instantaneous distribution of particles in the DNS turbulent flow inside the U-shaped channel. $St_b = 0.125, 0.5, 1, 2, 3, 4, 5, 6$ (plots a-h)

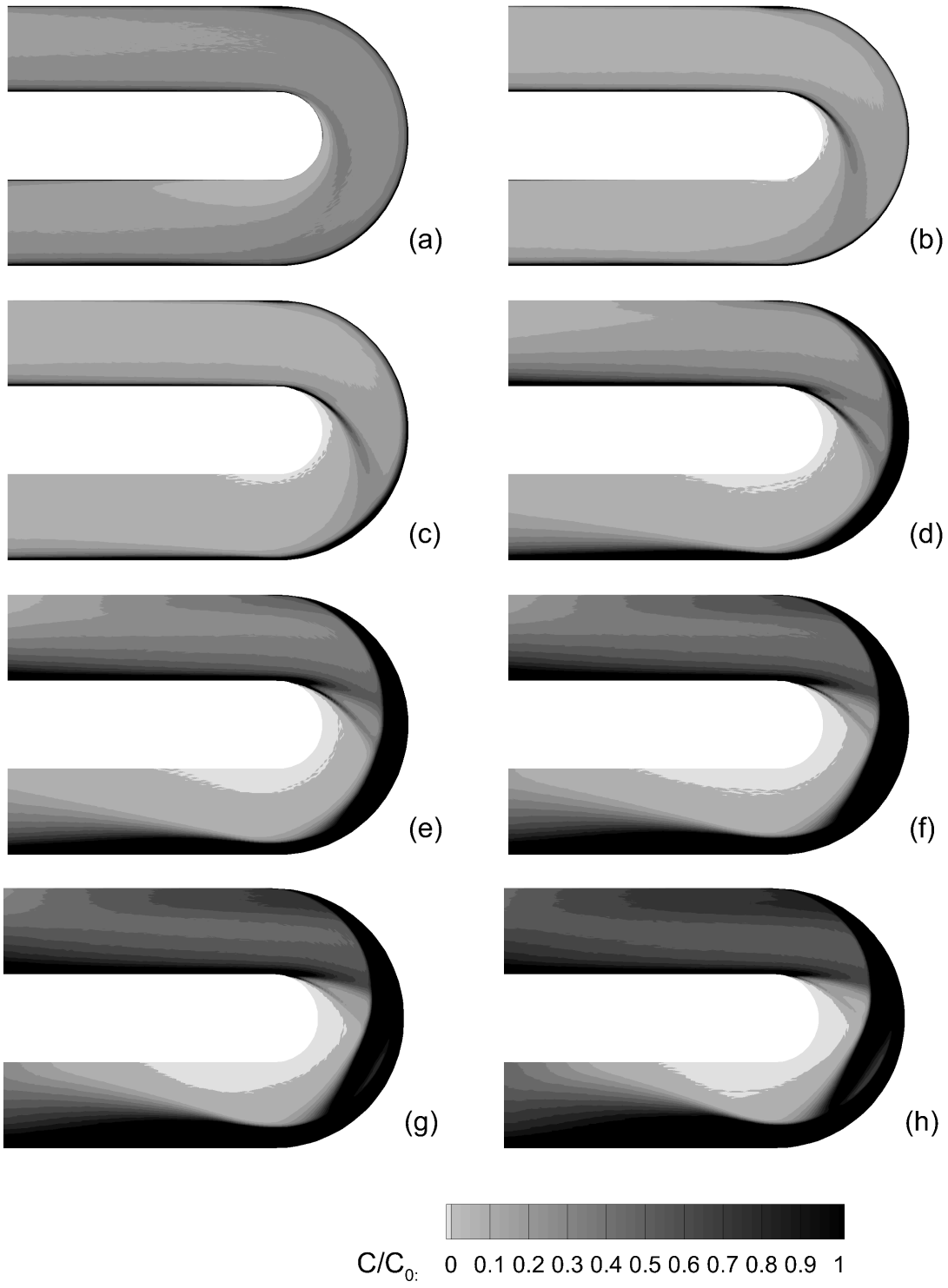

Figure 4.6 Contours of particle mean concentration in the DNS turbulent flow inside the U-shaped channel. $St_b = 0.125, 0.5, 1, 2, 3, 4, 5, 6$ (plots a-h)

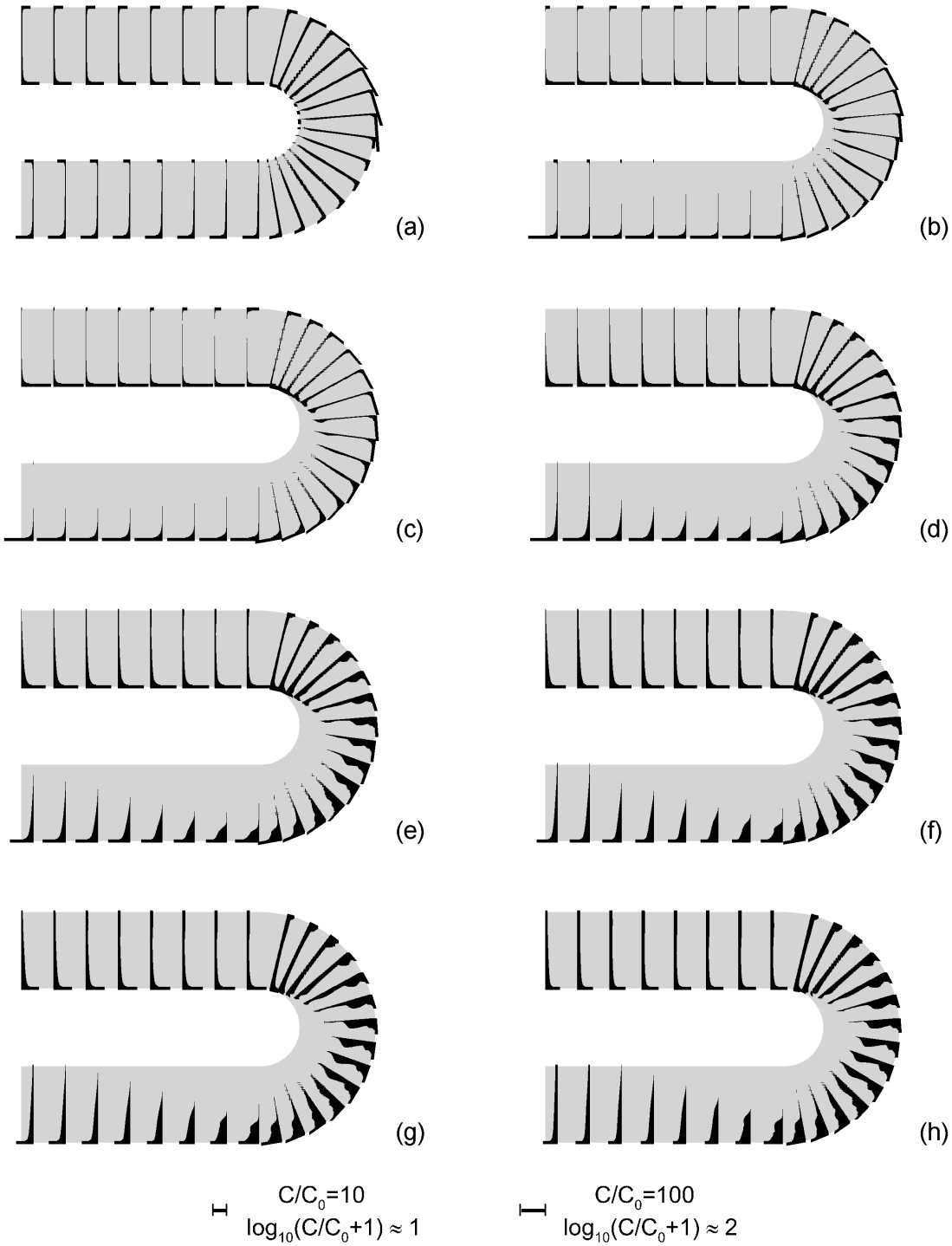

Figure 4.7 Particle mean concentration profiles in logarithm in the DNS turbulent flow inside the U-shaped channel. $St_b = 0.125, 0.5, 1, 2, 3, 4, 5, 6$ (plots a-h)

4.3 Grid Resolution and Time Convergence Study

As has been mentioned, particle concentration is computed using particles inside cells of a uniformly spaced grid, which differs from the non-uniform grid used in the DNS solver. In the streamwise direction, the cell size in the particle phase statistics is 1/4 that of the DNS solver. In the wall normal direction, 801 points are spaced uniformly across the channel and the cell height Δy^+ is about 0.5. In the near-wall high concentration regions where the concentration may rise rapidly, a fine grid is needed. In regions where the concentration is low, for example, in the core region, the number of particles inside a cell of the fine grid may be too few to ensure the accuracy of the statistics. To improve the statistical accuracy, the total number of particles could be increased, or the resolution of the grid for particle phase statistics can be coarsened. In the present simulation, the total number of particles for each Stokes number is 10^5. Due to the high computational cost demanded by simulating a larger number of particles, a coarse grid was adopted in post-processing. The uniformly spaced grid was generated so that the mesh can be agglomerated to meet the required resolution during post-processing. A study of grid resolution and time convergence at $St_b = 0.5$ is presented in this section. This Stokes number ($St_b = 0.5$) is chosen because it has nearly the lowest concentration in the core region, as shown in Figure 4.6, and nearly the highest concentration on both upper and lower walls in the straight sections, as shown in Figure 4.7. Thus, a grid that can meet the resolution requirement in both the core and near-wall regions at $St_b = 0.5$ is appropriate for other Stokes numbers.

Figures 4.8 and 4.9 present the relative standard deviation of particle concentration on four different post-processing grids: MESH-C1, MESH-C2, MESH-C3 and MESH-C4. The mesh number of MESH-C1, MESH-C2, MESH-C3 and MESH-C4 is, respectively, 720×400, 360×200, 180×100 and 90×50, in the streamwise and wall-normal directions. In Figure 4.8, the relative standard deviation is based on 10 samples of particle mean concentration and each sample is an average of 588 snapshots of particle instantaneous distribution collected during 5 flow through times. For the samples post-processed on MESH-C1 (plot C1), the relative standard deviation is higher than 10% almost everywhere inside the U-shaped channel. The magnitude in high

concentration regions becomes lower than 10% on MESH-C2 (plot C2). As the post-processing grid is coarsened to MESH-C3 (plot C3), the relative standard deviation is lower than 10% throughout the U-shaped channel except in the zero-concentration region and its neighboring area. No significant improvement is seen as the grid is coarsened from MESH-C3 (plot C3) to MESH-C4 (plot C4). The same trend is observed in Figure 4.9, in which the relative standard deviation is based on 6 samples of particle mean concentration and each sample is an average over 8 flow through times. As the sample time increases from 5 flow through time (Figure 4.8) to 8 flow through time (Figure 4.9), the relative standard deviation in most regions decreases from 10% to 7.5%. The mean concentration presented in this chapter is averaged over 24 flow through times on MESH-C3 and the relative standard deviation is expected to be lower than 5%.

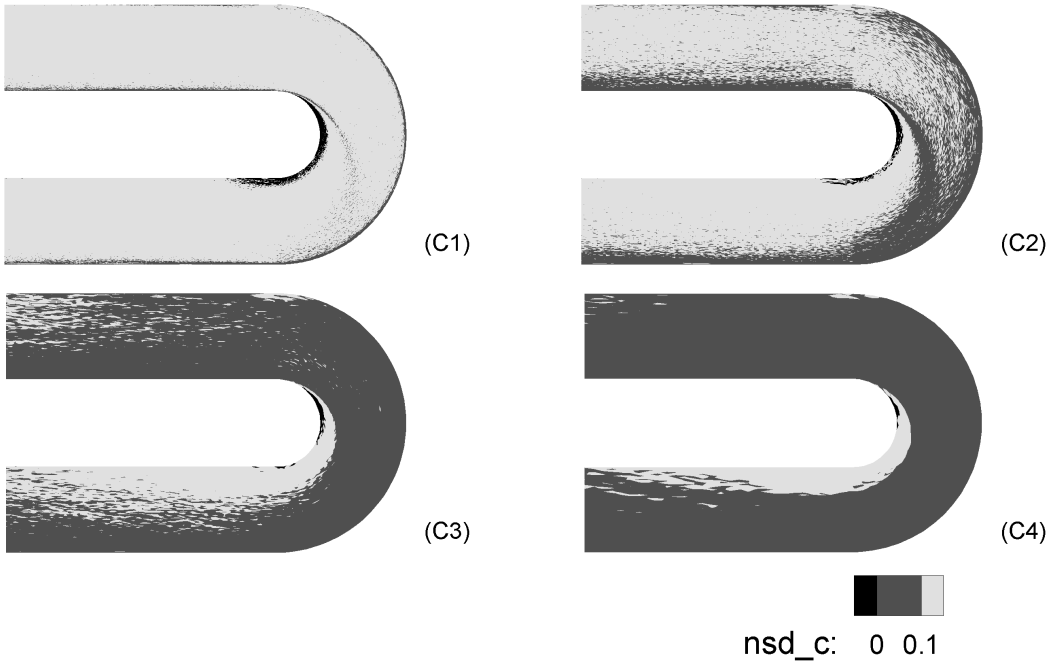

Figure 4.8 Relative standard deviations of particle mean concentration over 5 flow through times. ($St_b = 0.5$)

Particle concentration at the entrance of the U-shaped channel on different post-processing grids is compared in Figure 4.10. In plots m-1, m-2 and m-3, the concentration profile on MESH-C4 is compared with those on MESH-C1, MESH-C2 and MESH-C3, respectively. Along the horizontal axis, d is the distance to the inner wall, which is 0 on the inner wall and 2 on

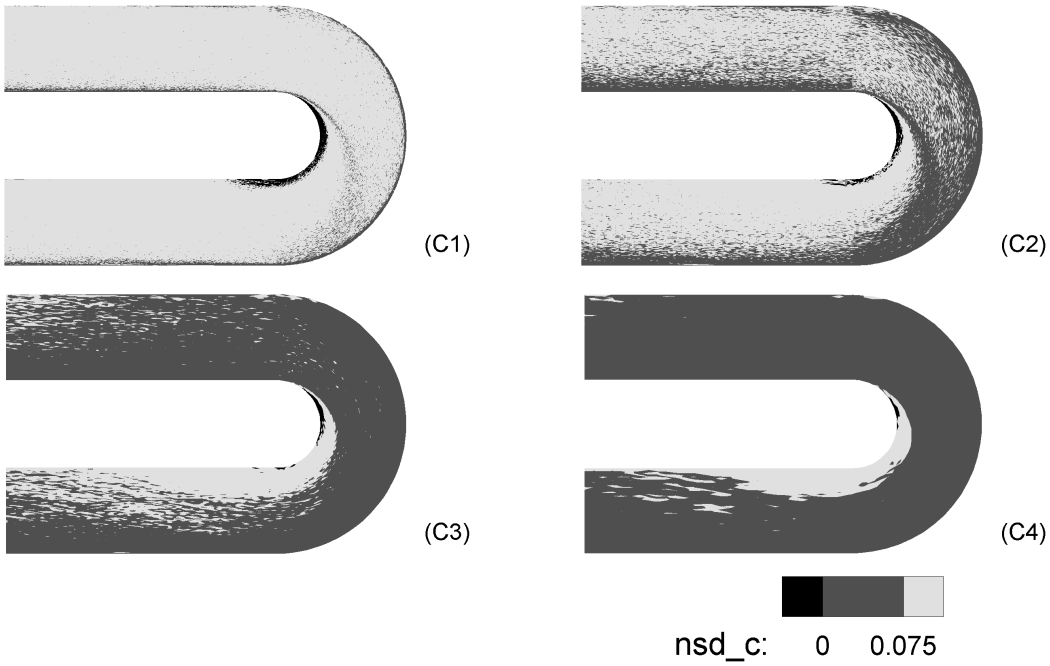

Figure 4.9 Relative standard deviations of particle mean concentration over 8 flow through times. ($St_b = 0.5$)

the outer wall. The concentration profiles of MESH-C1 and MESH-C2 oscillate in the region where the concentration is lower than 0.3 and 0.1, respectively. This is caused by the small size of cells on MESH-C1 and MESH-C2. In plot m-3, the results on MESH-C3 and MESH-C4 agree except in near-wall regions where a fine mesh may be required. The mean concentration profile on MESH-C1, the finest mesh, is compared with those on MESH-C4 and MESH-C3 in plots m-1 and m-4. A good agreement in the near-wall regions is seen between MESH-C1 and MESH-C3. Thus, the post-processing grid MESH-C3 is coarse enough in the core region and fine enough in near-wall regions. Figure 4.11 compares the profiles of particle mean streamwise velocity at the entrance of the U-shaped channel on the four different post-processing grids. It shows again that MESH-C3 can meet the resolution requirement in both the core and near-wall regions.

The study of time convergence is conducted at the entrance of the U-shaped channel on MESH-C3. The mean concentration averaged over 12, 24 and 48 flow through times are compared in Figure 4.12. The three profiles FLOW-40-52, FLOW-40-64 and FLOW-40-88 represent the statistics from 40 to 52 flow through times, from 40 to 64 flow through times, and from 40 to

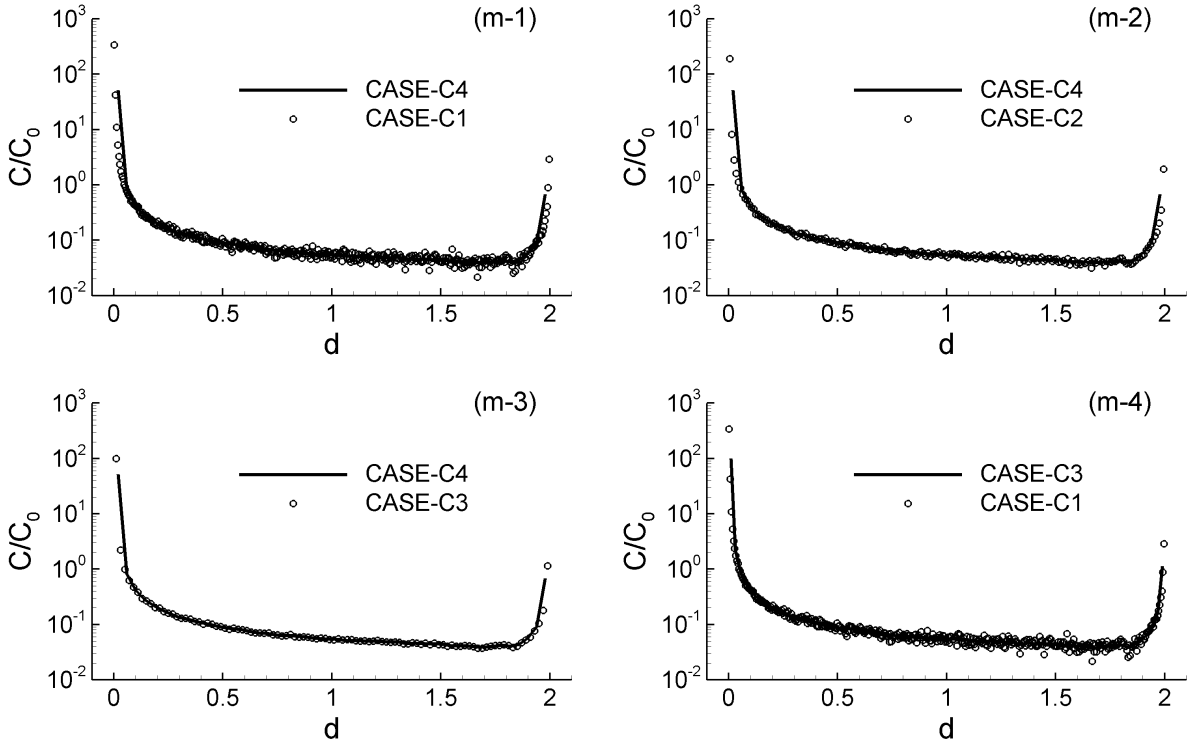

Figure 4.10 Particle mean concentration at the entrance on MESH-C1, MESH-C2, MESH-C3 and MESH-C4. d represents distance from inner wall, with 0 being inner wall and 2 being outer wall. ($St_b = 0.5$)

88 flow through times, respectively. The maximum relative percentage difference of the mean concentration is 14% between FLOW-40-52 and FLOW-40-88 and 5% between FLOW-40-64 and FLOW-40-88. Figure 4.13 shows particle mean streamwise velocity profiles of FLOW-40-52, FLOW-40-64 and FLOW-40-88. The maximum relative percentage difference of the mean streamwise velocity is 10% between FLOW-40-52 and FLOW-40-88 and 2% between FLOW-40-64 and FLOW-40-88. Because the focus of the current project is the pattern of particle motion inside the U-shaped channel, the difference between FLOW-40-64 and FLOW-40-88 is acceptable. Thus, all the statistics presented in this chapter were collected from 40 to 64 flow through times on MESH-C3 unless otherwise specified.

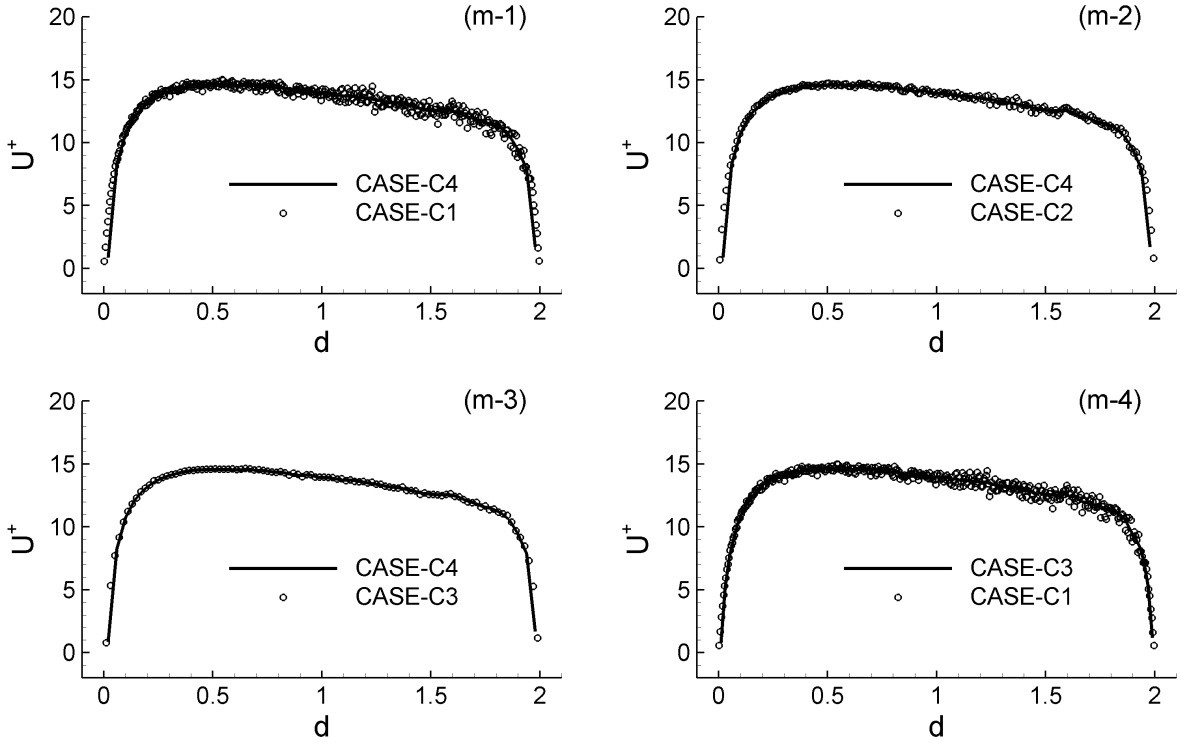

Figure 4.11 Particle mean streamwise velocity at the entrance on MESH-C1, MESH-C2, MESH-C3 and MESH-C4. d represents distance from inner wall, with 0 being inner wall and 2 being outer wall. ($St_b = 0.5$)

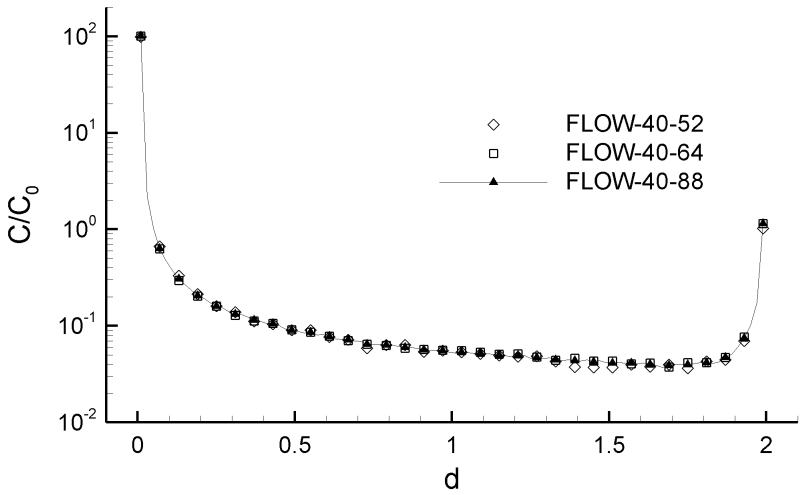

Figure 4.12 Particle mean concentration at the entrance averaged over 12, 24 and 48 flow through times. d represents distance from inner wall, with 0 being inner wall and 2 being outer wall. ($St_b = 0.5$)

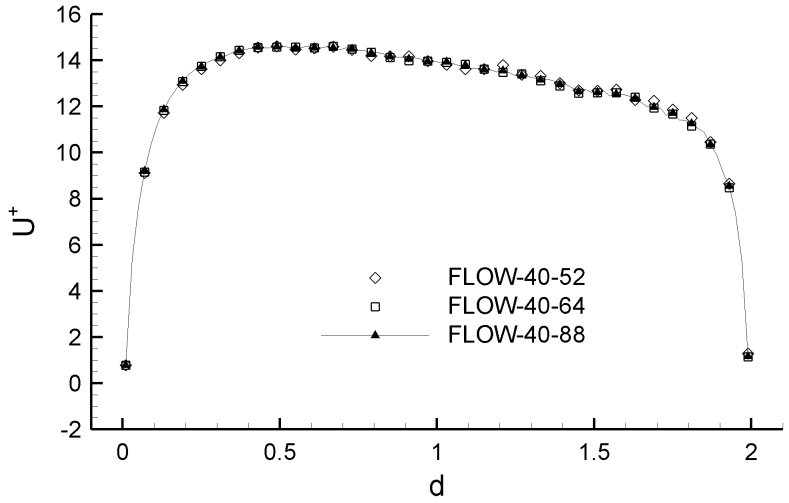

Figure 4.13 Particle mean streamwise velocity at the entrance averaged over 12, 24 and 48 flow through times. d represents distance from inner wall, with 0 being inner wall and 2 being outer wall. ($St_b = 0.5$)

4.4 Particle Velocity in the Turbulent Flow

To better understand how centrifugal acceleration, particle-wall collision, and turbulence influence particle distribution, especially the accumulation of particles on the walls, the mean velocity of particles was investigated. Figure 4.14 compares the mean velocity vectors of particle and fluid phases along the U-shaped channel. In the statistics of the particle phase, particle mean velocity is computed by averaging the velocity of particles inside each statistical cell. The mean velocity of the fluid phase plotted in Figure 4.14 is the corresponding average of the fluid velocity at particle locations. It can differ from those in Figure 2.6, in which the fluid velocity was computed on mesh points of the non-uniform grid in the DNS solver. In Figure 4.14, the velocity vectors of both particle and fluid phases are a bit random in the region adjacent to the zero concentration region, where the number of particles is too few to obtain statistics.

At $St_b = 0.125$ (plot a), particle and fluid mean velocity vectors deviate at a minor angle near the inner bend and almost overlap near the outer bend. The deviation near the outer bend becomes apparent at $St_b = 0.5$ (plot b) and $St_b = 1.0$ (plot c). As St_b increases (plots d-h), particle-wall collisions can expel particles away from the walls. Inside a cell of particle phase statistics in the curved section, some particles may move away from the outer bend after collisions while others move toward the outer bend due to inertia. Particle mean velocity vectors can deviate from fluid mean velocity vectors in the direction toward the outer bend or toward the inner bend. At $St_b = 2.0$ (plot d) and $St_b = 3.0$ (plot e), particle mean velocity vectors still deviate from fluid mean velocity vectors in the direction toward the outer bend. The deviation in both directions is observed at $St_b \geq 4.0$ (plots f-h). At the exit of the curved section, particle mean velocity vectors point to the lower wall of the straight section. For $St_b \leq 1.0$ (plots a-c), particles gradually resume the velocity of the fluid in the straight sections; thus the flow can transport particles to the upper wall. As St_b becomes larger, the inertia shifts the contact point of particles with the upper wall closer to the exit of the U-shaped channel. However, the contact point moves closer to the curved section as St_b increases from 4.0 to 6.0 (plots f-h). For $St_b \geq 2.0$ (plots d-h), some particles move to the upper wall after they impact the outer wall near the exit of the curved section, which shifts the contact point toward the curved section.

Figure 4.14 exposes the difference between particle and fluid mean velocity not only in the direction but also in the magnitude. For example, particles of $St_b \geq 3.0$ (plots f-h) are slower than the fluid inside the straight section. In the curved section where particles deviate from the flow, the magnitude difference between particle and fluid mean velocity cannot be easily observed. The next two figures (4.15 and 4.16) present contour plots of particle mean velocity components U^+ and V^+. The corresponding contour plots of the fluid phase from the DNS solver are shown in Figure 4.17 for comparison.

In Figure 4.17, a positive maximum of the fluid mean velocity component U^+ is located near the inner bend at the entrance of the curved section and a negative maximum is seen inside the second straight section. In Figure 4.15, a similar pattern is exhibited at $St_b \leq 1.0$ (plots a-c), but the area of the positive and negative maximum shrinks as St_b increases. This is due to the reduced response of particles to the acceleration or deceleration of the flow. Both maximum regions disappear at $St_b = 2.0$ (plot d). By this Stokes number, particle-wall collisions become pronounced. When particles collide with the outer bend, their U^+ components can change dramatically, which affects the U^+ component of particle mean velocity near the outer bend. At $St_b = 3.0$ (plot e), a concave shape is seen in the contour of U^+ adjacent to the outer bend. The concavity becomes larger as St_b increases from 3.0 to 6.0 (plots e-h).

The effect of particle-wall collision on the particle mean velocity component U^+ is revealed by superimposing contour lines of particle mean velocity component U^+ on the flooded contour of particle concentration C/C_0 in Figure 4.18. At $St_b = 3.0$ (plot e), the location of the concave portion of the particle phase U^+ contour is in accord with the high concentration regions. Particle-wall collision can either reduce the magnitude of particle velocity component U^+ or alter the value of the U^+ component from positive to negative. Regardless of the specific change, the value of the velocity component U^+ becomes smaller after a particle collides with the outer bend. As particle-wall collisions accumulate particles into the high concentration band, the mean velocity component U^+ of particles along the band is reduced. This creates the concave shape near the outer bend in the contour of particle phase U^+. In plot h ($St_b = 6.0$), a second high concentration band forms and a small concave shape appears on top of this high concentration band and the near-wall accumulation.

Figure 4.16 exposes the effect of particle-wall collision on the particle mean velocity component V^+. In the curved section, particles of $St_b \geq 2.0$ (plots d-h) move faster in the downward direction after they collide with the outer bend. In the straight section, at all Stokes numbers (plots a-h), the particle mean velocity component V^+ is larger than the fluid phase V^+, as shown in Figure 4.17. For $St_b \leq 1.0$ (plots a-c) in Figure 4.16, besides the fluid convection, both turbulent diffusion and turbophoresis may play a role on particle movement toward the upper wall. As St_b increases to 2.0 (plot d), the magnitude of particle mean velocity component V^+ in the straight section after the curved section becomes much larger, which can only be caused by particle-wall collisions on the outer wall near the exit of the curved section. This area of large V^+ component diminishes as St_b increases from 2.0 to 6.0 (plots d-h), though particle-wall collisions become more severe. Unlike the U^+ component, the V^+ component of a particle is reversed when the particle impacts the upper wall. As the collisions on the upper wall become concentrated in the region closer to the exit of the curved section, the average of the V^+ component in the forward region is reduced.

The comparison of particle and fluid mean velocity components illustrates that the difference in particle and fluid mean velocity is the largest at the exit of the curved section. After particles leave the curved section, they gradually resume the velocity of the fluid in the straight section. To expose the influence of the flow on particle motion in the straight section, Figures 4.19-4.21 compare the mean streamwise velocity profiles of particle and fluid phases at Stations 4, 1 and 2, as shown in Figure 2.4. Stations 4, 1 and 2 are located, respectively, at the exit of the curved section, the entrance of the U-shaped channel, and the entrance of the curved section. They also correspond to the entrance, the middle point, and the exit of the straight section in the S-shaped channel. The horizontal axis d in Figures 4.19-4.21 represents the distance from the lower to the upper wall, with 0 being the lower wall and 2 the upper wall.

In Figure 4.19, at the exit of the curved section, particle mean streamwise velocity U^+ of $St_b = 0.125$ (plot a) is slightly lower than fluid phase U^+. As St_b becomes larger (plots a-h), the difference between particle and fluid mean streamwise velocity profiles rises. The full profile of fluid mean streamwise velocity U^+ from $d = 0$ to $d = 2$ can only be observed in plot a, where the magnitude of the fluid phase U^+ increases almost linearly from $d = 0.2$ to $d = 1.5$ and

plunges in both near-wall regions. Inside the first cell adjacent to the lower wall ($d = 0$), the magnitude of the fluid phase U^+ varies with the Stokes number. This is because the velocity of the fluid is collected at locations of particles and the magnitude of the fluid mean velocity depends on the distribution of particles inside statistical cells.

After leaving the curved section, the fluid accelerates near the lower wall and decelerates near the upper wall in the straight section. At the entrance of the U-shaped channel, in Figure 4.20, the profile of fluid mean streamwise velocity U^+ declines linearly from $d = 0.3$ to $d = 1.7$, as shown in plot a. Since particle phase U^+ is smaller than fluid phase U^+ at the exit of the curved section, particles are accelerated by the fluid when they enter the straight section. At the entrance of the U-shaped channel, the particle phase U^+ of all Stokes numbers (plots a-h) becomes closer to fluid phase U^+. Particles of $St_b = 0.125$ can follow the acceleration of the fluid; and the profile of particle phase U^+ overlaps the profile of fluid phase U^+ at $St_b = 0.125$ (plot a). At the entrance of the curved section (Figure 4.21), the fluid velocity rises rapidly near the inner wall due to the strong favorable pressure gradient associated with the convex surface of the inner bend. Even particles of $St_b = 0.125$ (plot a) cannot follow this rapid acceleration of the fluid.

In contrast to the lower wall region, particle concentration is zero or nearly zero adjacent to the upper wall at the exit of the curved section. The velocity of the particle and fluid is not collected when no particle is present, so their average in the zero-concentration region is shown as zero in Figure 4.19 (plots b-h). In the straight section, particles can move toward the upper wall by fluid convection or particle-wall collisions. If a particle is transported to the upper wall by the flow, its velocity should become comparable to the velocity of the local fluid. When a particle moves to the upper wall after it collides with the lower wall, its velocity can be much larger than the velocity of the fluid adjacent to the upper wall. At the entrance of the U-shaped channel (Figure 4.20), for $St_b \leq 1.0$ (plots a-c), the profile of particle mean streamwise velocity U^+ plunges with the profile of fluid phase U^+ in the region adjacent to the upper wall ($d = 2$). For these Stokes numbers, the influence of particle-wall collision on particle motion in the straight section can be ignored. For $St_b \geq 2.0$ (plots d-h), the profile of particle phase U^+ decreases linearly from the core region to the upper wall. Thus, the majority of particles with

$St_b \geq 2.0$ near the upper wall ($d = 2$) at the entrance of the U-shaped channel are caused by particle-wall collisions near the exit of the curved section. The influence of particle-wall collision diminishes along the straight section. At the entrance of the curve section (Figure 4.21), at all Stokes numbers (plots a-h), the profile of particle phase U^+ plunges in the region adjacent to the upper wall ($d = 2$), though particles of $St_b \geq 3.0$ (plots e-h) still move much faster than the fluid.

As particles move from the straight section into the curved section, they are thrown away from the inner bend. Figure 4.22 presents the profiles of particle and fluid mean streamwise velocity V^+ at the middle position of the curved section, which is Station 3 in Figure 2.4. The horizontal axis d in Figure 4.22 represents the distance from the inner to outer bend, with 0 being the inner bend and 2 the outer bend. The zero-concentration range extends as St_b increases from 0.125 to 6.0 (plots a-h), and it is larger than 1/4 of the channel width at $St_b \geq 3.0$ (plots e-h). For $St_b \leq 1.0$ (plots a-c), the profile of particle phase V^+ declines all the way from the core region to the outer bend ($d = 2$). For $St_b \geq 2.0$ (plots d-h), however, the profile of particle phase V^+ goes up suddenly once or twice. This is because particles in the high concentration bands move much faster in the streamwise direction after their collisions on the outer bend. In the space between high concentration regions, the number of particles may be too few to ensure the accuracy of statistics, which explains the discrepancy in the profile of fluid phase V^+ at $St_b \geq 4.0$ (plots f-h).

The study of particle mean velocity exposes the influence of centrifugal acceleration and particle-wall collision on particle motion. The influence of turbulent disturbances is exhibited with contour plots of the particle phase turbulent kinetic energy (tke) shown in Figure 4.23. The maximum tke in the fluid phase occurs inside the separation bubble, as shown in Figure 4.17. A nearly identical pattern is seen at $St_b = 0.125$ (plot a) in Figure 4.23. As St_b increases (plots b-h), particle concentration around the separation bubble is zero or nearly zero, thus this high tke region disappears. At $St_b \leq 1.0$ (plots a-c), the magnitude of tke diminishes with the Stokes number due to the reduced response to turbulent disturbances. At $St_b \geq 2.0$ (plots d-h), however, the magnitude in the region adjacent to the outer bend becomes higher as St_b increases. The large velocity difference in the curved section is caused by particle-wall collision

instead of turbulent perturbation. Thus, for $St_b \geq 2.0$, the computation of tke in the curved section has no meaning.

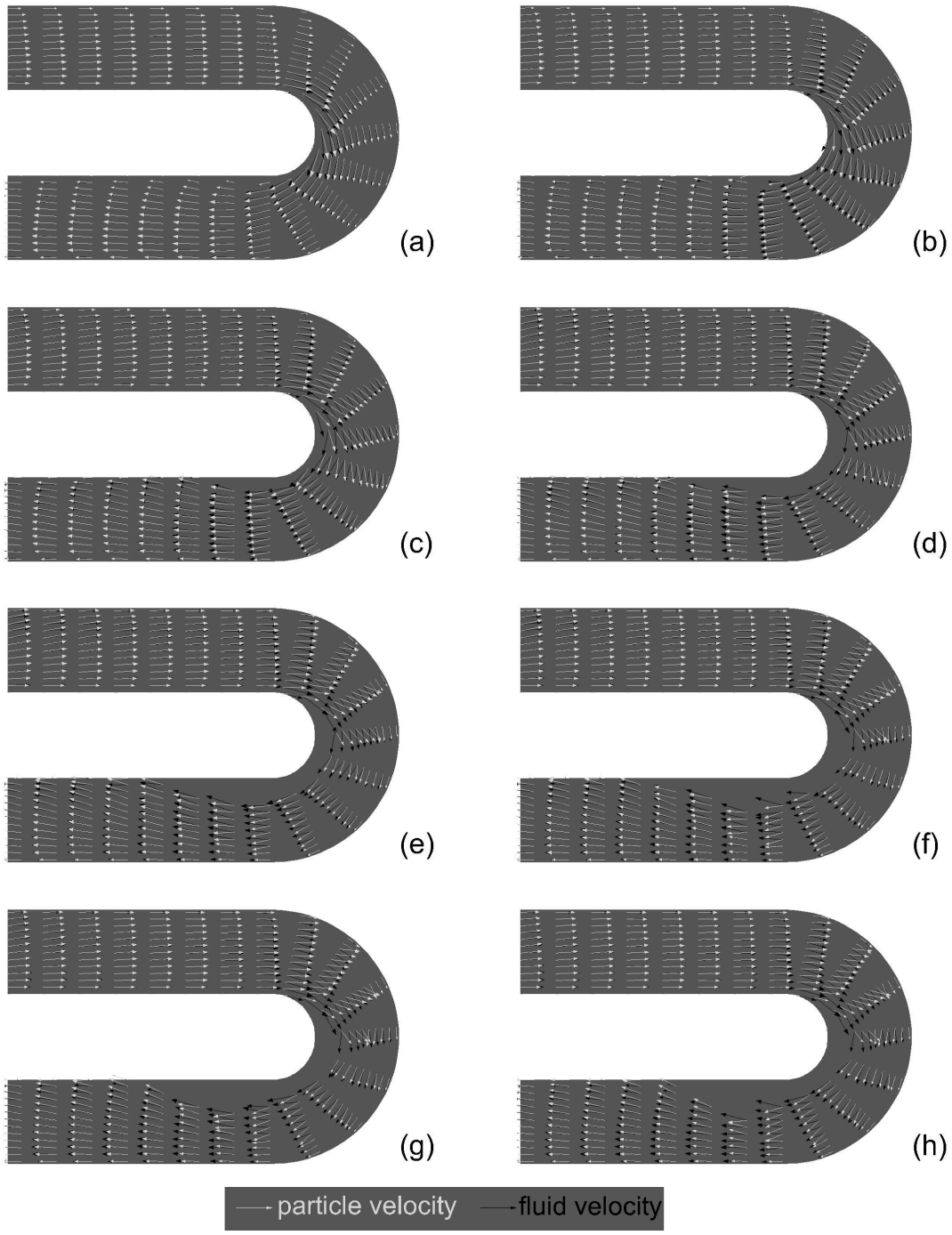

Figure 4.14 Particle and fluid mean velocity vectors in the DNS turbulent flow inside the U-shaped channel. $St_b = 0.125, 0.5, 1, 2, 3, 4, 5, 6$ (plots a-h)

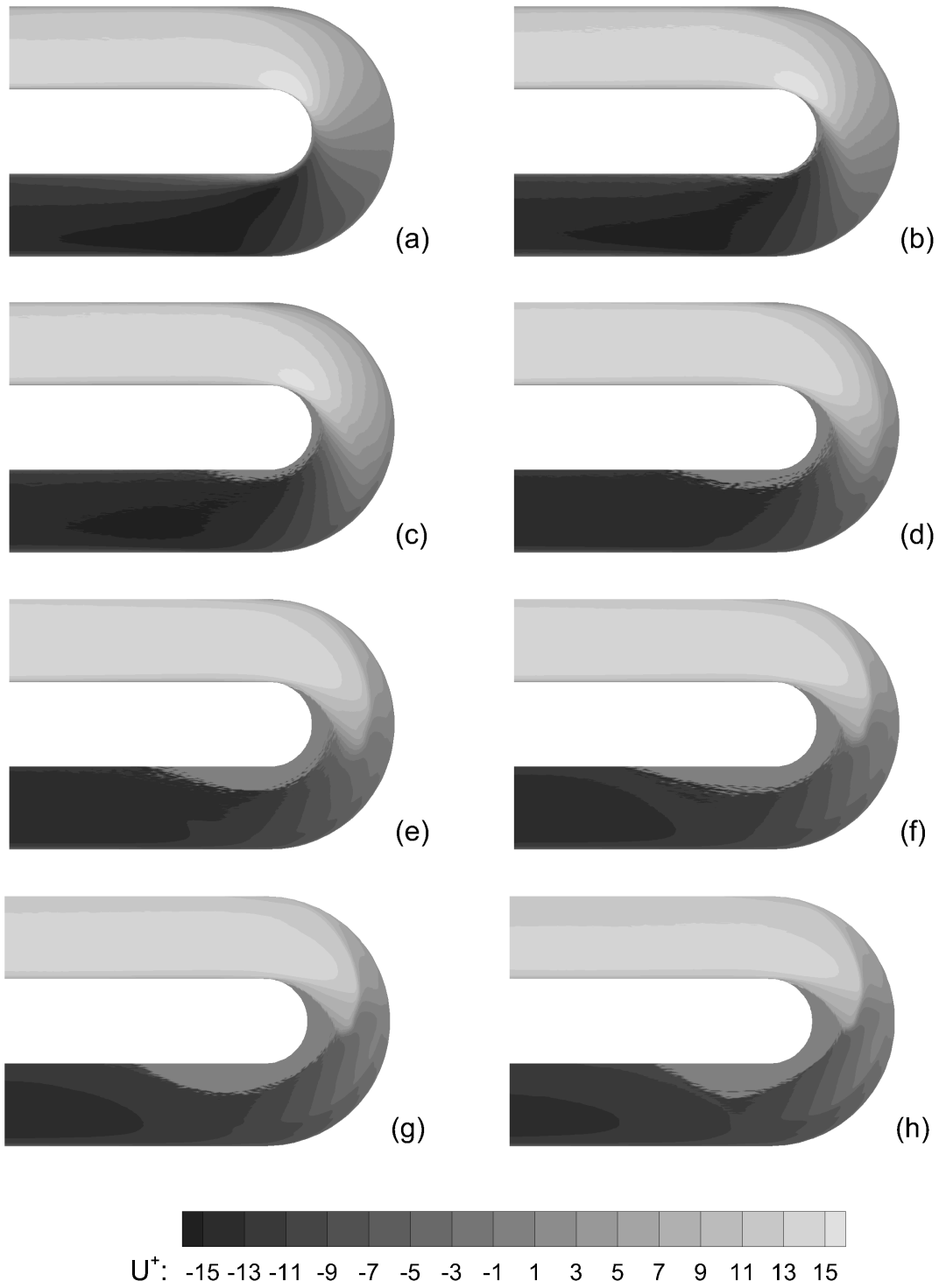

Figure 4.15 Particle mean velocity component U^+ contour in the DNS turbulent flow inside the U-shaped channel. $St_b = 0.125, 0.5, 1, 2, 3, 4, 5, 6$ (plots a-h)

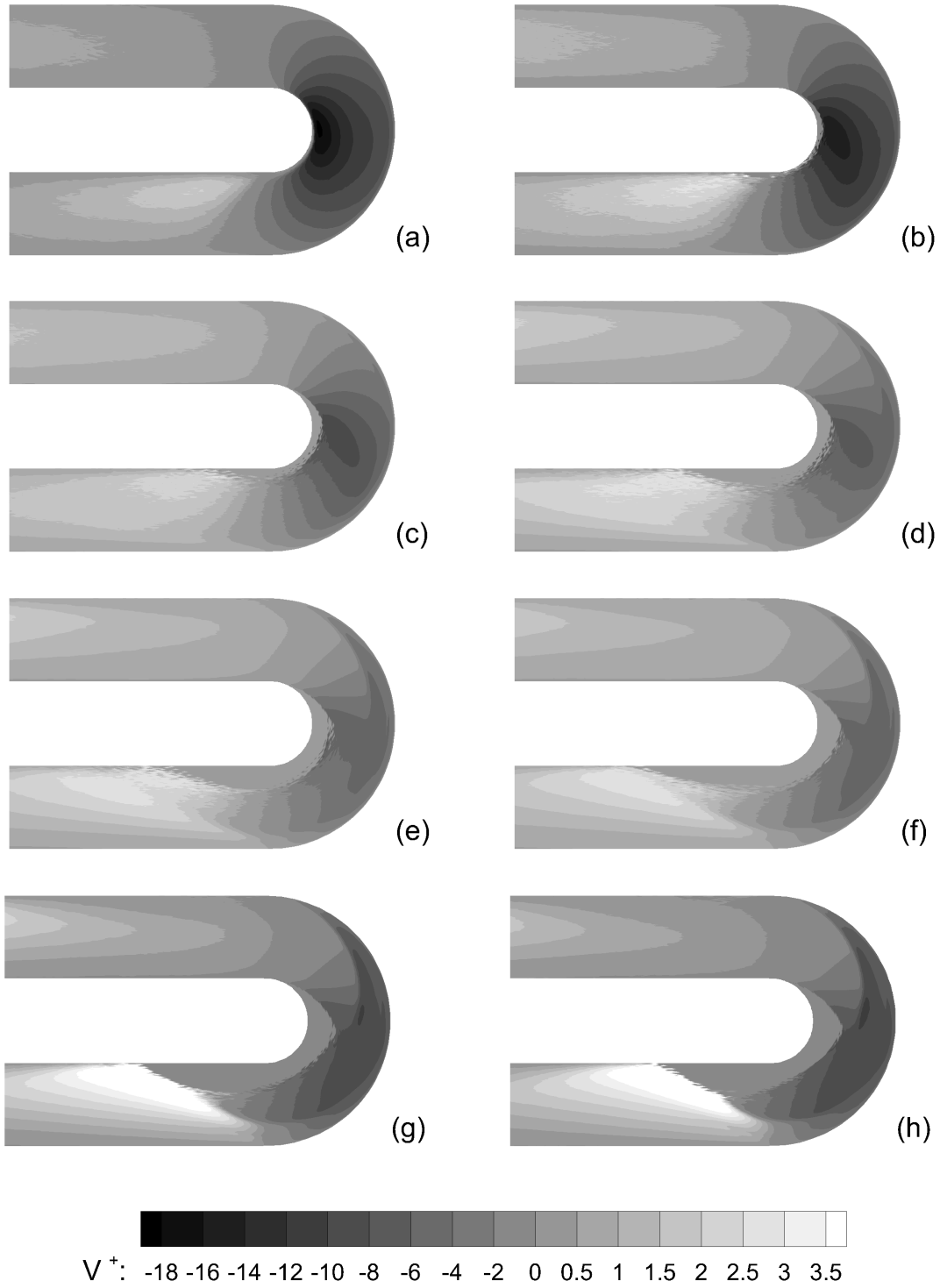

Figure 4.16 Particle mean velocity component V^+ contour in the DNS turbulent flow inside the U-shaped channel. $St_b = 0.125, 0.5, 1, 2, 3, 4, 5, 6$ (plots a-h)

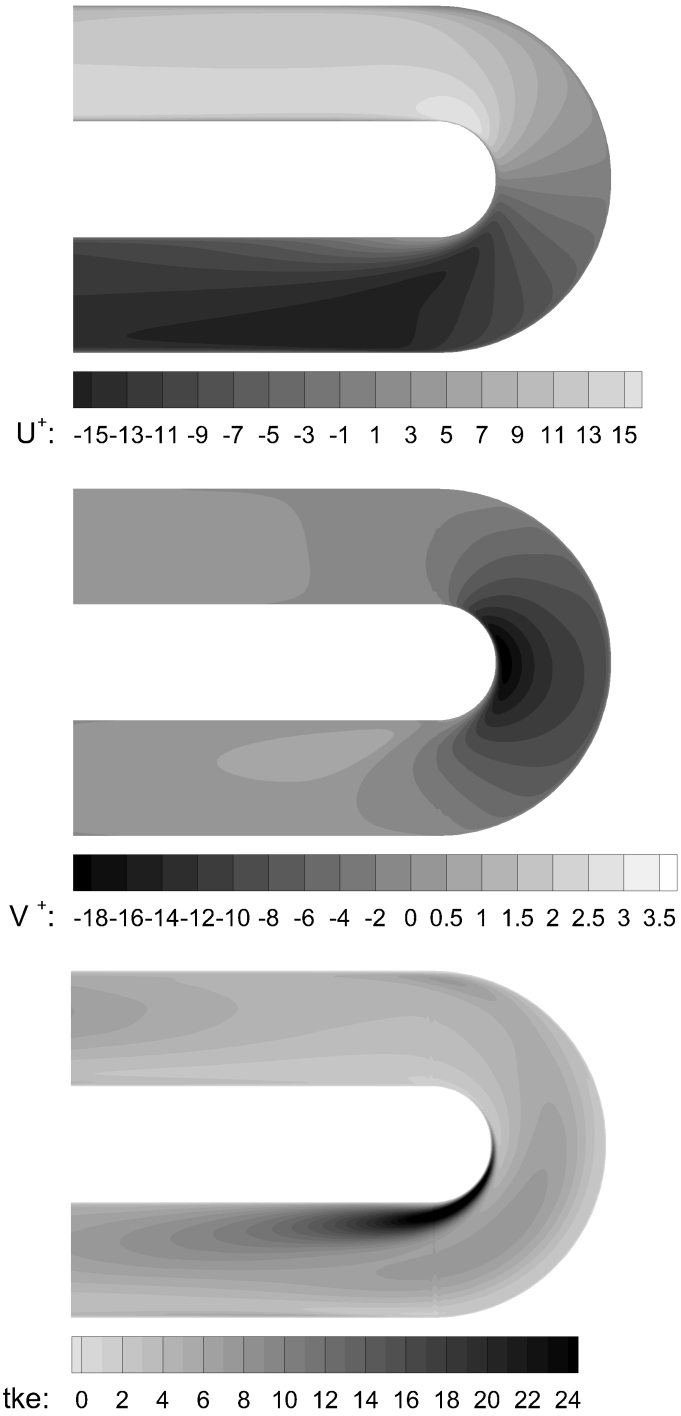

Figure 4.17 Contours of fluid mean velocity components (U^+, V^+) and fluid phase turbulent kinetic energy (tke) in the DNS turbulent flow inside the U-shaped channel.

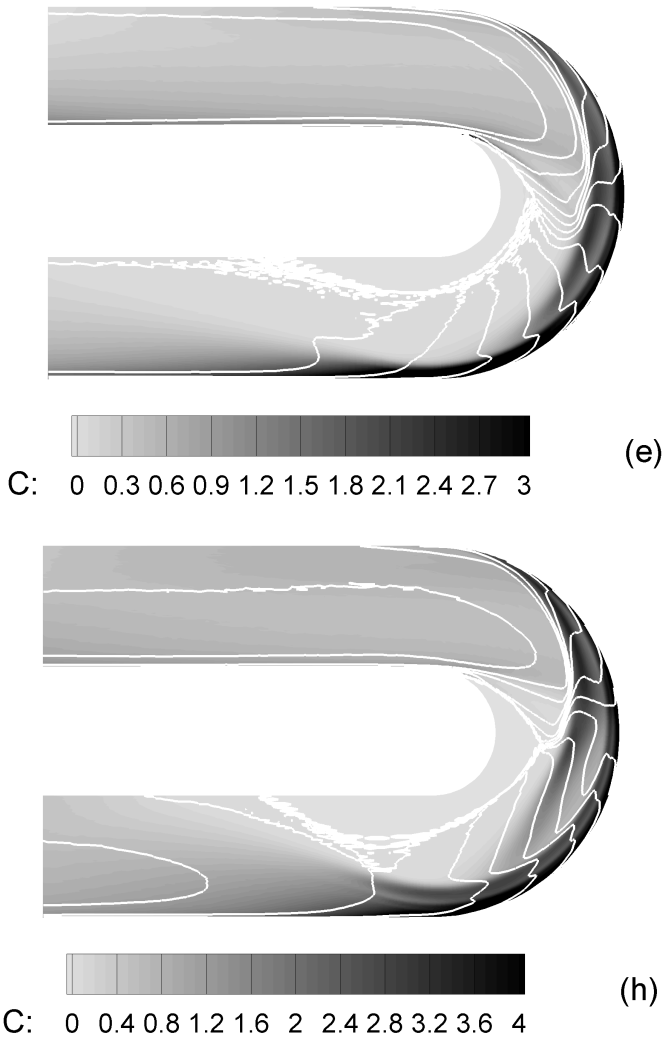

Figure 4.18 Contour lines of particle streamwise velocity component U^+ superimposed on the flooded contour of particle concentration in the DNS turbulent flow inside the U-shaped channel. $St_b = 3, 6$ (plots e,h)

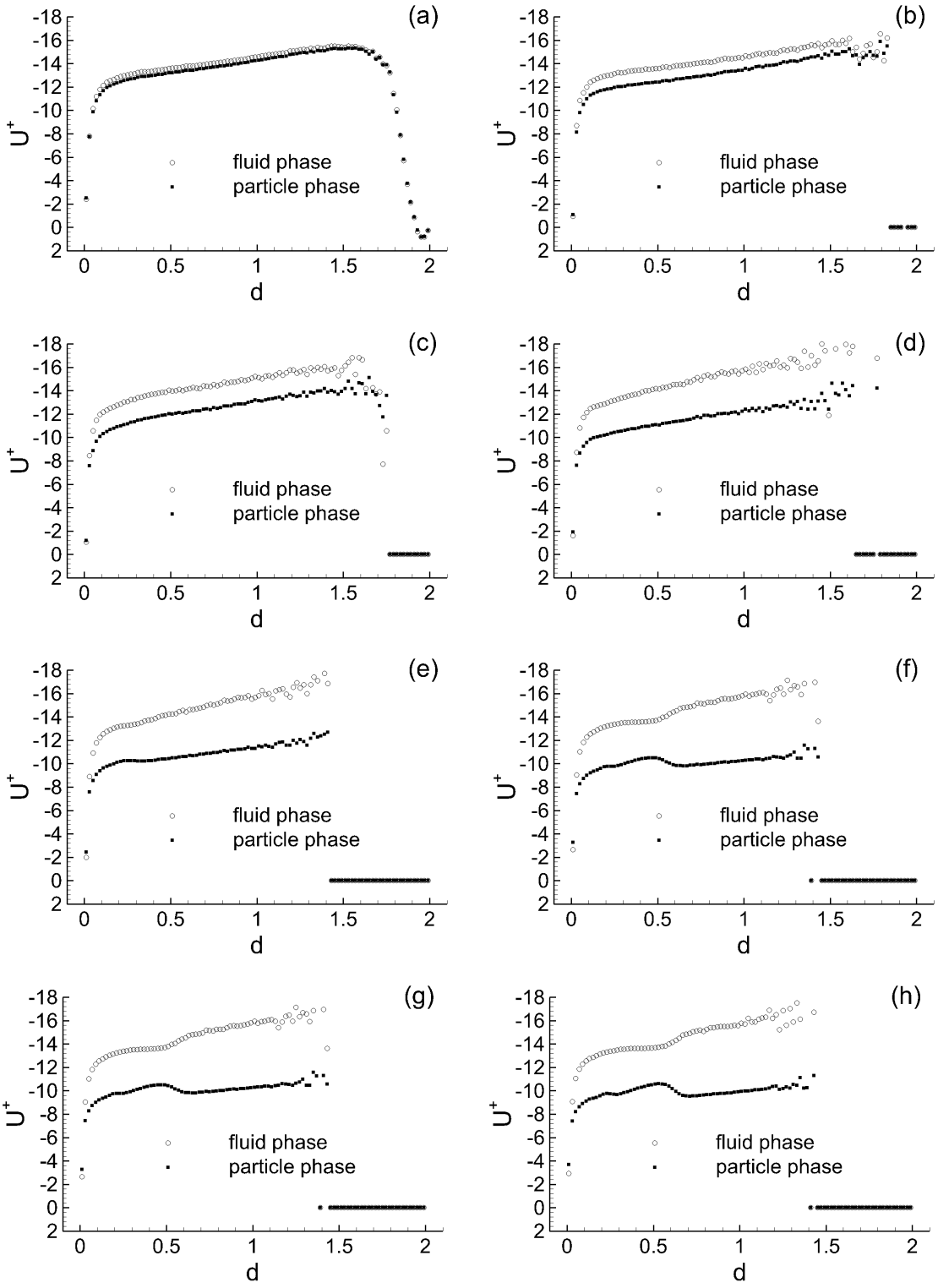

Figure 4.19 Particle mean streamwise velocity profiles at the exit of the curved section in the DNS turbulent flow inside the U-shaped channel. $St_b = 0.125, 0.5, 1, 2, 3, 4, 5, 6$ (plots a-h)

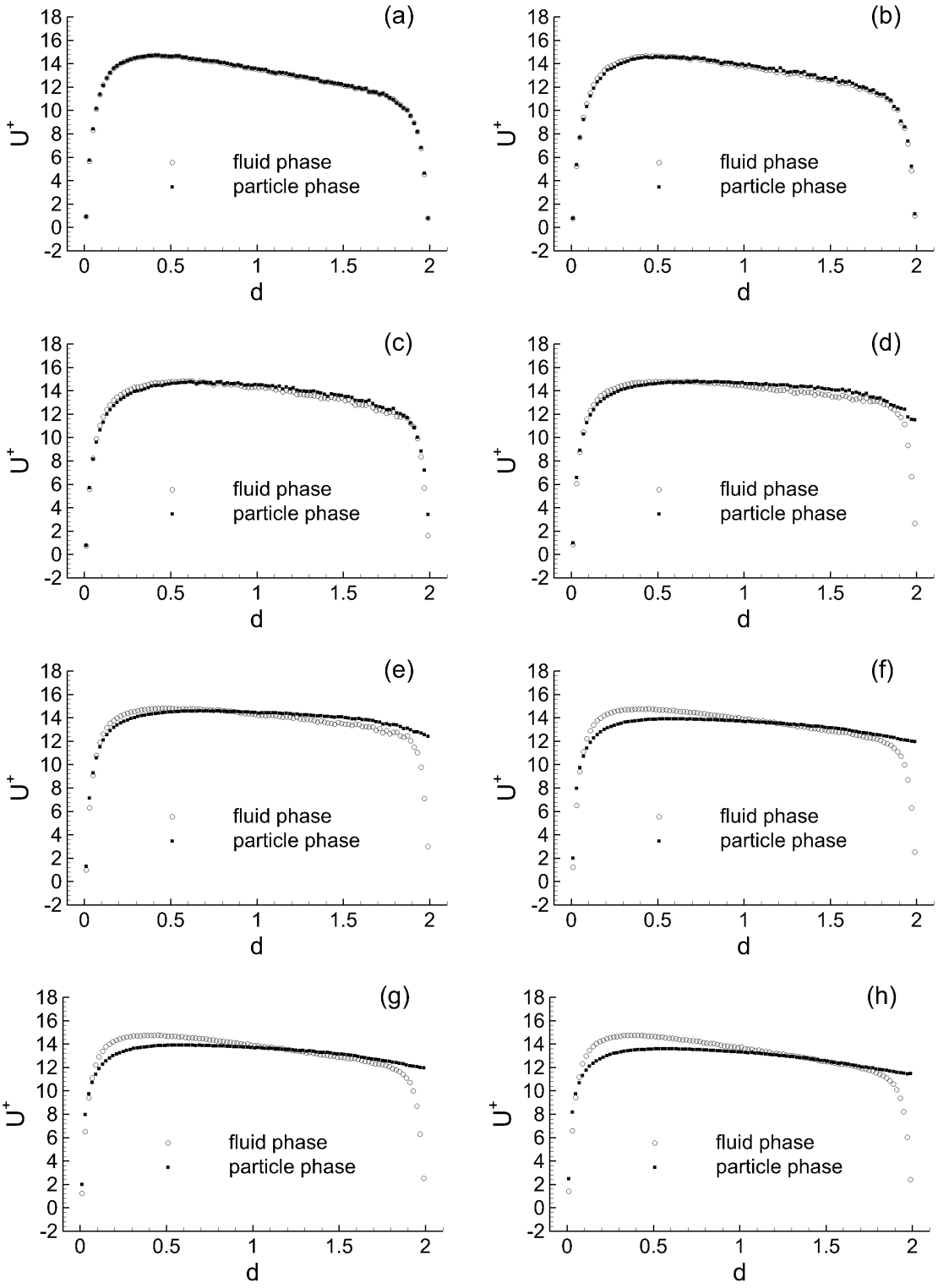

Figure 4.20 Particle mean streamwise velocity profiles at the entrance in the DNS turbulent flow inside the U-shaped channel. $St_b = 0.125, 0.5, 1, 2, 3, 4, 5, 6$ (plots a-h)

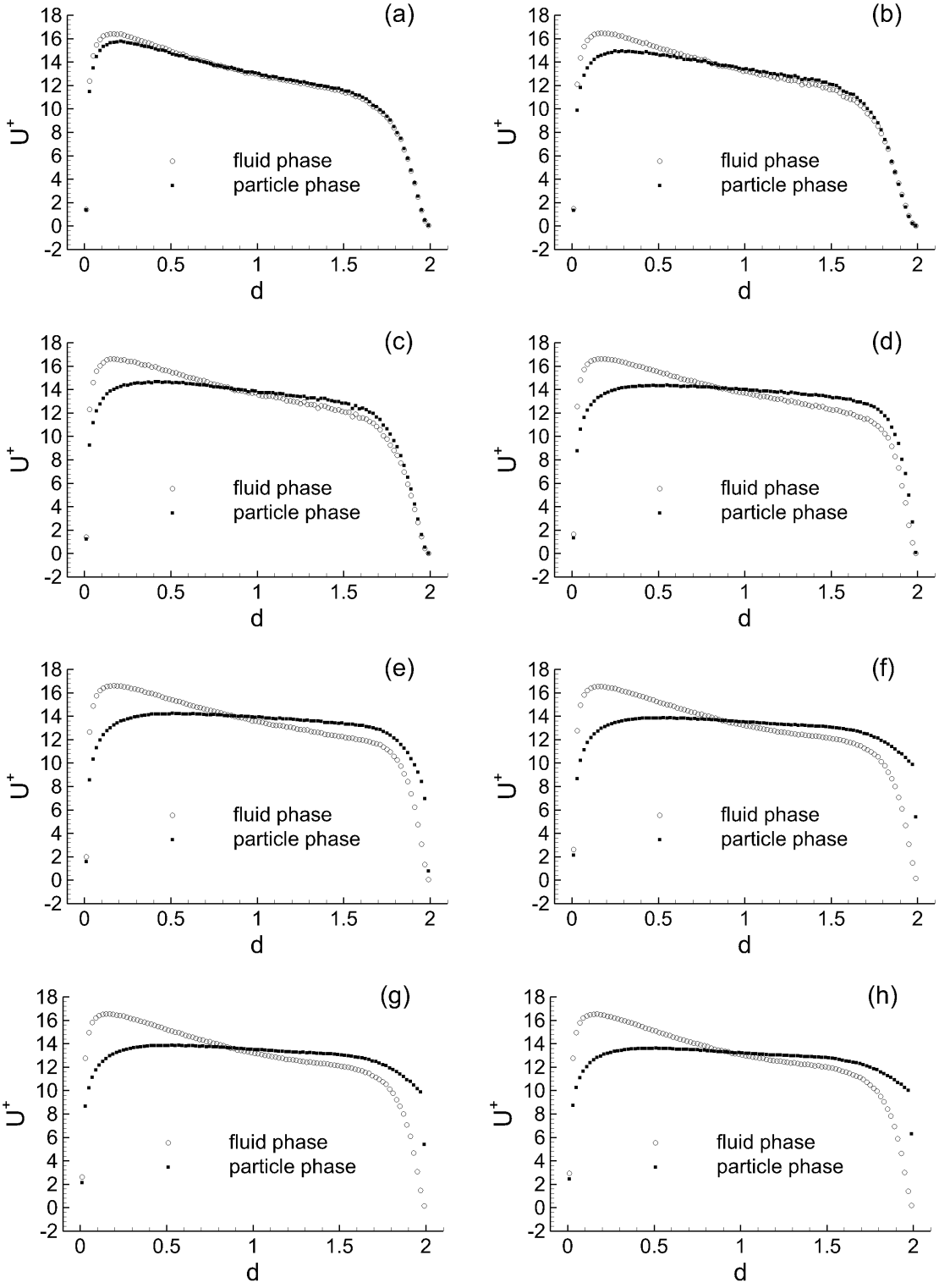

Figure 4.21 Particle mean streamwise velocity profiles at the entrance of the curved section in the DNS turbulent flow inside the U-shaped channel. $St_b = 0.125, 0.5, 1, 2, 3, 4, 5, 6$ (plots a-h)

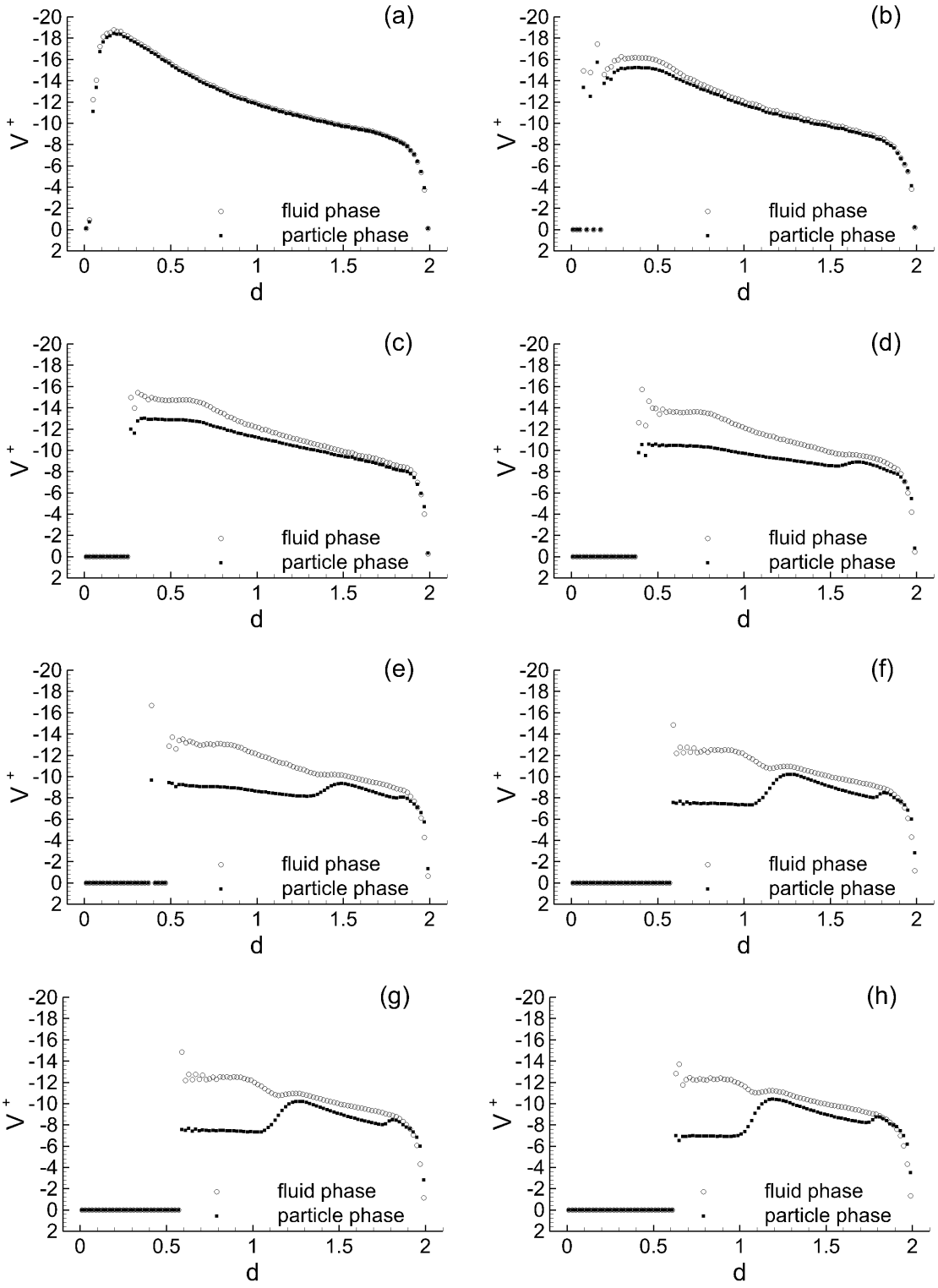

Figure 4.22 Particle mean streamwise velocity profiles at the middle position of the curved section in the DNS turbulent flow inside the U-shaped channel. $St_b = 0.125, 0.5, 1, 2, 3, 4, 5, 6$ (plots a-h)

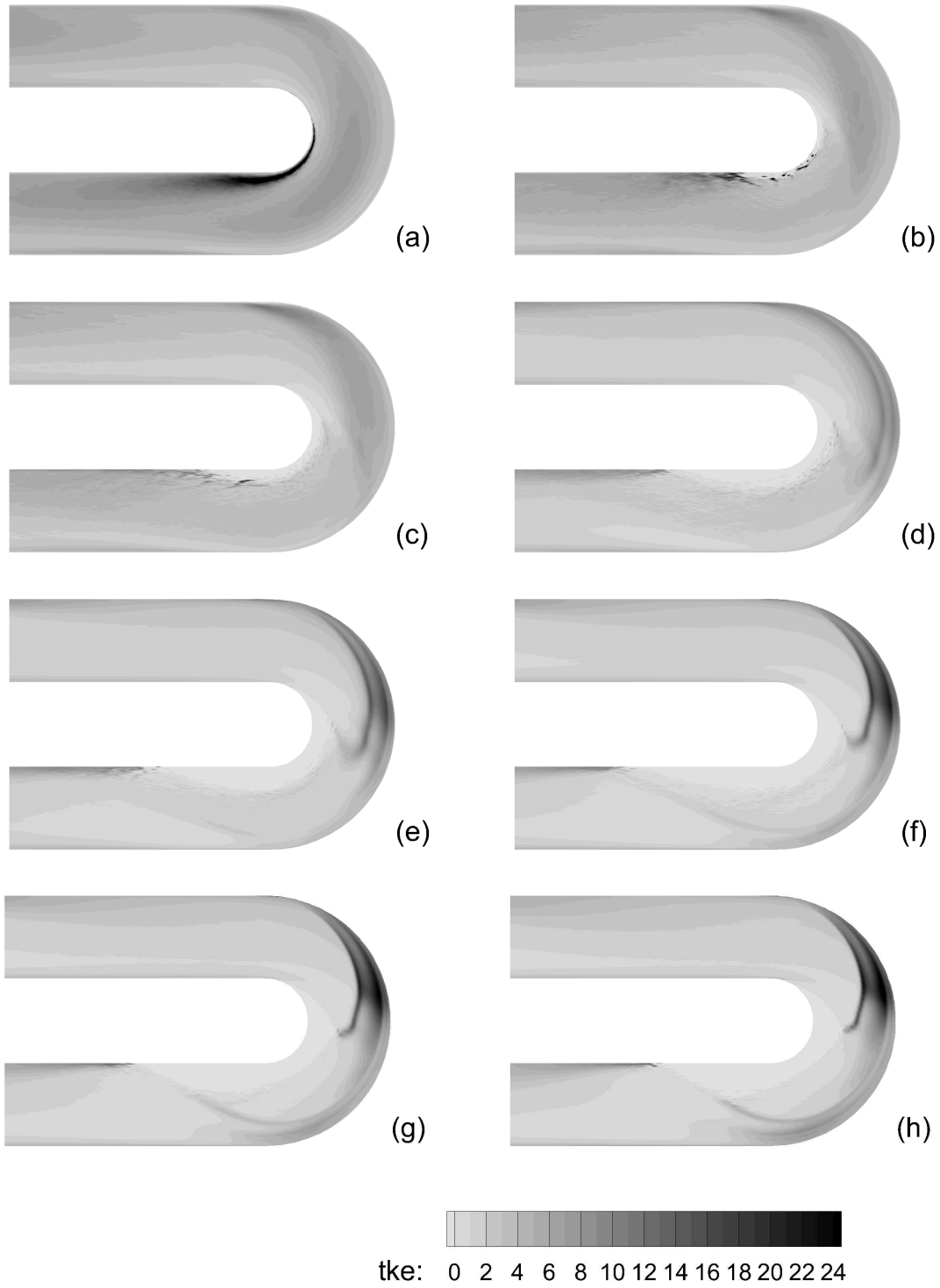

Figure 4.23 Particle phase turbulent kinetic energy (tke) contour in the DNS turbulent flow inside the U-shaped channel. $St_b = 0.125, 0.5, 1, 2, 3, 4, 5, 6$ (plots a-h)

4.5 Particle-Wall Collision Modeling

In the simulation presented in the previous sections, the type of particle-wall collision is elastic reflection and the coefficients of restitution are 1.0 when particles rebound from channel walls. At $St_b \geq 2.0$, the influence of particle-wall collision is observed not only in the curved section but also in the straight section. However, at $St_b \leq 1.0$, the influence of particle-wall collision is hard to determine, though the collision may affect the accumulation of particles on channel walls. To further examine the effect of particle-wall collision on particle distribution, a simulation assuming inelastic reflection was carried out, in which the restitution coefficients were dependent of particle impingement angle α. The adopted correlation between the restitution coefficients and particle impingement angle is an experimental formula from Forder *et al.* (1998):

$$e_n = 0.988 - 0.78\alpha + 0.19\alpha^2 - 0.024\alpha^3 + 0.027\alpha^4 \tag{4.1}$$

$$e_t = 1 - 0.78\alpha + 0.84\alpha^2 - 0.21\alpha^3 + 0.028\alpha^4 - 0.022\alpha^5 \tag{4.2}$$

where e_n and e_t are the restitution coefficients in the direction perpendicular and parallel to the wall, respectively. At any non-zero impingement angle, the restitution coefficients are smaller than 1.0, thus inelastic reflection cannot repel particles away from channel walls as far as elastic reflection. The influence of particle-wall collision should decrease in the simulation assuming inelastic reflection.

Figure 4.24 presents contour plots of particle mean concentration C/C_0 when the particle-wall collision is inelastic reflection, and the profiles of $log(C/C_0+1)$ are displayed in Figure 4.25. The corresponding figures showing elastic reflection are Figures 4.6 and 4.7. For $St_b \geq 2.0$, comparing plots d-h in Figure 4.24 with those in Figure 4.6 reveals that the high concentration region adjacent to the outer bend is narrower when the reflection is inelastic. In the straight section, particle concentration in the core region and near the upper wall is smaller. Consequently, at the entrance of the curved section, fewer particles are thrown onto the beginning part of the outer bend. When plots d-h in Figure 4.25 are compared with those in Figure 4.7, the concentration adjacent to the beginning part of the outer bend is smaller. Other than

in this region, the concentration of the near-wall accumulation is larger when the intensity of collisions is reduced.

For $St_b \leq 1.0$, the difference in the concentration between elastic and inelastic reflection is barely discernible by comparing plots a-c in Figures 4.24 and 4.6 or plots a-c in Figures 4.25 and 4.7. For a more precise comparison between elastic and inelastic reflection, Figures 4.26-4.31 present, respectively, the concentration profiles of $St_b = 0.125$, 0.5, 1.0, 2.0, 4.0, and 6.0 along SURFACE-1 in the S-shaped channel shown in Figure 4.32. In Figures 4.26-4.31, the horizontal axis represents the distance along the center line of the S-shaped channel, instead of SURFACE-1. The profiles of $0.0 \leq S/\pi \leq 6.0$ and $6.0 \leq S/\pi \leq 12.0$ delineate the concentration along the inner and outer walls of the U-shaped channel. As discussed in section 4.4, a fine mesh is required for the statistics in the near-wall region. To post-process particle concentration on SURFACE-1, the mesh size in the wall-normal direction is refined to 1.1 in wall unit.

At $St_b \leq 1.0$ (Figures 4.26-4.28), the concentration profiles differ slightly when the reflection is modified from elastic to inelastic, but the difference is negligible. The difference caused by the type of reflection becomes larger as St_b increases from 2.0 to 6.0 (Figures 4.29-4.31). Thus, for $St_b \geq 2.0$, the modeling of particle-wall collision would be critical and worth further investigation. For $St_b \leq 1.0$, the influence of particle-wall collision on particle concentration is not significant, and the cause of particle accumulation on channel walls will be discussed in the next section.

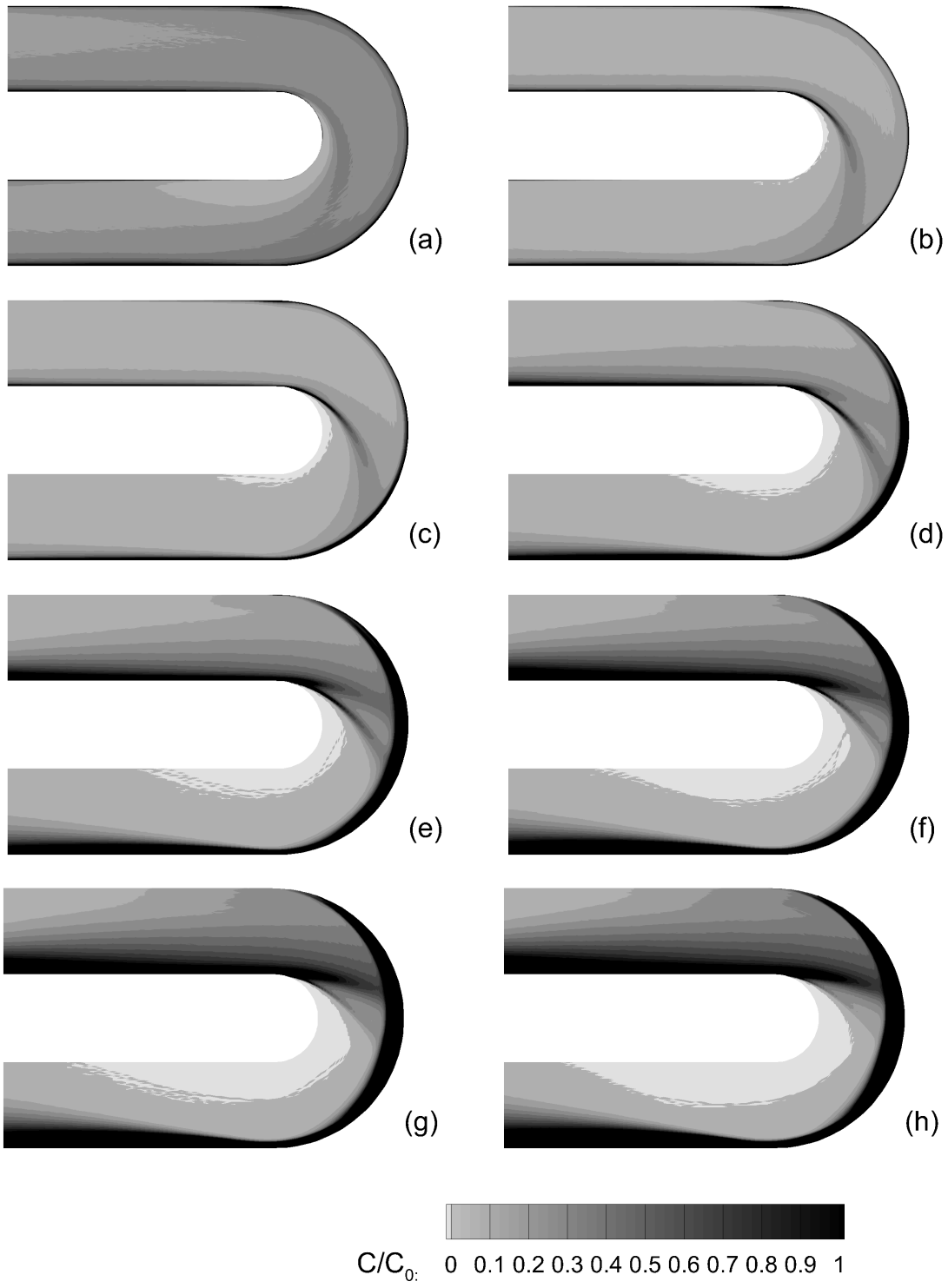

Figure 4.24 Contours of particle mean concentration in the U-shaped channel with inelastic reflection. $St_b = 0.125, 0.5, 1, 2, 3, 4, 5, 6$ (plots a-h)

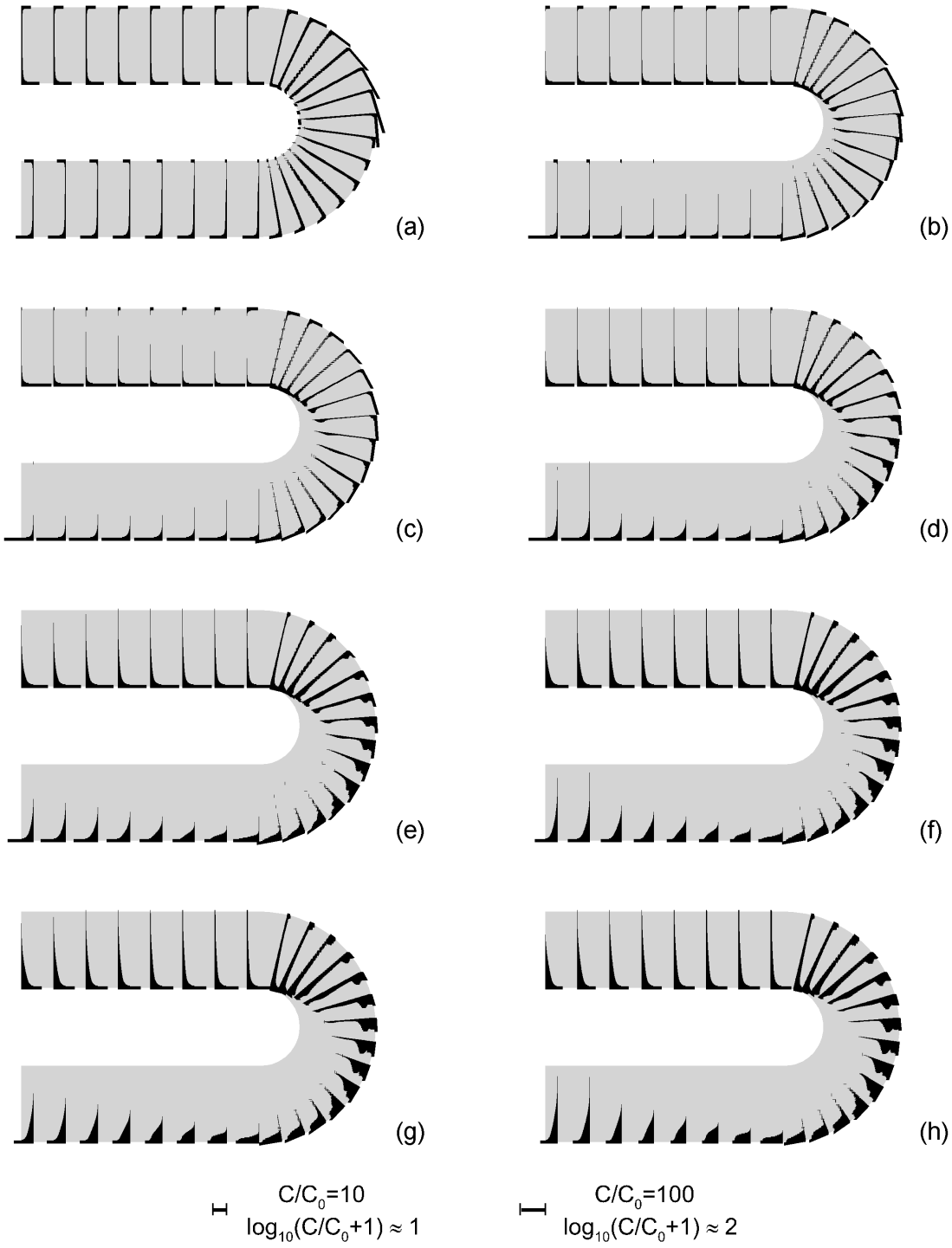

Figure 4.25 Particle mean concentration profiles in logarithm in the U-shaped channel with inelastic reflection. $St_b = 0.125, 0.5, 1, 2, 3, 4, 5, 6$ (plots a-h)

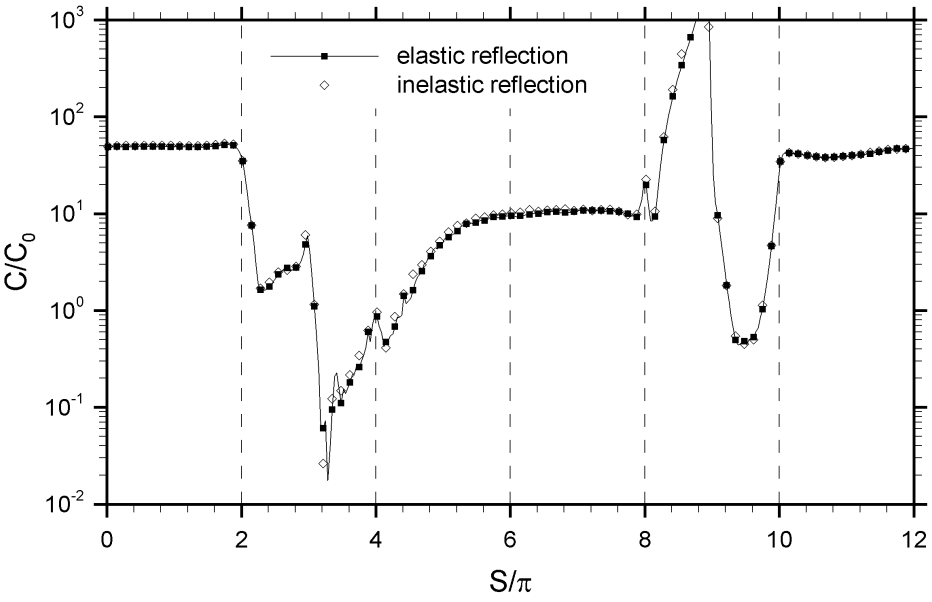

Figure 4.26 Particle concentration on SURFACE-1 with elastic and inelastic reflection at $St_b = 0.125$.

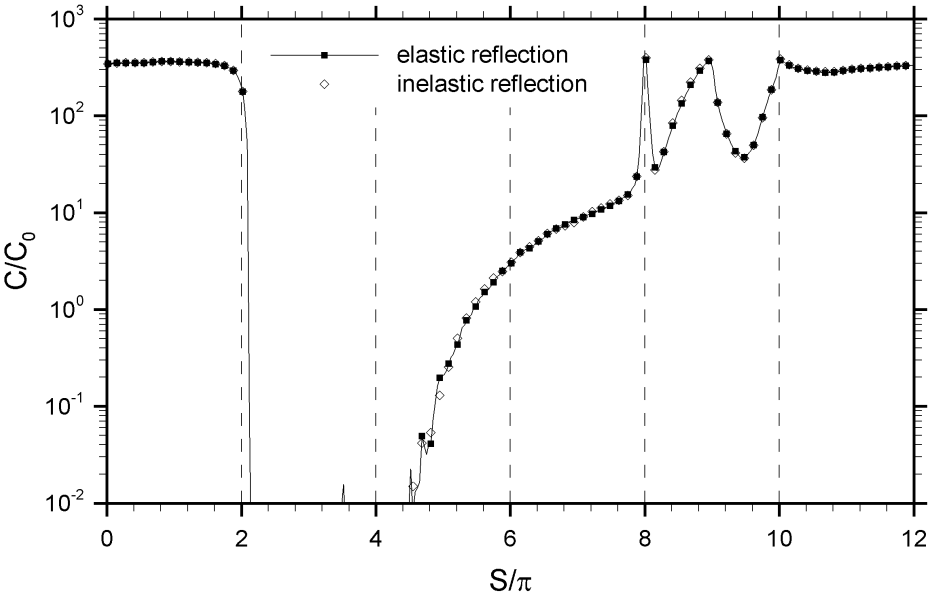

Figure 4.27 Particle concentration on SURFACE-1 with elastic and inelastic reflection at $St_b = 0.5$.

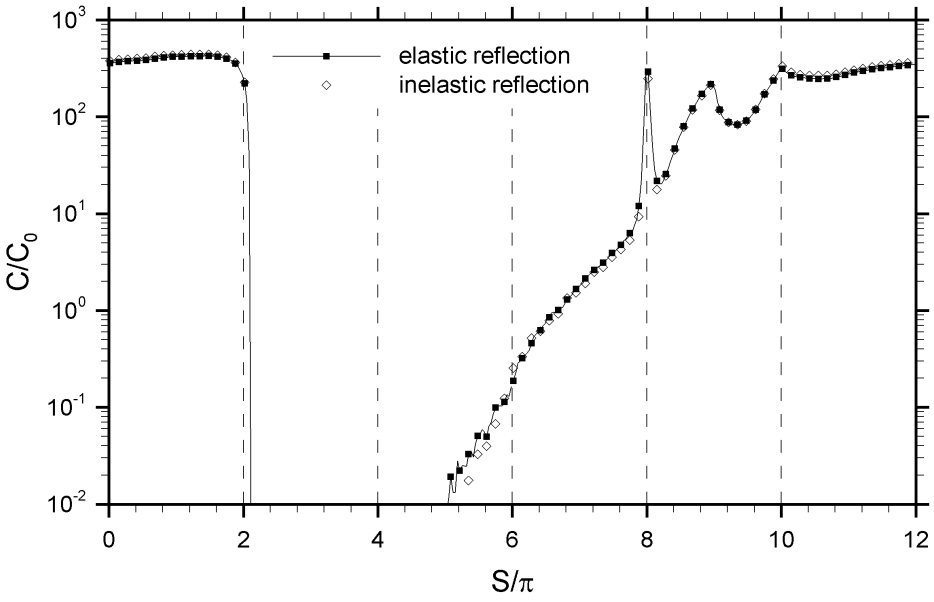

Figure 4.28 Particle concentration on SURFACE-1 with elastic and inelastic reflection at $St_b = 1$.

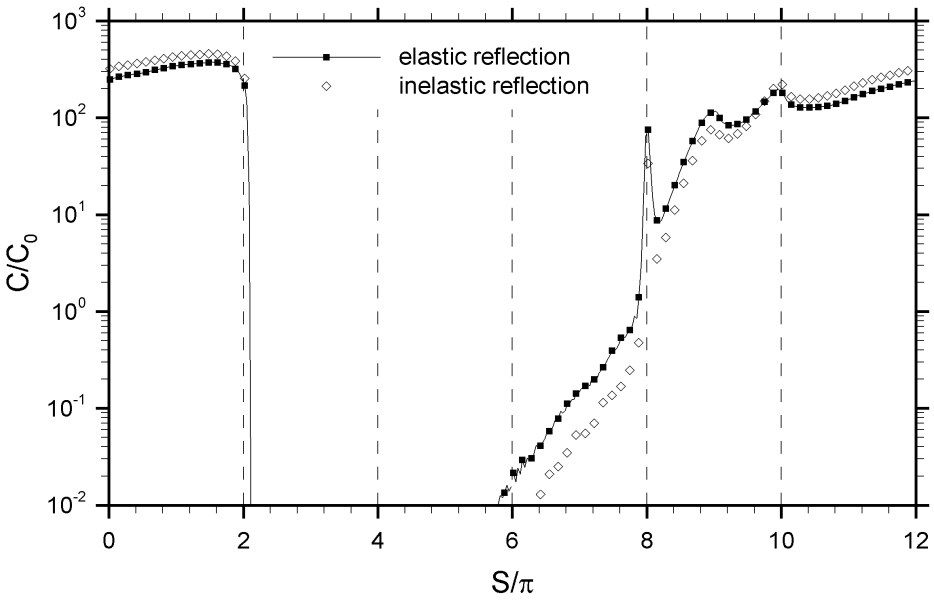

Figure 4.29 Particle concentration on SURFACE-1 with elastic and inelastic reflection at $St_b = 2$.

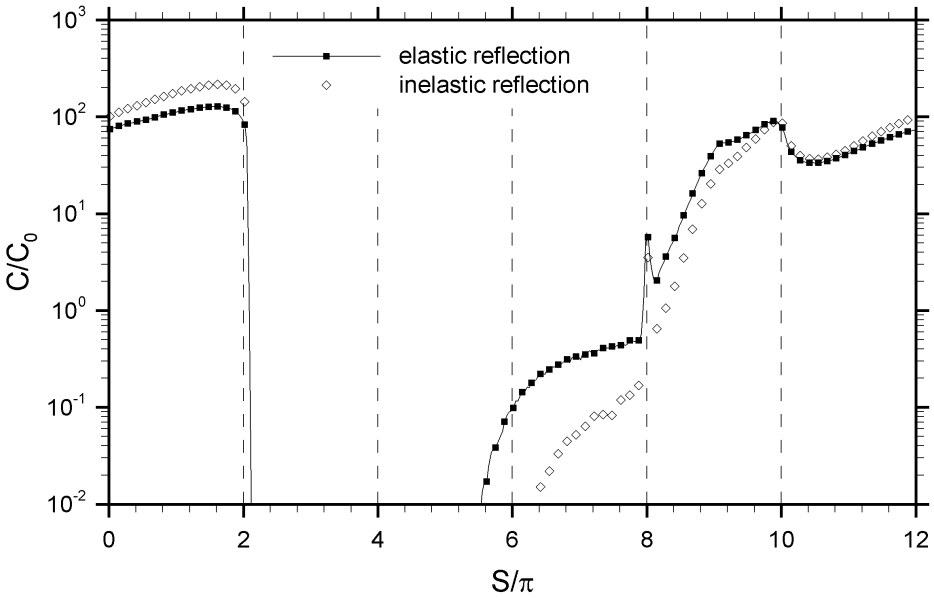

Figure 4.30 Particle concentration on SURFACE-1 with elastic and inelastic reflection at $St_b = 4$.

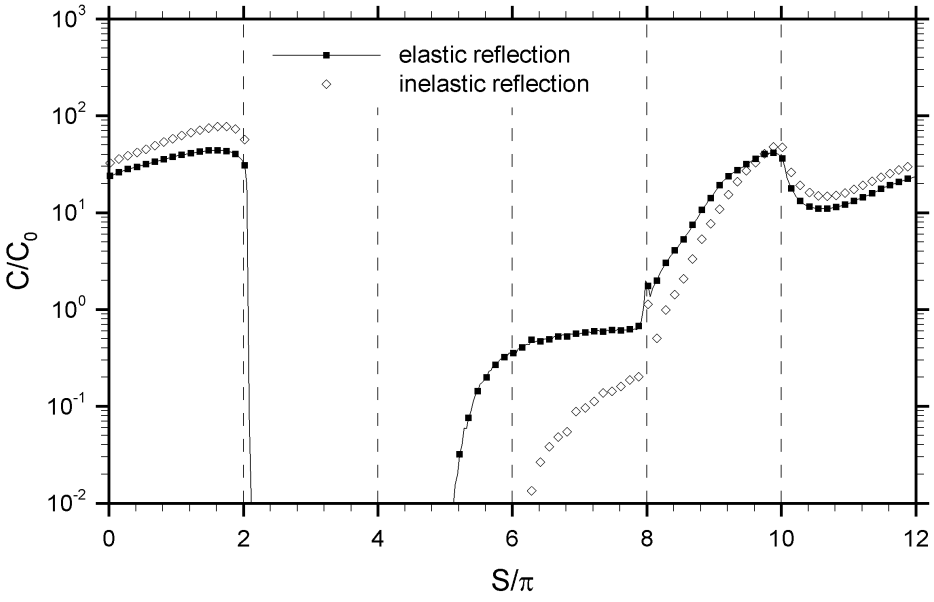

Figure 4.31 Particle concentration on SURFACE-1 with elastic and inelastic reflection at $St_b = 6$.

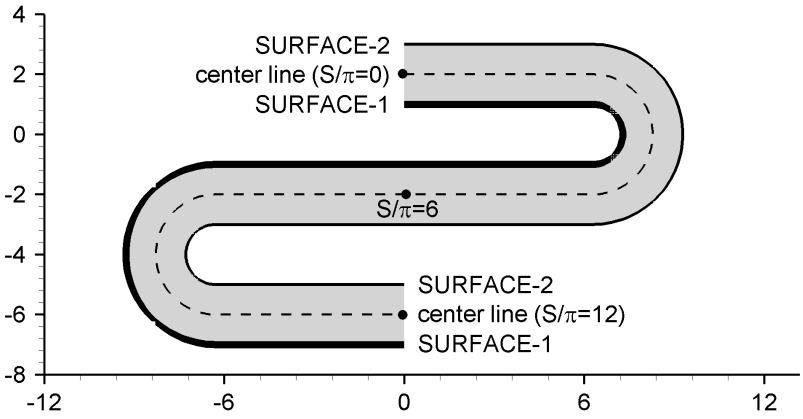

Figure 4.32 SURFACE-1 in the S-shaped channel.

4.6 Particle Accumulation adjacent to Channel Walls

To explore the cause of particle accumulation adjacent to the channel walls for $St_b \leq 1.0$, the location to start is the inner bend, the concentration along which is represented by the range $2.0 \leq S/\pi \leq 4.0$ in Figures 4.26-4.28. At $St_b = 0.125$ (Figure 4.26), particle concentration decreases rapidly around $S/\pi = 2.0$ where particles are thrown away from the inner bend by centrifugal acceleration. Along the inner bend, particles become slower and centrifugal acceleration diminishes. When the centrifugal acceleration becomes trivial, the concentration starts increasing. As particles approach the middle point ($S/\pi = 3.0$), they cannot follow the fluid around the bend and leaves the wall, which causes the concentration to plunge. On the lower part of the inner bend ($3.0 \leq S/\pi \leq 4.0$), particles are either transported from the straight section by the reverse flow or scattered from the core region by turbulence. In general, at $St_b = 0.125$, particle concentration on the inner bend is affected by fluid convection and centrifugal acceleration. As St_b increases to 0.5 and 1.0 (Figures 4.27 and 4.28), the inertia carries all particles away from the inner bend at the entrance of the curved section, and the concentration profiles of both plunge to zero immediately after $S/\pi = 2.0$.

After particles are thrown away from the inner bend by centrifugal acceleration in the curved section, they are transported from the core region to the upper wall in the straight section by the flow. In the core region of the straight section, the mean velocity component V^+ of the particle phase is larger than the fluid mean V^+, as shown in section 4.4. This is because turbulent diffusion transports more particles toward the upper wall due to the concentration gradient. In the core region after the separation bubble ($S/\pi \approx 4.3$), the particle mean velocity component V^+ is nearly 1.5, 2.0 and 3.0, respectively, at $St = 0.125$, 0.5 and 1.0. As particles move from the core region to the upper wall, they are decelerated by the fluid. By assuming the velocity decreases linearly, particle displacement can be roughly estimated. If the velocity of a particle located at 1/4 channel width below the upper wall is 12 in the streamwise direction ($U^+ = 12$) and 1.5 in the wall-normal direction ($V^+ = 1.5$), this particle advances approximately 3.3 in the streamwise direction ($\Delta S \approx 3.3$) while it traverses 0.5 to reach the upper wall ($\Delta y = 0.5$). Although this estimation can not provide the accurate position where

this particle arrives at the upper wall, it suggests that a considerable number of particles can approach the upper wall before $S/\pi = 6.0$, which corresponds to the exit of the U-shaped channel. In Figures 4.26-4.28, the particle concentration for $St_b \leq 1.0$ rises at least an order of magnitude along $4.0 \leq S/\pi \leq 6.0$.

The accumulation of particles on the entire upper wall ($4.0 \leq S/\pi \leq 8.0$) can be caused by fluid convection plus turbophoresis. As has discussed in the previous chapter, particles are affected by the turbophoretic force F^+_{turbo} from the fluid and acquire the turbophoretic velocity V^+_{turbo} in the wall-normal direction. The turbophoretic velocity ($V^+_{turbo} = St^+ F^+_{turbo}$) is proportional to the turbophoretic force ($F^+_{turbo} = -\partial\overline{v^{+2}}/\partial y^+$). The calculation of particle phase F^+_{turbo} requires smooth profiles of particle phase $\overline{v^{+2}}$ in the wall-normal direction throughout the U-shaped channel. But this would require an excessive number of particles. For that reason, the turbophoretic force F^+_{turbo} of $St_b = 0.125$ is approximated using the fluid phase $-\partial\overline{v^{+2}}/\partial y^+$ from the DNS solver. According to the statistics of particle motion in the plane channel, the maximum F^+_{turbo} of $St_b = 0.125$ is about 0.015 at $\Delta y^+ \approx 20$ from channel walls. It is close to the maximum of fluid phase F^+_{turbo}, which is about 0.017 at $\Delta y^+ \approx 18$. In the U-shaped channel, particles of $St_b = 0.125$ basically follow the fluid in the straight section and the turbulent kinetic energy (tke) contour of $St_b = 0.125$ is nearly identical to the fluid phase tke contour, as shown in section 4.4. Thus, it is appropriate to estimate the turbophoretic velocity V^+_{turbo} of $St_b = 0.125$ using the fluid phase $-\partial\overline{v^{+2}}/\partial y^+$.

The influence of turbophoresis and fluid convection on the near-wall accumulation of particles can be evaluated by comparing particle turbophoretic velocity V^+_{turbo} with the fluid mean convection velocity in the wall-normal direction (V^+_{conv}). Figure 4.33 presents the profiles of fluid phase F^+_{turbo} across the channel width at Stations 4, 1 and 2 in the U-shaped channel, with Stations 4, 1 and 2 representing, respectively, the entrance, the middle point and the exit of the straight section in the S-shaped channel. The horizontal axis y represents the distance from the lower to the upper wall. The profile of fluid phase F^+_{turbo} in the plane channel is also plotted for comparison. At Station 4, the maximum F^+_{turbo} adjacent to the upper wall is about 0.2625, which is 15.1 times the maximum in the plane channel. At Stations 1 and 2, the maximum F^+_{turbo} is approximately 4.4 and 2.4 times the maximum in the plane channel.

Thus, particles in the straight section of the S-shaped channel can obtain a larger turbophoretic velocity V^+_{turbo} than those in the plane channel. For $St_b = 0.125$ ($St^+ = 2.28$), the maximum V^+_{turbo} is estimated to be about 0.60, 0.18 and 0.10, respectively, at Stations 4, 1 and 2. The location where particles acquire the maximum V^+_{turbo} varies between $y = 1.9$ and $y = 2.0$, thus the maximum of V^+_{turbo} is larger than or equal to the magnitude of V^+_{turbo} at $y = 1.9$. Figure 4.34 displays the turbophoretic velocity V^+_{turbo} of $St_b = 0.125$ at $y = 1.9$ ($\Delta y^+ = 23$) and the fluid mean velocity component in the wall-normal direction V^+_{conv} at $y = 1.9$ in the straight section. At the entrance of the straight section where the fluid separates from the upper wall ($4.0 \leq S/\pi \leq 4.3$), the profiles of both V^+_{turbo} and V^+_{conv} incline. At $4.0 \leq S/\pi \leq 4.1$, the fluid mean velocity component V^+_{conv} is negative and particles are convected away from the upper wall, thus the concentration of $St_b = 0.125$ decreases at $4.0 \leq S/\pi \leq 4.1$ in Figure 4.26. After $S/\pi \approx 4.1$ where V^+_{conv} becomes positive, particles are transported to the upper wall by fluid convection plus turbophoresis. After the separation bubble ($S/\pi \approx 4.3$), the magnitude of V^+_{turbo} and V^+_{conv} diminishes, thus the accumulation rate of $St_b = 0.125$ becomes smaller. At $5.0 \leq S/\pi \leq 7.0$, the magnitude of fluid convection V^+_{conv} is nearly zero, and the influence of turbophoresis is dominant. After $S/\pi \approx 7.0$, the fluid deviates from the upper wall and the fluid V^+_{conv} is negative again. Along $7.0 \leq S/\pi \leq 8.0$, the magnitude of V^+_{conv} becomes larger while V^+_{turbo} becomes smaller. When the influence of V^+_{conv} overcomes that of V^+_{conv}, the concentration of $St_b = 0.125$ starts decreasing. Thus, for $St_b = 0.125$, particle concentration on the upper wall is affected by both fluid convection and turbophoresis. As St_b increases to 0.5 and 1.0, the magnitude of turbophoretic velocity V^+_{turbo} becomes much larger, according to the statistics of V^+_{turbo} in the plane channel. In Figures 4.27 and 4.28, the concentration of $St_b = 0.5$ and 1.0 increases along $4.0 \leq S/\pi \leq 8.0$ because of turbophoresis, and the influence of fluid convection may be negligible.

When particles enter the curved section, besides centrifugal acceleration, they can drift toward the outer bend due to turbophoresis. Figure 4.35 displays the profiles of fluid phase turbophoretic force F^+_{turbo} at Stations 2, 3 and 4, with Stations 2, 3 and 4 representing the entrance, the middle point and the exit of the curved section, respectively. The horizontal axis y represents the distance from the inner to the outer bend. The maximum F^+_{turbo} adjacent to

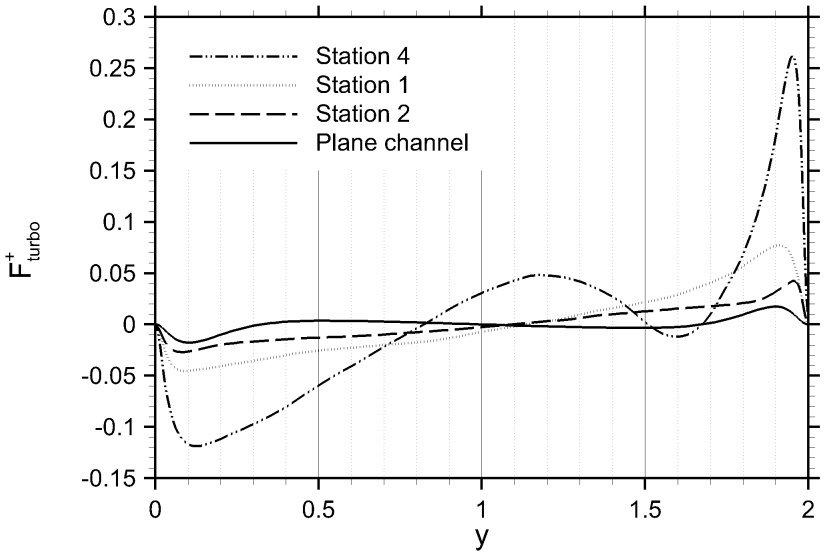

Figure 4.33 Fluid phase turbophoretic force across the channel width in the plane channel and at Stations 4, 1 and 2 in the U-shaped channel. y represents distance from lower wall, with 0 being lower wall and 2 being upper wall.

the outer bend at Stations 2, 3, and 4 is, respectively, 2.4, 4.3 and 6.8 times the maximum in the plane channel. Table 4.1 lists the magnitude of the maximum F^+_{turbo} and the corresponding centrifugal acceleration F^+_{ac} at the location of the maximum F^+_{turbo}. At Station 2, the maximum F^+_{turbo} occurs at $y = 1.95$, where F^+_{turbo} is about 5 times F^+_{ac}. However, at Stations 3 and 4, the maximum of F^+_{turbo} becomes smaller than F^+_{ac}. Thus, turbophoresis may play an important role on particle motion toward the outer wall at the entrance of the curved section, but the centrifugal acceleration becomes more important along the outer bend.

After particles are thrown onto the outer bend by centrifugal acceleration and turbophoresis, their accumulation on the outer bend is affected by fluid convection. The profile of the fluid mean streamwise velocity U^+ at $\Delta y = 0.002$ ($\Delta y^+ = 0.47$) away from SURFACE-1 is displayed in Figure 4.36. At $8.0 \leq S/\pi \leq 8.125$, the fluid mean streamwise velocity U^+ is negative and the flow reverses. Particles are convected to $S/\pi \approx 8.0$ by the fluid from both directions, thus the concentration at $S/\pi \approx 8.0$ becomes much larger in Figures 4.26-4.28. After the reverse flow region, the fluid convects particles forward along the outer bend. At the same time, more particles are thrown onto the outer bend, thus the concentration increases after $S/\pi \approx 8.125$. However, after $S/\pi \approx 9.0$, particles become much faster and the concentration starts decreas-

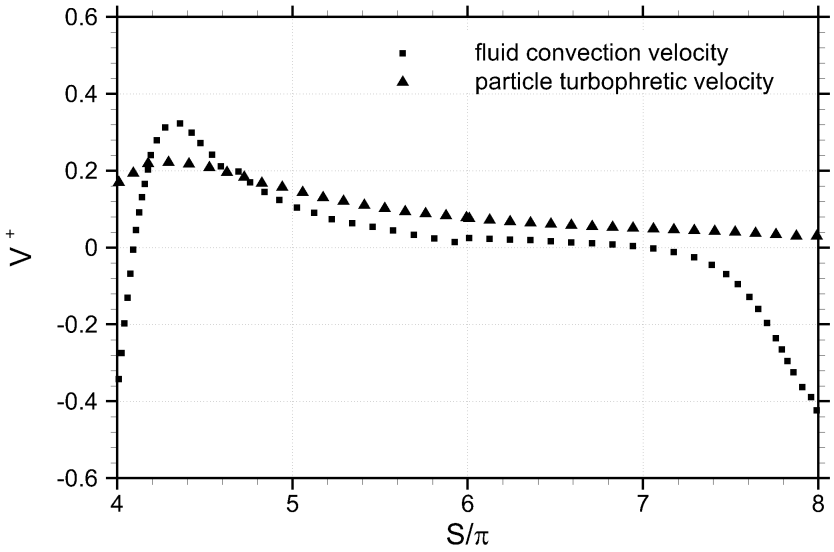

Figure 4.34 Turbophoretic velocity of $St_b = 0.125$ and the fluid mean convection velocity in the wall-normal direction at $\Delta y^+ = 23$ away from the upper wall in the straight section of the S-shaped channel, with $S/\pi = 4.0$ being the entrance and $S/\pi = 6.0$ being the exit.

ing. Due to the approximation error in the simulation, particle velocity is underestimated when particles cross the outer bend at the intermediate time steps of the Runge-Kutta interpolation, and particle concentration on the upper part of the outer bend ($8.125 \leq S/\pi \leq 9.0$) is over-estimated. In Figures 4.26-4.28, the concentration is plotted in the range of $10^{-2} \sim 10^{3}$ since the variation of particle concentration along channel walls is more interesting than the exact magnitude of the concentration at a particular location.

On the lower part of the outer bend ($9.0 \leq S/\pi \leq 10.0$), particle concentration becomes larger when more particles from the plume are thrown onto the outer bend. After $S/\pi = 10.0$ where the outer wall becomes the lower wall in the straight section, particle concentration diminishes as the influence of centrifugal acceleration attenuates. In Figures 4.26-4.28, the concentration on the first half and the second half of the lower wall is delineated, respectively, by profiles of $10.0 \leq S/\pi \leq 12.0$ and $0.0 \leq S/\pi \leq 2.0$. Away from the entrance of the straight section, the concentration on the lower wall increases slowly due to turbophoresis. As the accumulated particles approach the exit of the straight section ($S/\pi = 2.0$), they are thrown away from the inner wall by centrifugal acceleration and the concentration on the lower wall

diminishes.

In summary, for $St_b \leq 1.0$ in the U-shaped channel, particles are transported to channel walls by fluid diffusion and turbophoresis, plus the fluid mean convection in the straight section and centrifugal acceleration in the curved section. Particle concentration on channel walls is also affected by the streamwise mean velocity of the fluid near the channel walls.

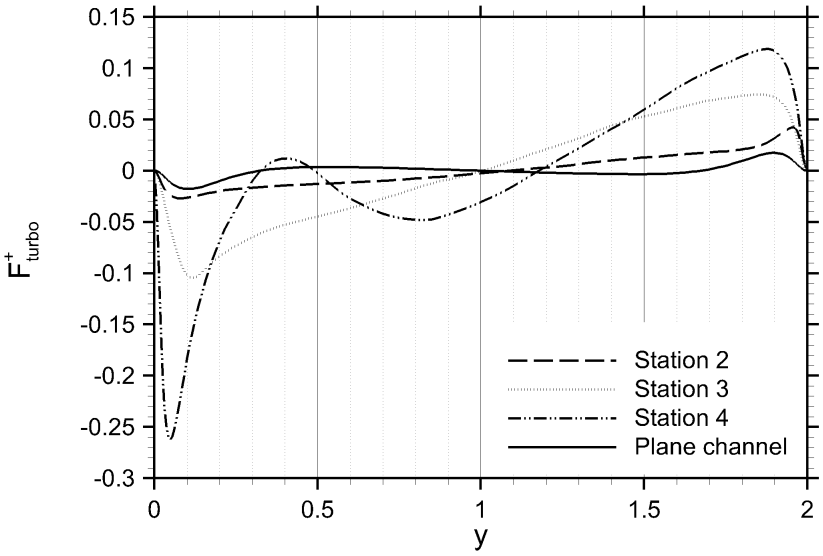

Figure 4.35 Fluid phase turbophoretic force across the channel width in the plane channel and at Stations 2, 3 and 4 in the U-shaped channel. y represents distance from inner wall, with 0 being inner wall and 2 being outer wall

Table 4.1 The maximum fluid phase turbophoretic force and the corresponding centrifugal acceleration at Stations 2, 3 and 4.

Station	F^+_{turbo}	y	U^+	F^+_{ac}
2	0.042	1.96	2.0	0.009
3	0.074	1.85	8.5	0.172
4	0.119	1.87	13.2	0.411

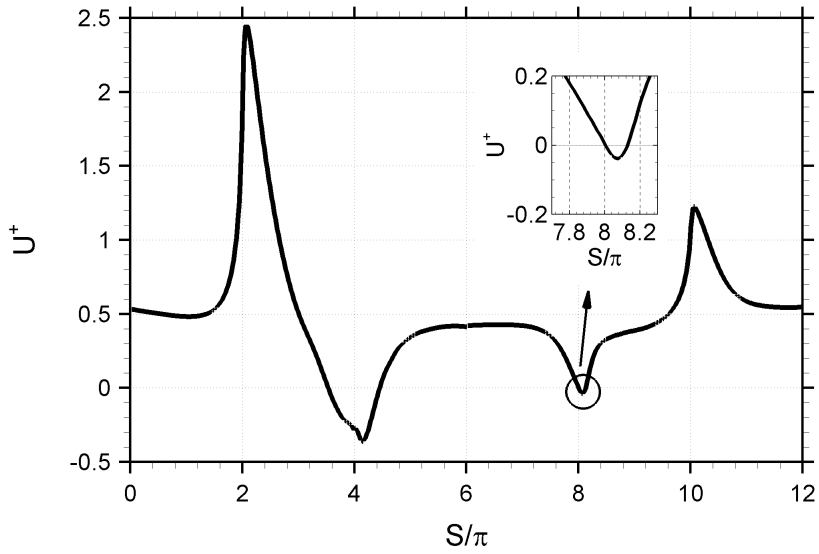

Figure 4.36 Fluid mean streamwise velocity at $\Delta y^+ = 0.47$ away from SURFACE-1.

4.7 Surface Erosion on Channel Walls

The simulation of particle motion inside the U-shaped channel was motivated by the issue of surface erosion associated with particle-wall collisions. As particles travel through the U-shaped channel, they remove material from the channel walls when they impact them. Figure 4.37 presents contour plots of erosion rate (ER-t) caused by particles of different Stokes numbers, with ER-t defined as the ratio of the mass removed from one unit area during one flow through time to the total mass of particles at each Stokes number. The mass removed by each impingement is computed using the Tulsa angle dependent model (Equations 2.44-2.45), but without the constant coefficients A and F_s.

Figure 4.37 provides an overall view of surface erosion on the channel walls. At St_b increases from 0.125 to 6.0 (plots a-h), the maximum erosion rate increases by more than two orders of magnitude. The magnitude of ER-t caused by St_b = 0.5, 2.0, 4.0, and 6.0, is delineated along SURFACE-1 in Figures 4.38-4.41, with the corresponding collision rate ($N-t$), mean incident angle (α) and mean impact velocity (V_{imp}^{+}) at $\alpha \leq 15°$ and at $\alpha > 15°$, respectively. The collision rate is defined as the number of collisions on one unit area during one flow through time divided by the total number of particles at each Stokes number. The erosion rate, however, depends not only on the collision rate but also on the incident angle and impact velocity. According to the Tulsa angle dependent model, the erosion rate exhibits different angular dependence for $\alpha \leq 15°$ and for $\alpha > 15°$. When $\alpha \leq 15°$, the erosion rate rises rapidly with the incident angle. After $\alpha = 15°$, the erosion rate increases slightly as α increases to 38°, and then drops slowly as α increases further.

At all Stokes numbers (Figures 4.38-4.41), the erosion rate at both $\alpha \leq 15°$ and $\alpha > 15°$ are the highest on the outer bend ($8.0 \leq S/\pi \leq 10.0$). At $St_b = 0.5$ (Figure 4.38), the erosion rate at $\alpha \leq 15°$ is higher at $9.0 \leq S/\pi \leq 10.0$ than at $8.0 \leq S/\pi \leq 9.0$ due to the larger incident angle and impact velocity at $9.0 \leq S/\pi \leq 10.0$. Similarly, due to the larger α and V_{imp}^{+} at $\alpha > 15°$, the erosion rate at $\alpha > 15°$ is comparable to the ER-t at $\alpha \leq 15°$ though the collision rate at $\alpha \leq 15°$ is much higher. As St_b increases from 0.5 to 6.0 (Figures 4.38-4.41), the collision rate at $\alpha > 15°$ rises but the collision rate at $\alpha \leq 15°$ lessens. Despite the decrease

of collision rate at $\alpha \leq 15°$, the erosion rate at $\alpha \leq 15°$ becomes larger with the incident angle and impact velocity as St_b increases. In contrast to the ER-t at $\alpha \leq 15°$, the erosion rate at $\alpha > 15°$ is less sensitive to the incident angle. As St_b increases from 0.5 to 6.0, the erosion caused by collisions at $\alpha > 15°$ becomes larger primarily owing to the rising collision rate at $\alpha > 15°$. As St_b increases to 2.0 (Figure 4.39), the erosion rate at $\alpha > 15°$ has become dominant on the outer bend except near the end. At $St_b = 4.0$ and 6.0 (Figures 4.40 and 4.41), the erosion caused by collisions at $\alpha \leq 15°$ is negligible in comparison to that caused by collisions at $\alpha > 15°$.

For $St_b \geq 2.0$ (Figures 4.39-4.41), the erosion rate at $\alpha > 15°$ is highest where particles from the plumes impact the outer bend at large incident angle. These particles then rebound from the outer bend and collide with it again, which results in the high erosion rate on the lower part of the outer bend ($9.0 \leq S/\pi \leq 10.0$). The simulated surface erosion on the channel walls, especially on the lower part of the outer bend, may be affected by the modeling of particle-wall collision.

Figure 4.42 compares the total erosion rate (ER-t) caused by elastic reflection with the total ER-t assuming inelastic reflection along SURFACE-1 for $St_b = 0.5$, 2.0, 4.0 and 6.0, respectively. At $St_b = 0.5$ (plot b), the difference in the erosion rate due to the modeling of particle-wall collision is negligible. For $St_b \geq 2.0$ (plots d-h), the erosion rate on the outer bend ($8.0 \leq S/\pi \leq 10.0$) is slightly lower when particle-wall collision is inelastic, but the maximum ER-t caused by elastic and inelastic reflection is almost identical. Surprisingly, the influence of particle-wall collision modeling on surface erosion is more significant in the straight section. On the upper wall ($4.0 \leq S/\pi \leq 6.0$), the erosion rate is much lower when particle-wall collision is inelastic. This is because the collisions on the upper wall are associated with the collisions on the outer bend near the exit of the curved section. When the intensity of collisions on the outer bend is reduced, the number of collisions on the upper wall diminishes and the erosion rate lessens. The influence of the collisions on the outer bend diminishes along the straight section, hence the difference in the erosion rate between elastic and inelastic reflection becomes smaller along the upper wall ($4.0 \leq S/\pi \leq 6.0$) and the lower wall ($10.0 \leq S/\pi \leq 12.0$ and $0.0 \leq S/\pi \leq 2.0$). In the curved section, the influence of particle-wall collision modeling is,

however, compromised by the curvature of the bend. After particles rebound from the outer bend, they may collide with it again and again. When the intensity of collisions is reduced, the number of collisions between particles and the outer bend increases while the incident angle and impact velocity decrease. On the whole, the erosion rate on the outer bend is only slightly lower when particle-wall collision is inelastic.

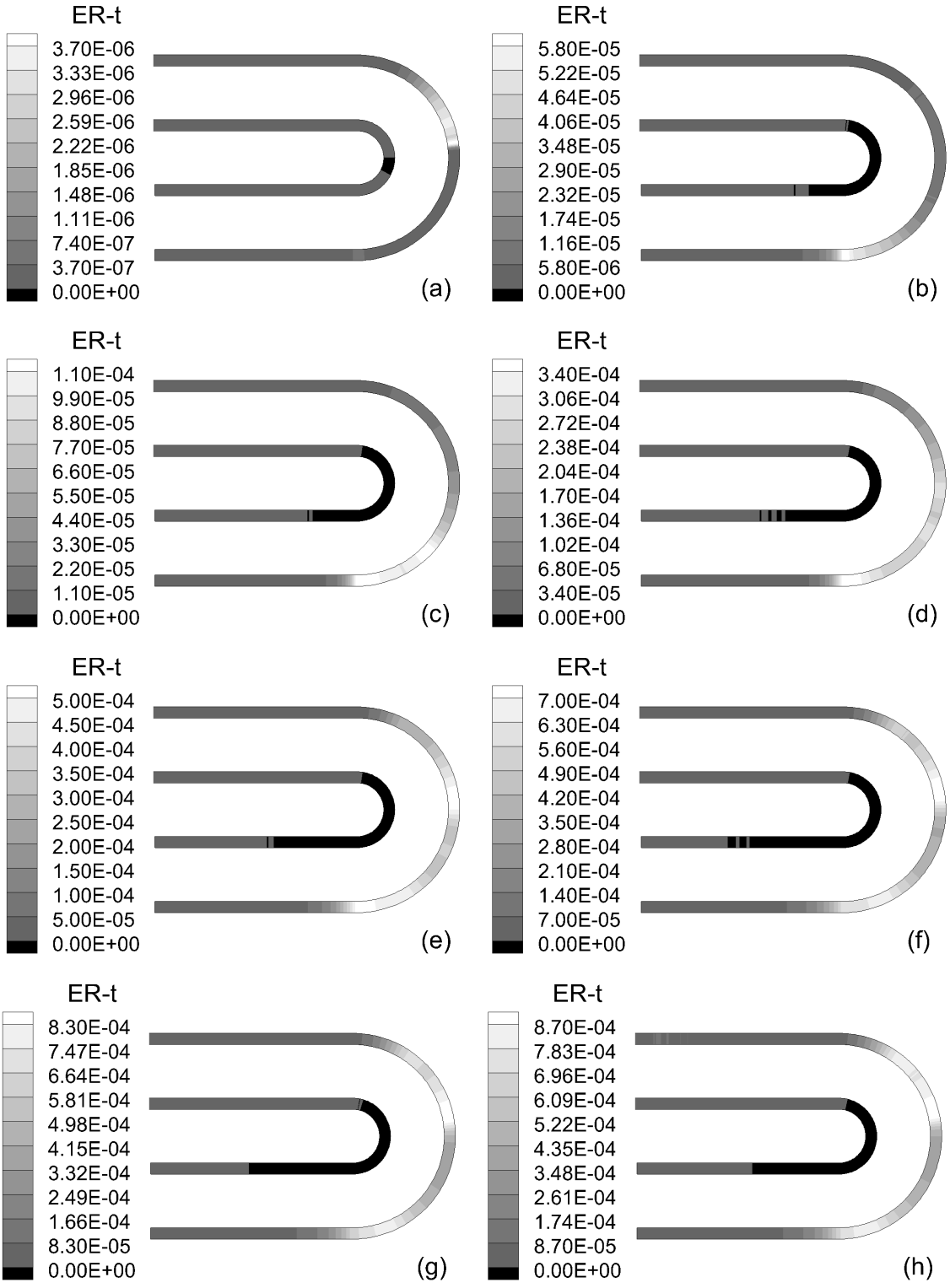

Figure 4.37 Erosion rate along the channel walls. $St_b = 0.125, 0.5, 1, 2, 3, 4, 5, 6$ (plots a-h)

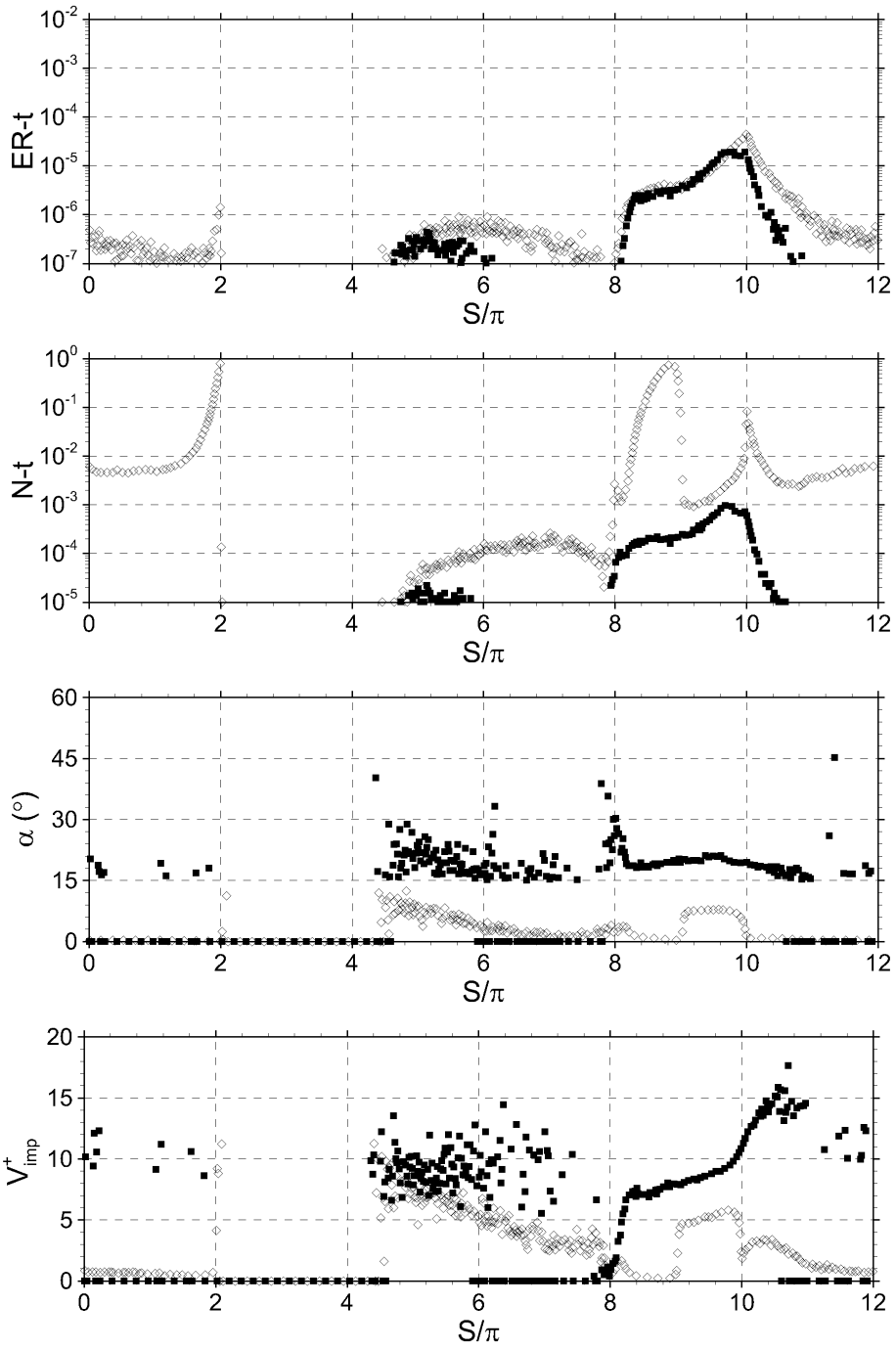

Figure 4.38 Erosion rate ($ER-t$), collision rate ($N-t$), incident angle (α) and impact velocity (V^+_{imp}) at $\alpha \leq 15°$ (diamond) and at $\alpha > 15°$ (filled square) along SURFACE-1. ($St_b = 0.5$)

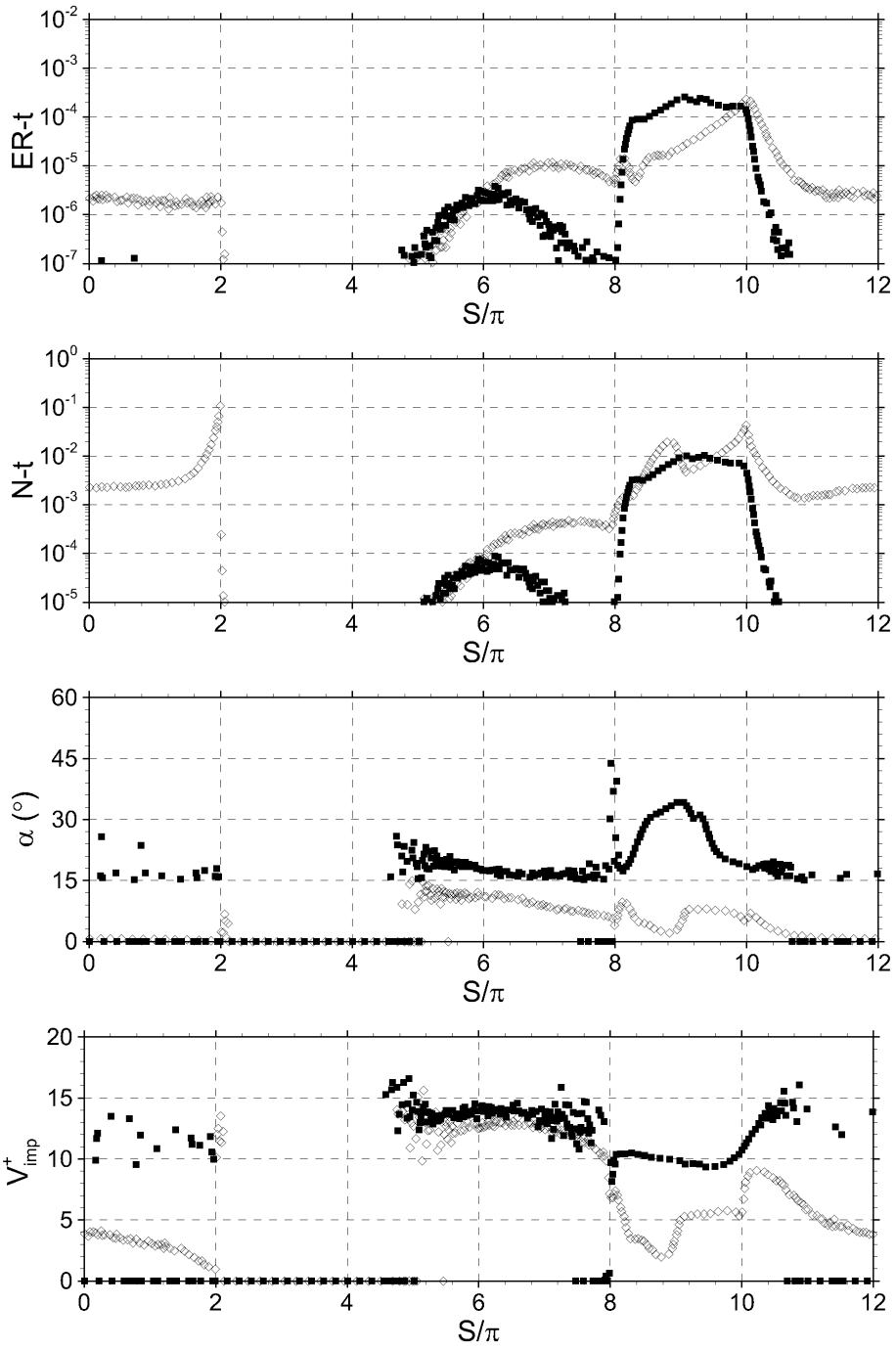

Figure 4.39 Erosion rate ($ER-t$), collision rate ($N-t$), incident angle (α) and impact velocity (V^+_{imp}) at $\alpha \leq 15°$ (diamond) and at $\alpha > 15°$ (filled square) along SURFACE-1. ($St_b = 2.0$)

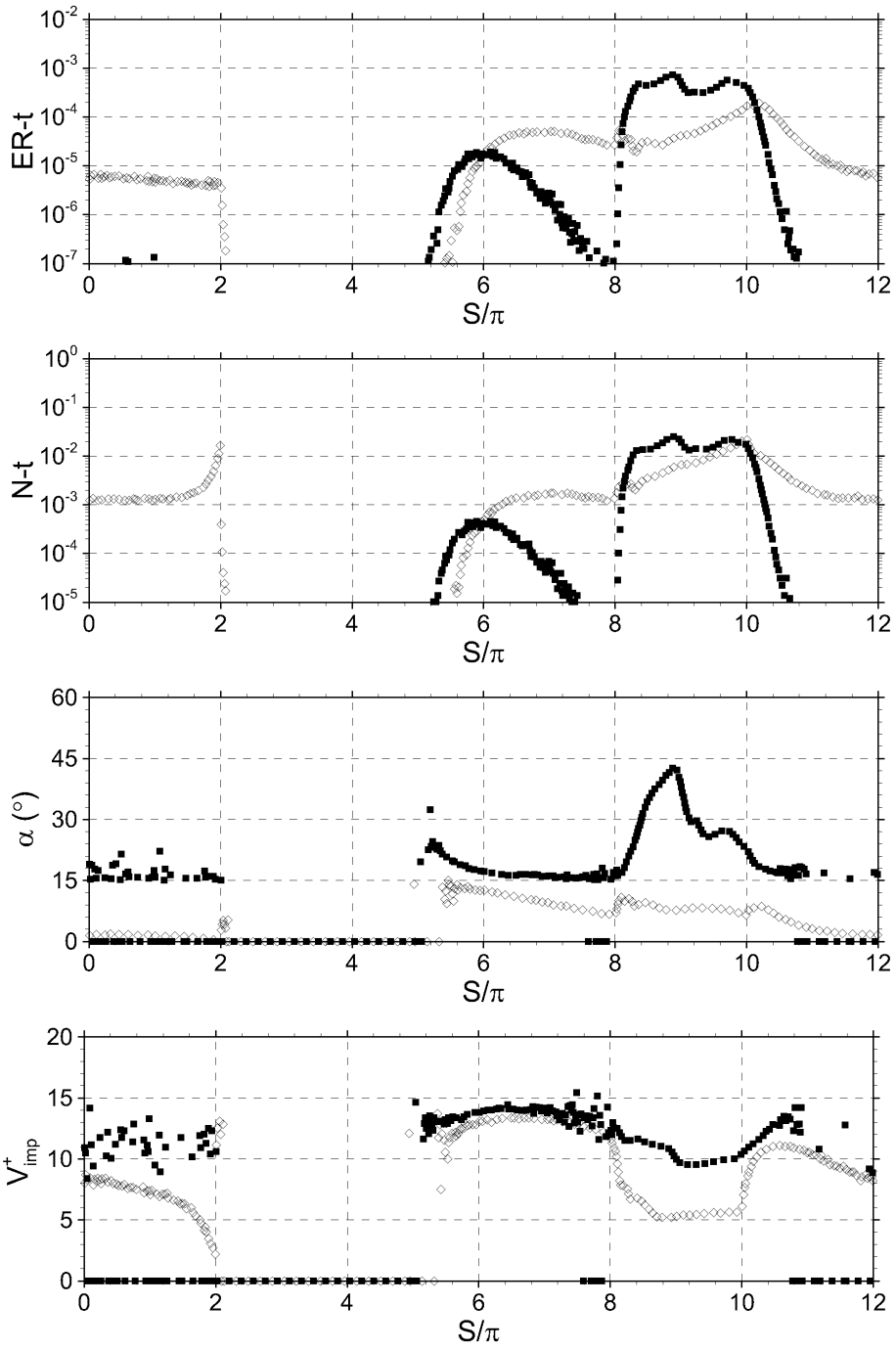

Figure 4.40 Erosion rate ($ER-t$), collision rate ($N-t$), incident angle (α) and impact velocity (V^+_{imp}) at $\alpha \leq 15°$ (diamond) and at $\alpha > 15°$ (filled square) along SURFACE-1. ($St_b = 4.0$)

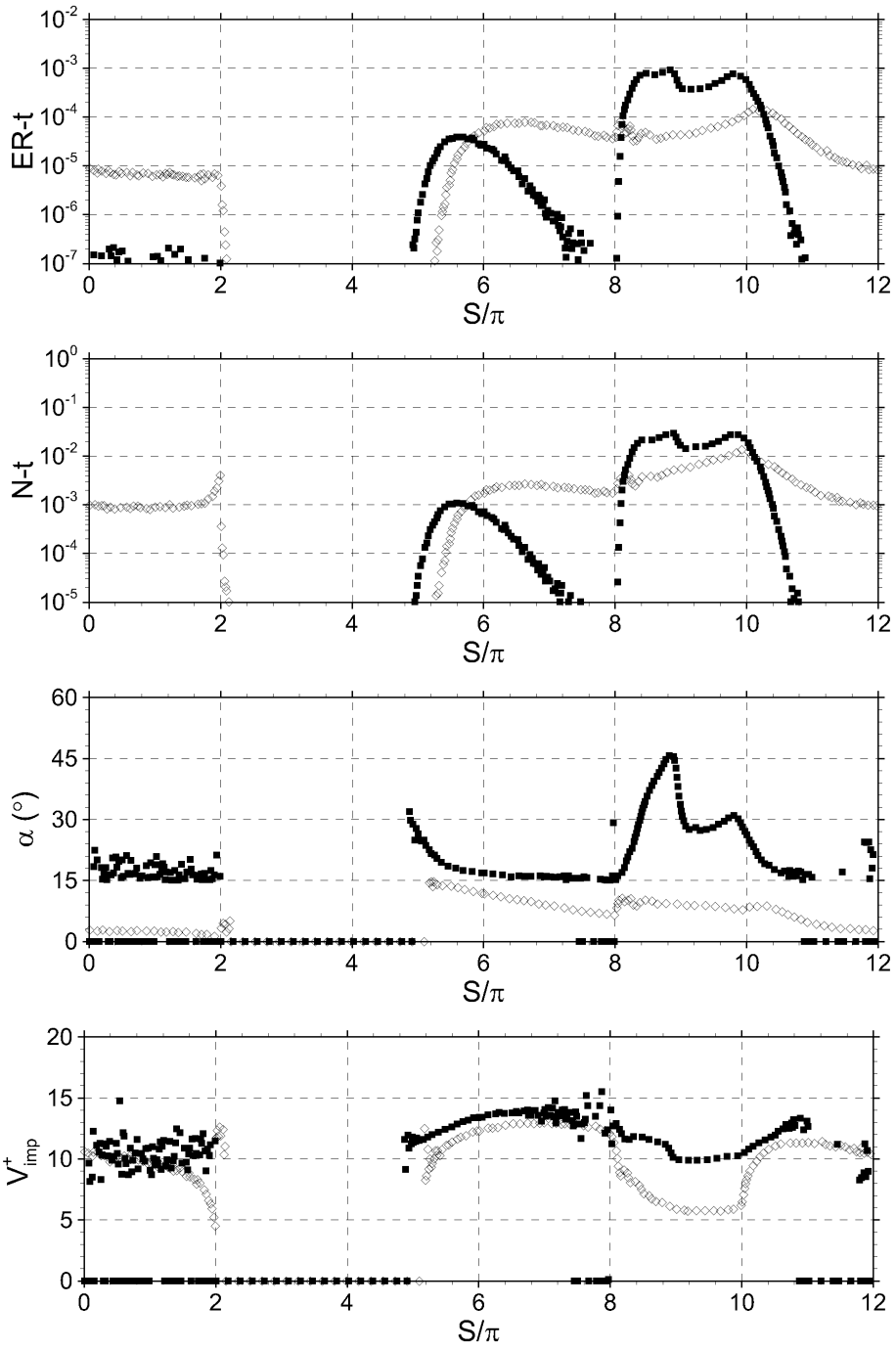

Figure 4.41 Erosion rate ($ER-t$), collision rate ($N-t$), incident angle (α) and impact velocity (V^+_{imp}) at $\alpha \leq 15°$ (diamond) and at $\alpha > 15°$ (filled square) along SURFACE-1. ($St_b = 6.0$)

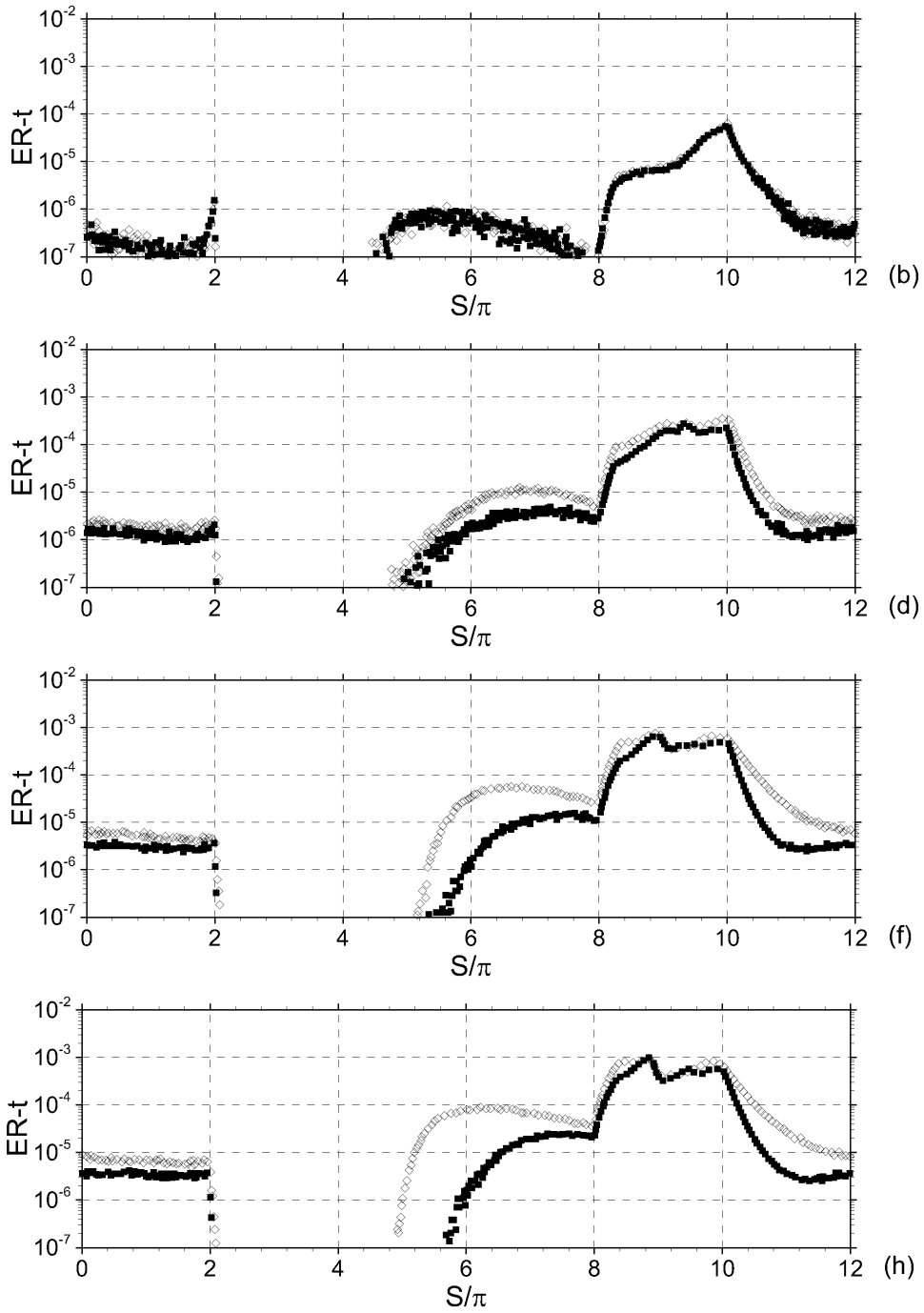

Figure 4.42 Erosion rate along SURFACE-1 assuming elastic reflection (diamond) and inelastic reflection (filled square). $St_b = 0.5, 2, 4, 6$ (plots b-h)

4.8 Particle Preferential Distribution in the Spanwise Direction

Up to this point, all the results of particle motion inside the infinite serpentine channel were presented by projecting particles onto a spanwsie cross-section ($x-y$ plane) of the U-shaped channel. The statistics were averaged both in time and in the spanwise direction. In fact, particles are not distributed randomly in the spanwise direction, as shown in Figures 4.43-4.46. In Figures 4.43-4.46, the full S-shape channel is adopted to provide a complete view of particle distribution in the straight section. For $St_b = 0.5$ and 2.0 (Figures 4.43 and 4.44), particles accumulate into streaks that spread across the span of the lower wall in the straight section, no matter whether the particle-wall collision is elastic (top plot) or inelastic (bottom plot). As St_b increases to 4.0 and 6.0 (Figures 4.45 and 4.46), no particle streaks are seen when particle-wall collision is elastic. In the case of inelastic collision, a few streaks are formed at the entrance of the straight section at both $St_b = 4.0$ and $St_b = 6.0$. At the end of the straight section, the streaky pattern is seen at $St_b = 4.0$ but not at $St_b = 6.0$.

The previous studies of particle motion in the plane channel show that particles in the viscous sublayer accumulate in the low-speed streaks, with low-speed meaning the fluid streamwise velocity is lower than the mean velocity. Figure 4.47 displays the tangential components of fluid velocity fluctuations at $y^+ = 5$ from the inner and outer walls of the U-shaped channel. Elongated structures of positive and negative streamwise velocity fluctuations are observed. Figure 4.48 is a contour plot of fluid streamwise velocity fluctuations at $y^+ = 5$ above the lower wall in the straight section. The mean velocity of the fluid is in the negative x direction, with $x/\pi = 0.0$ and -4.0 representing the entrance and exit of the straight section, respectively. In the dark grey regions, the fluid streamwise velocity is lower than the mean velocity. In Figures 4.49-4.52, particles between the lower wall and the $x-z$ plane at $y^+ = 5$ are projected onto the contour map of Figure 4.48. Only the results by assuming the inelastic particle-wall collision are presented since more particle streaks of $St = 4.0$ and 6.0 are observed in Figures 4.45 and 4.46 when particle-wall collision is inelastic. For $St_b = 0.5$ and 2.0 (Figures 4.49 and 4.50), particles adjacent to the lower wall are gathered in the low-speed regions.

For $St_b = 4.0$ and 6.0 (Figures 4.51 and 4.52), the number of particle streaks at the entrance

of the straight section is fewer than those observed in the bottom plots of Figures 4.45 and 4.46. The latter shows particle position in 3-D within the duct. This indicates that particles are clustered outside of the viscous sublayer. For $St_b = 4.0$ and 6.0, particles form puffs in the core region of the straight section, as shown in Figures 4.45 and 4.46. The two sets of vorticity contours in Figure 4.53 show that the elongated vortex structures only exist in the viscous sublayer, thus these puffs cannot be caused by the flow structures in the core region. The puffs are associated with the few particle streaks formed above the lower wall at the end of the straight section, as shown in Figures 4.51 and 4.52. When the particles in these streaks enter the curved section, they are thrown onto the outer bend by inertia. The particles then reflect from the outer bend multiple times and accumulate into puffs at the entrance of the straight section.

When particles are thrown onto the outer bend preferentially in the spanwise direction, the surface erosion caused by particle-wall collisions may be uneven across the span of the channel walls. Figures 4.54 and 4.55 present the contour plots of channel wall erosion rate averaged over 1/6 and 12 flow through times, respectively. The streaky erosion pattern is formed during 1/6 flow through times, but the surface erosion rate averaged over 12 flow through times is almost uniform in the spanwise direction. Because particle clusters in the spanwise direction vary over time with the flow, the influence of particle preferential distribution on the long-term estimation of surface erosion rate is negligible.

4.9 Summary

Particle motion in a turbulent infinite serpentine channel was simulated using direct numerical simulation coupled with Lagrangian particle tracking. Simulation results, including the surface erosion caused by particle-wall collisions, were presented and analyzed. In general, the statistics of particle motion were affected by centrifugal acceleration, turbulent diffusion, turbophoresis and particle-wall collision. The instantaneous distribution of particles was preferential in the spanwise direction, which was caused by the elongated flow structures in the viscous sublayer.

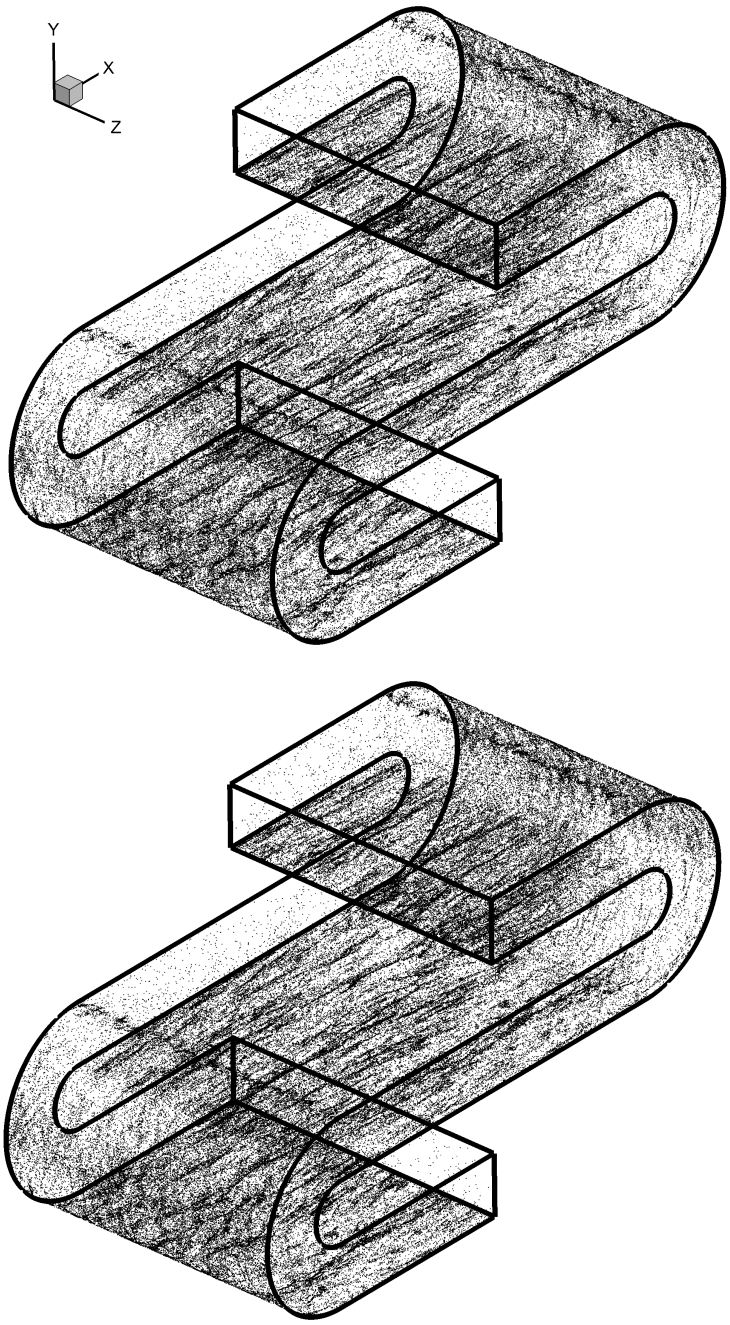

Figure 4.43 Particle instantaneous distribution inside the S-shaped channel assuming elastic (top plot) and inelastic (bottom plot) particle-wall collision. ($St_b = 0.5$)

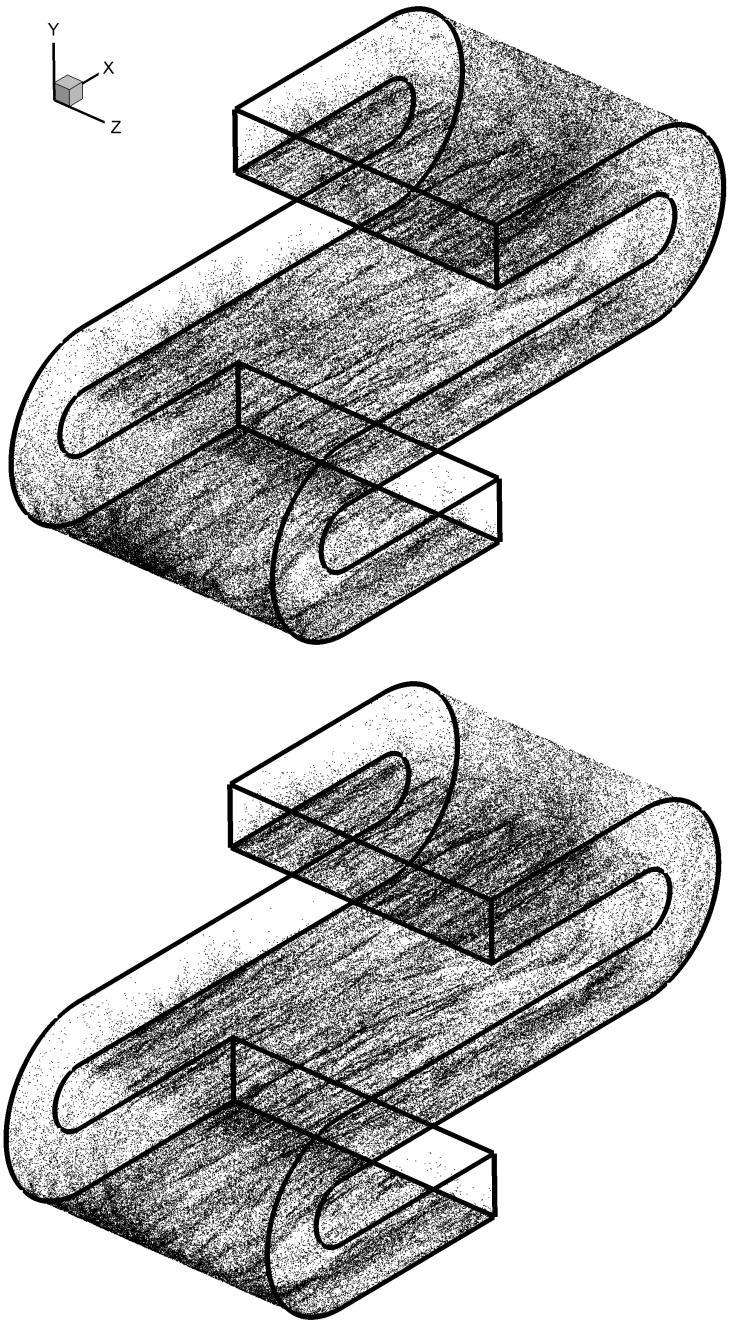

Figure 4.44 Particle instantaneous distribution inside the S-shaped channel assuming elastic (top plot) and inelastic (bottom plot) particle-wall collision. ($St_b = 2.0$)

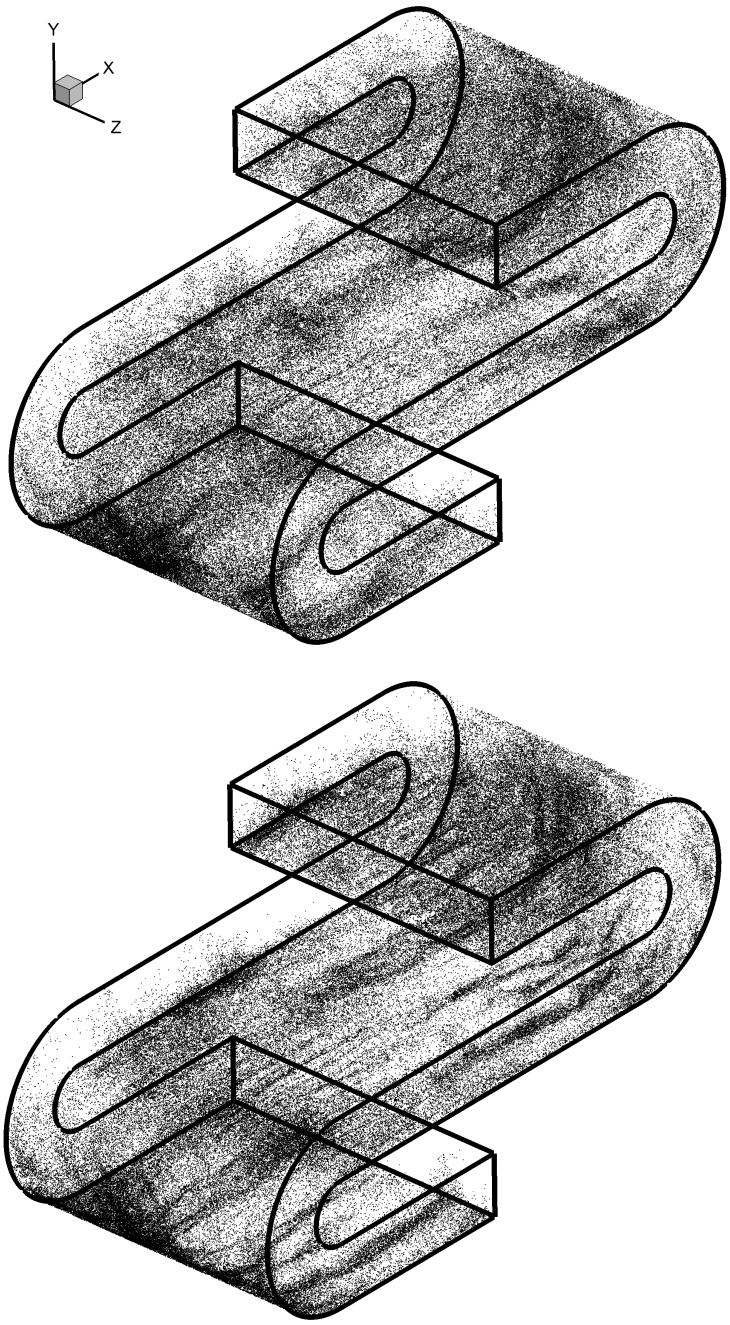

Figure 4.45 Particle instantaneous distribution inside the S-shaped channel assuming elastic (top plot) and inelastic (bottom plot) particle-wall collision. ($St_b = 4.0$)

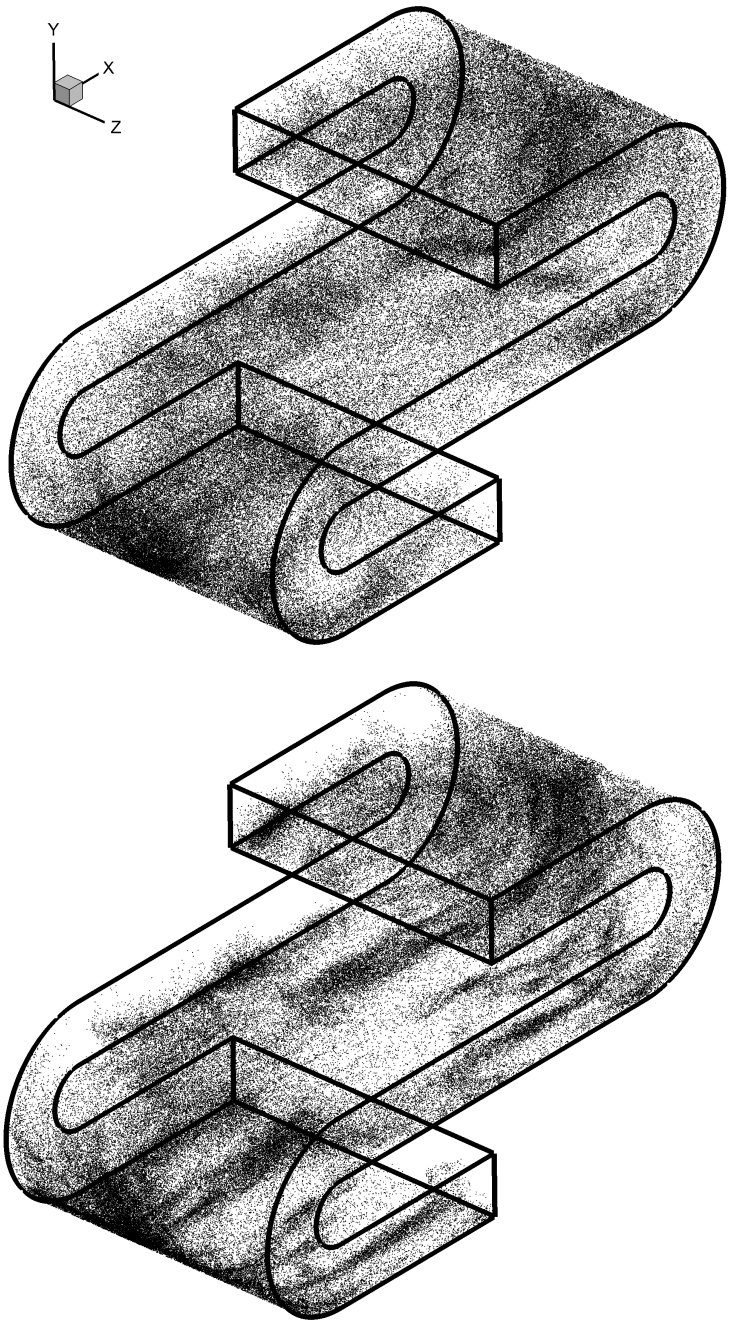

Figure 4.46 Particle instantaneous distribution inside the S-shaped channel assuming elastic (top plot) and inelastic (bottom plot) particle-wall collision. ($St_b = 6.0$)

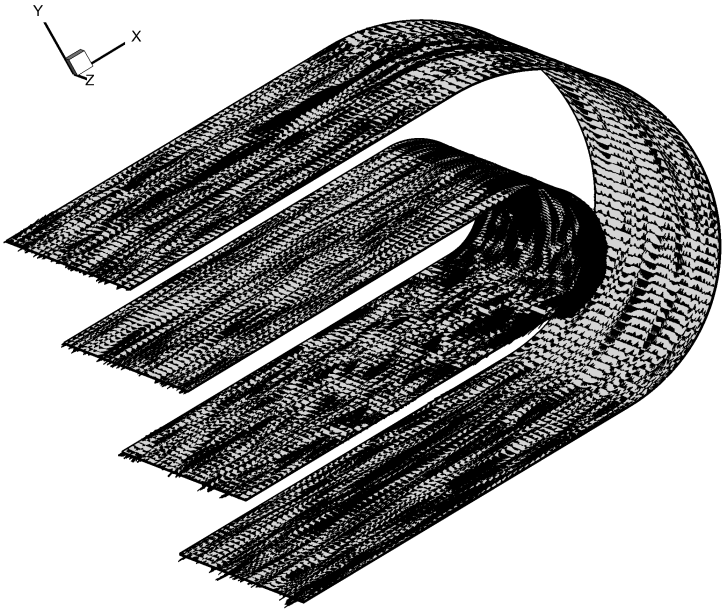

Figure 4.47 Tangential components of fluid velocity fluctuations along planes at $y^+ = 5$ from the inner and outer walls of the U-shaped channel.

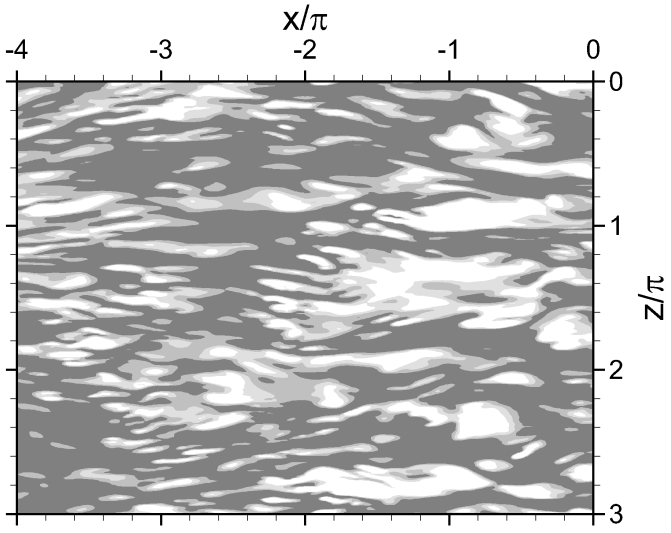

Figure 4.48 Fluid streamwise velocity fluctuations in the $x-z$ plane at $y^+ = 5$ above the lower wall in the straight section. The dark grey color represents low-speed regions.

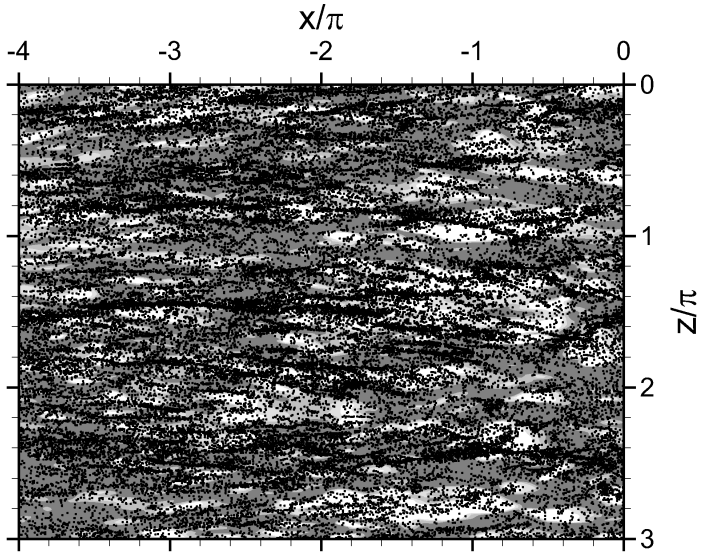

Figure 4.49 Particles in the proximity of the lower wall ($0 \leq y^+ \leq 5$) superimposed on the fluid streamwise velocity fluctuations at $y^+ = 5$ assuming inelastic particle-wall collision. ($St_b = 0.5$)

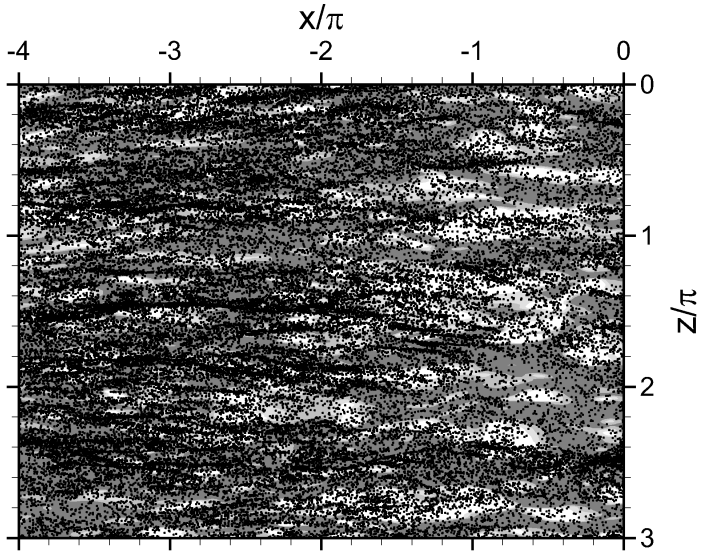

Figure 4.50 Particles in the proximity of the lower wall ($0 \leq y^+ \leq 5$) superimposed on the fluid streamwise velocity fluctuations at $y^+ = 5$ assuming inelastic particle-wall collision. ($St_b = 2.0$)

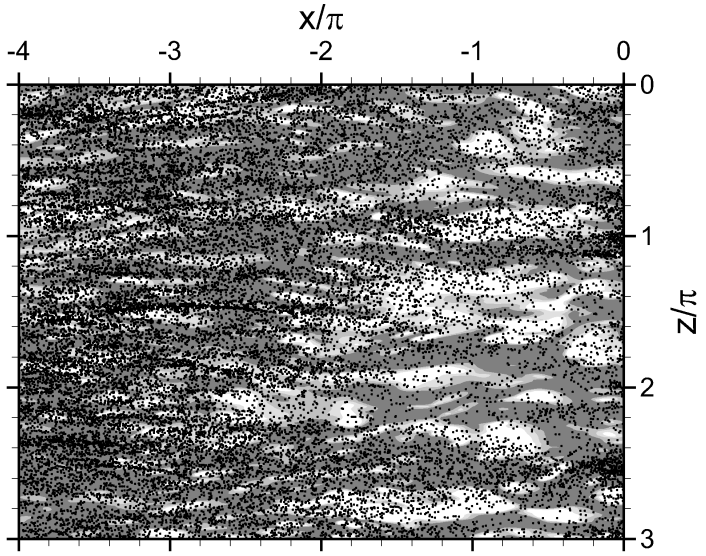

Figure 4.51 Particles in the proximity of the lower wall ($0 \leq y^+ \leq 5$) superimposed on the fluid streamwise velocity fluctuations at $y^+ = 5$ assuming inelastic particle-wall collision. ($St_b = 4.0$)

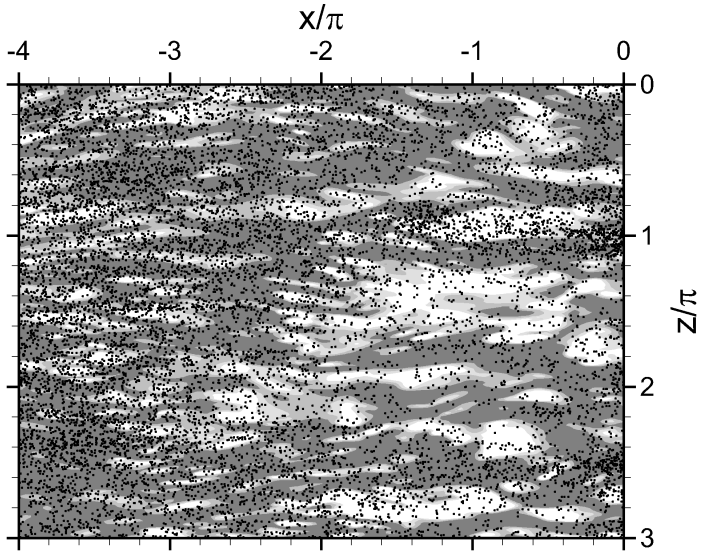

Figure 4.52 Particles in the proximity of the lower wall ($0 \leq y^+ \leq 5$) superimposed on the fluid streamwise velocity fluctuations at $y^+ = 5$ assuming inelastic particle-wall collision. ($St_b = 6.0$)

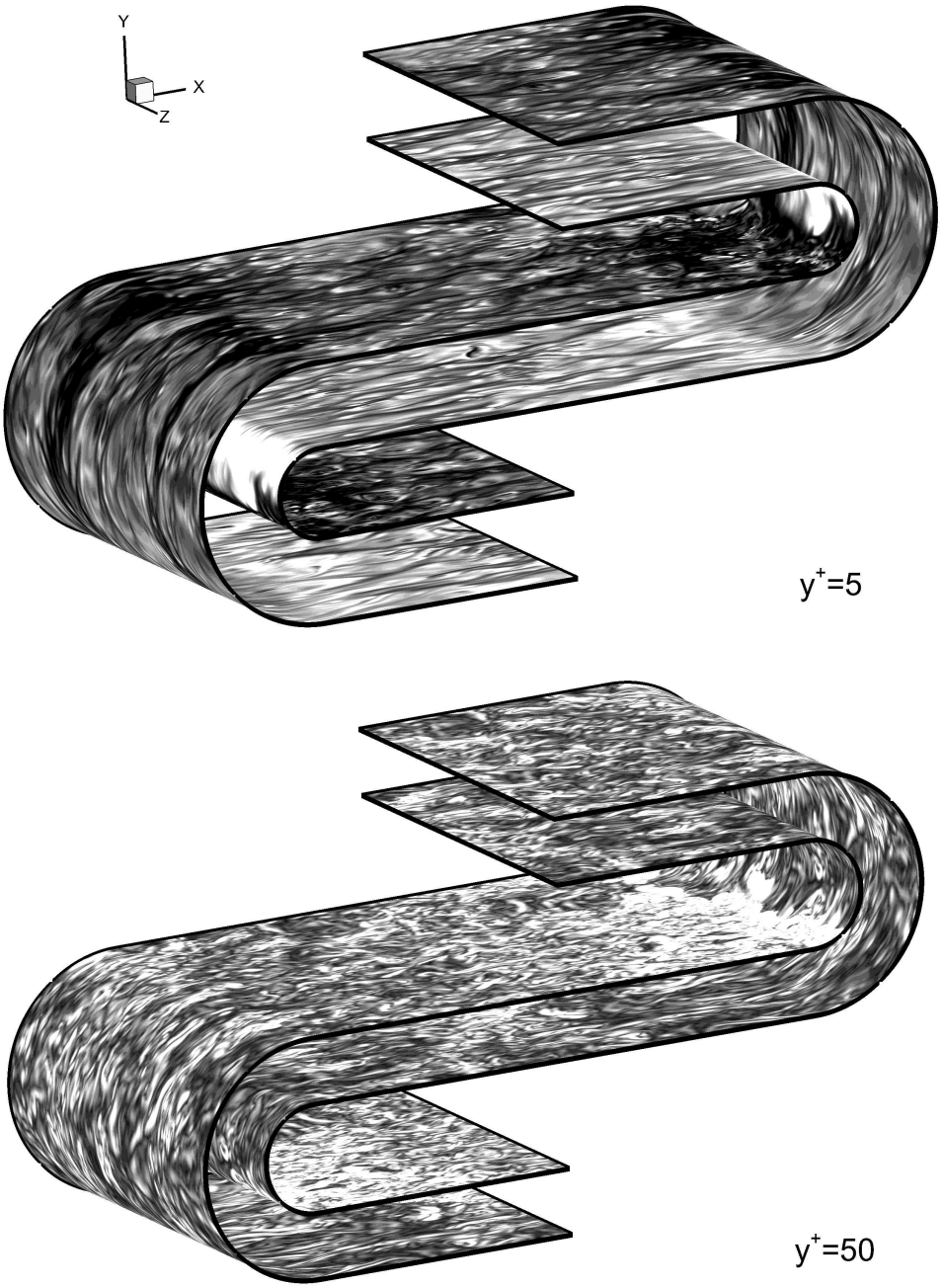

Figure 4.53 Vorticity magnitude at $y^+ = 5$ and $y^+ = 50$ from the channel walls of the S-shaped channel. The contour level is set up independently to visualize the vortex structures.

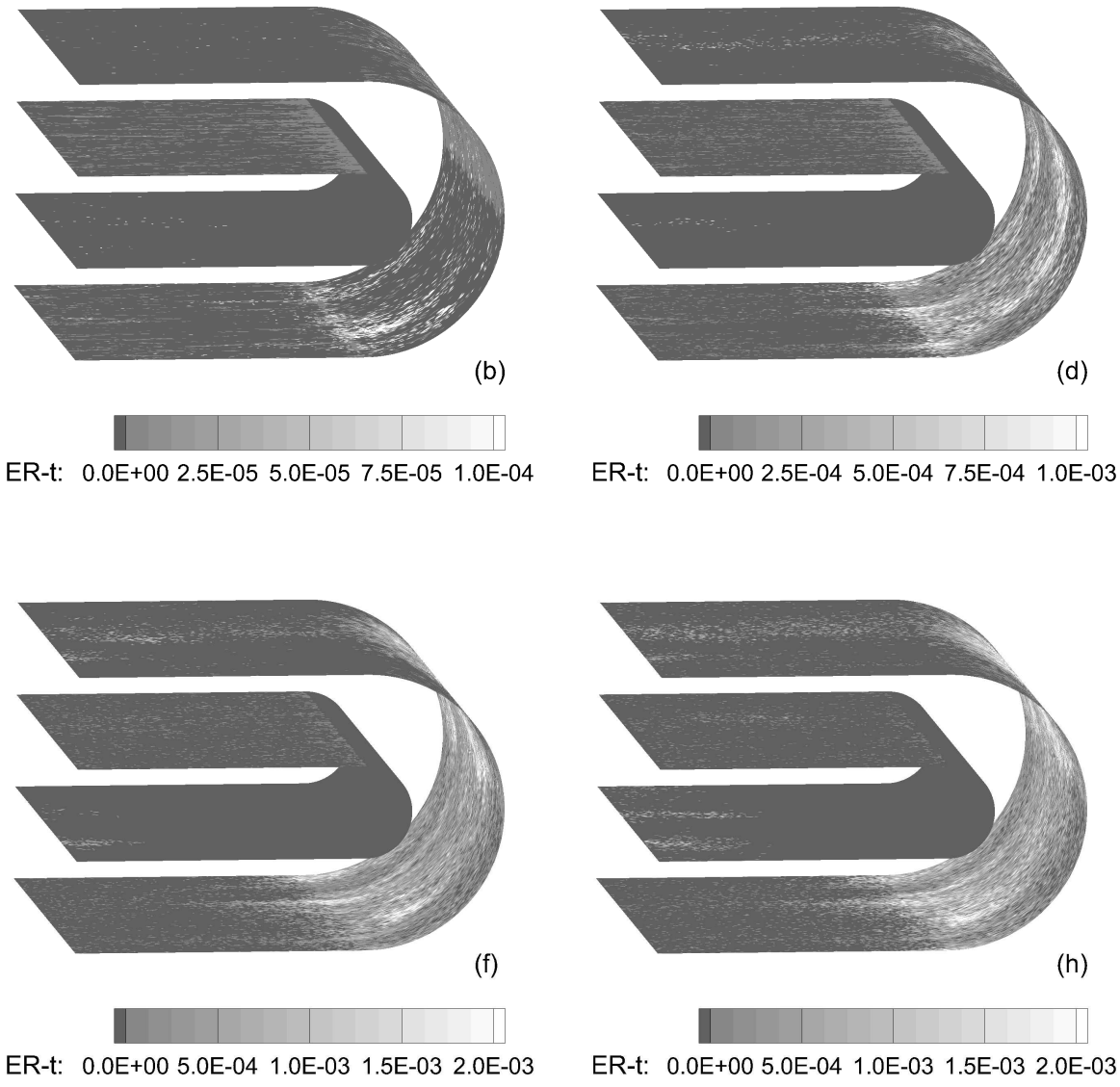

Figure 4.54 Channel wall erosion rate over 1/6 flow through times assuming elastic particle-wall collision. $St_b = 0.5, 2, 4, 6$ (plots b-h)

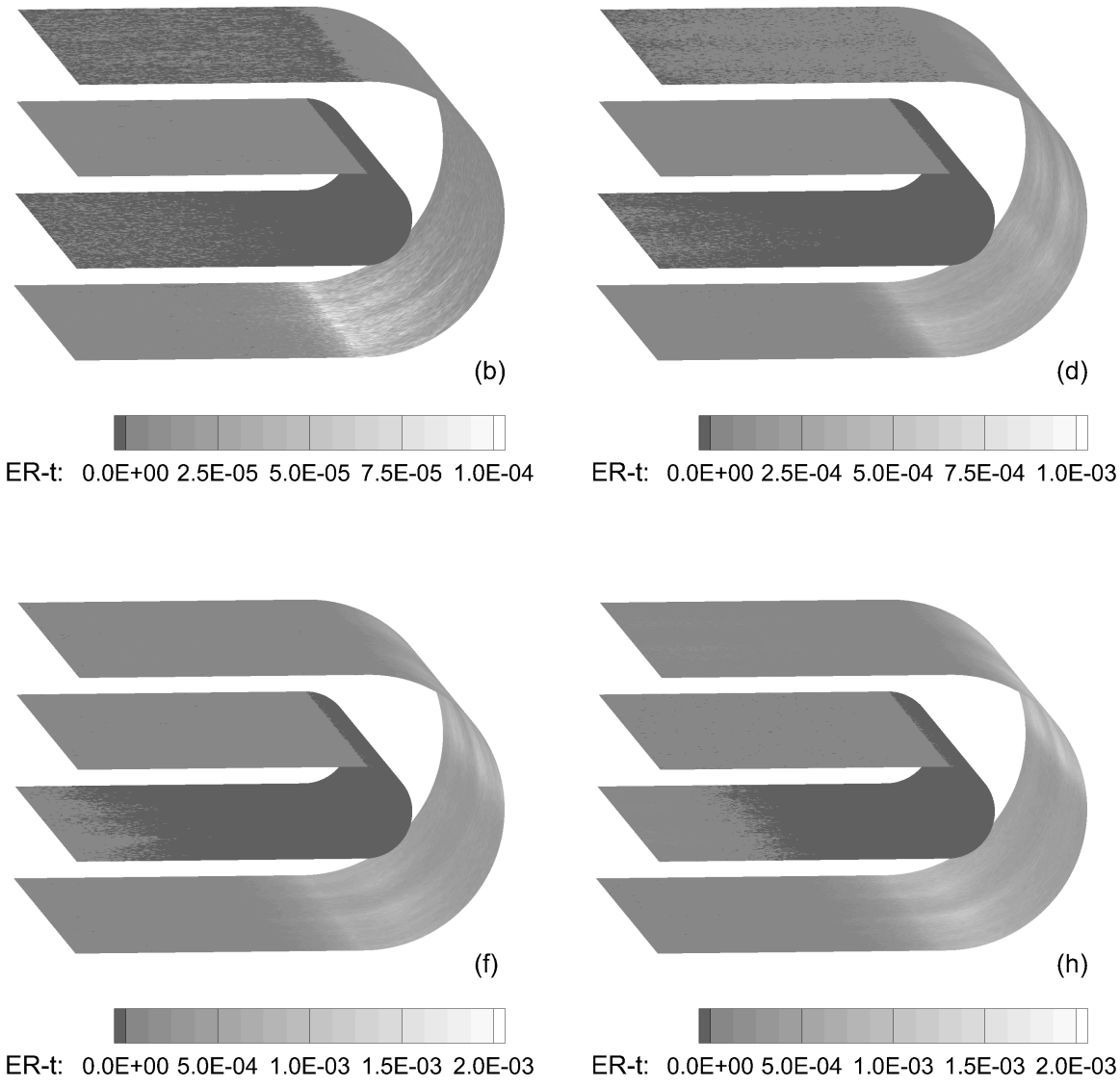

Figure 4.55 Channel wall erosion rate over 12 flow through times assuming elastic particle-wall collision. $St_b = 0.5, 2, 4, 6$ (plots b-h)

CHAPTER 5. CONCLUSION

5.1 Conclusion

In this thesis, the particulate motion in an infinite serpentine channel was studied using direct numerical simulation coupled with Lagrangian particle tracking. A pre-existing direct numerical simulation (DNS) code was modified to simulate flow in the infinite serpentine channel using a U-shaped channel. A parallel, Lagrangian particle tracking (LPT) module was developed and incorporated into the DNS code. To validate the implementation of the LPT module, a simulation of particle-laden flow in a plane channel was carried out, and the simulation results agreed well with those from an international collaboration.

Particle motion in the infinite serpentine channel without and with turbulence were simulated and compared. Without turbulence, particles accumulate onto equilibrium trajectories. Turbulence disperses particles to various degrees, depending on Stokes number. At small Stokes numbers, the influence of particle inertia is dominant. At large Stokes numbers, particle motion is affected by particle-wall collisions. In the spanwise direction, particle distribution is preferential, but it has little influence on long term surface erosion.

5.2 Suggestion on Future Work

This project is a first attempt to perform direct numerical simulation of particle-laden flows in the serpentine channel. In the current simulation, one-way coupling was assumed and only Stokes drag was included. In the future simulations, more forces (e.g. Saffman lift) can be considered and the influence of particles on the fluid can be modeled.

BIBLIOGRAPHY

Ahlert, K. (1994). Effects of particle impingement angle and surface wetting on solid particle erosion on AISI 1018 Steel. *M.S. Thesis, The University of Tulsa*.

Apte, S. V., Mahesh, K., Moin, P. and Oefelein, J. C. (2003). Large-eddy simulation of swirling particle-laden flows in a coaxial-jet combustor. *International Journal of Multiphase Flow*, *29*, 1311–1331.

Breuer, M., Baytekin, H. T. and Matida, E. A. (2006). Prediction of aerosol deposition in 90° bends using LES and an efficient Lagrangian tracking method. *Journal of Aerosol Science*, *37*, 1407–1428.

Brooke, J. W., Kontomaris, K., Hanratty, T. J. and McLaughlin, J. B. (1992). Turbulent deposition and trapping of aerosols at a wall. *Physics of Fluids A*, *4*, 825–834.

Brooke, J. W., Hanratty, T. J. and McLaughlin, J. B. (1994). Free-flight mixing and deposition of aerosols. *Physics of Fluids*, *6*, 3404–3415.

Caporaloni, M., Tampieri, F., Trombetti, F. and Vittori, O. (1975). Transfer of particles in nonisotropic air turbulence. *Journal of Atmospheric Sciences*, *32*(3), 565–568.

Chen, X., McLaury, B. S. and Shirazi, S. A. (2004). Application and experimental validation of a computational fluid dynamics (CFD)-based erosion prediction model in elbows and plugged tees. *Computers & Fluids*, *33*, 1251–1272.

Crowe, C. T., Sommerfeld, M. and Tsuji, Y. (1999). *Multiphase Flows with Droplets and Particles*. CRC Press, Boca Raton, FL

Durbin, P. A. and Pettersson Reif, B. A. (2001). *Statistical theory and modeling for turbulent flows*. John Wiley Sons.

Edwards, J. K., McLaury, B. S. and Shirazi, S. A. (2001). Solid particle erosion in elbows and plugged Tees. *Journal of Energy Resources Technology*, *123*, 277–284.

El-Behery, S. M., Hamed, M. H., Ibrahim, K. A. and El-Kadi, M. A. (2009). CFD prediction of air-solid flow in 180° curved duct. *Powder Technology*, *191*, 130–142.

Elghobashi, S. (1991). Particle-laden turbulent flows: direct simulation and closure models. *Applied Scientific Research*, *48*(3), 301–314.

Elghobashi, S. and Truesdell, G. C. (1992). Direct simulation of particle dispersion in a decaying isotropic turbulence. *Journal of Fluid Mechanics*, *242*, 655–700 .

Ferziger, J. H. and Peric, M. (2002). *Computational methods for fluid dynamics*. Springer-Verlag, 3^{rd} Edition

Fessler, J. R., Kulick, J. D. and Eaton, J. K. (1994). Preferential concentration of heavy particles in a turbulent channel flow. *Physics of Fluids*, *6*(11), 3742–3749.

Forder, A., Thew, M., and Harrison, D. (1998). A numerical investigation of solid particle erosion experienced within oilfield control valves. *Wear*, *216*, 184–193.

Guha, A. (1997). A unified Eulerian theory of turbulent deposition to smooth and rough surfaces. *Journal of Aerosol Science*, *28*, 1517–1537.

Haarlem, B. V., Boersma, B. J. and Nieuwstadt, F. T. M. (1998). Direct numerical simulation of particle deposition onto a free-slip and no-slip surface. *Physics of Fluids*, *10*(10), 2608–2620.

Hidayat, M. and Rasmuson, A. (2005). Some aspects on gas-solid flow in a U-bend: Numerical investigation. *Powder Technology*, *153*, 1–13.

Huang, L., Kumar, K., and Mujumadar, A. S. (2003). Use of computational fluid dynamics to evaluate alternative spay-dryer chamber configurations. *Drying Technology*, *21*(3), 385–412.

Kuan B., Yang W. and Schwarz, M. P. (2007). Dilute gas-solid two-phase flows in a curved 90° duct bend: CFD simulation with experimental validation. *Chemical Engineering Science*, *62*, 2068–2088.

Kuerten, J. G. M. and Vreman, A. W. (2005). Can turbophoresis be predicted by large-eddy simulation? *Physics of Fluids*, *17*, 011701.

Laskowski, G. M. (2005). Inverse design of a turbine cascade passage and DNS of a stationary and rotating serpentine passage. *PhD Thesis, Stanford University.*

Laskowski, G. M. and Durbin, P. A. (2007). Direct numerical simulations of turbulent flow through stationary rotating infinite serpentine passages. *Physics of Fluids*, *19*, 015101.

Malik, N. A. and Vassilicos, J. C. (1999). A Lagrangian model for turbulent dispersion with turbulent-like flow structure: Comparison with direct numerical simulation for two-particle statistics. *Physics of Fluids*, *11*(6), 1572–1580.

Marchioli, C. and Soldati, A. (2002). Mechanisms for particle transfer and segregation in a turbulent boundary layer. *Journal of Fluid Mechanics*, *469*, 283–315.

Marchioli, C., Giusti, A., Salvetti, M. V. and Soldati, A. (2003). Direct numerical simulation of particle wall transfer and deposition in upward turbulent pipe flow. *International Journal of Multiphase Flow*, *29*, 1017–1038.

Marchioli, C., Salvetti, M. V. and Soldati, A. (2008). Some issues concerning large-eddy simulation of inertial particle dispersion in turbulent bounded flows *Physics of Fluids*, *20*, 040603.

Marchioli, C., Soldati, A., Kuerten, J. G. M., Arcen, B., Tanière, A., Goldensoph, G., Squires, K. D., Cargnelutti, M. F. and Portela, L. M. (2008). Statistics of particle dispersion in direct numerical simulations of wall-bounded turbulence: Results of an international collaborative benchmark test. *International Journal of Multiphase Flow*, *34*, 879–893.

Maxey, M. R. (1987). The gravitational settling of aerosol particles in homogeneous turbulence and random flow fields. *Journal of Fluid Mechanics*, *174*, 441–465.

Mazur, Z., Urquiza, G., and Campos, R. (2004). Improvement of the turbine main stop valves with flow simulation in erosion by solid particle impact CFD. *International Journal of Rotating Machinery*, *10*, 65–73.

McCoy, D. D. and Hanratty, T. J. (1977). Rate of deposition of droplets in annular two-phase flow. *International Journal of Multiphase Flow*, *3*, 319–331.

McLaughlin, J. B. (1989). Aerosol particle deposition in numerically simulated channel flow. *Physics of Fluids A*, *1*, 1211–124.

Metwally, M., Tabakoof, W., and Hamed, A. (1995). Blade erosion in automotive gas turbine engine. *Journal of Engineering for Gas Turbines and Power*, *117*(1), 213–219.

Michaelides, E. E. (2006). *Particles, Bubbles and Drops–Their Motion, Heat and Mass Transfer.* World Scientific Publishing Co. Pte. Ltd.

Narayanan, C., Lakehal, D., Botto, L., and Soldati, A. (2003). Mechanisms of particle deposition in a fully-developed turbulent open channel flow. *Physics of Fluids*, *15*, 763-775.

Njobuenwu, D. O., Fairweather, M. and Yao, J. (2009). Prediction of gas-solid flows in a square duct with a 90° bend. 6th International Symposium on Turbulence, Heat and Mass Transfer. 14-18 September 2009.

Pedinotti, S., Mariotti, G. and Banerjee, S. (1992). Direct numerical simulation of particle behavior in the wall region of turbulent flows in horizontal channels. *International Journal of Multiphase Flow*, *18*, 927-941.

Picciotto, M., Marchioli, C. and Soldati, A. (2003). Characterization of near-wall accumulation regions for inertial particles in turbulent boundary layers. *Physics of Fluids*, *17*, 098101.

Rashidi, M., Hetsroni, G. and Banerjee, S. (1990). Particle-turbulence interaction in a boundary layer. *International Journal of Multiphase Flow*, *16*, 935–949.

Riley, J. J. and Patterson, G. S. (1974). Diffusion experiments with numerically integrated isotropic turbulence. *Physics of Fluids*, *17*, 292–297.

Rosenfeld, M., Kwak, D. and Vinokur, M. (1991). A fractional step solution method for the unsteady incompressible Navier-Stokes equations in generalized coordinate systems. *Journal of Computation Physics*, *Vol. 94*, 102–127.

Rouson, D. W. I. and Eaton, J. K. (2001). On the preferential concentration of solid particles in turbulent channel flow. *Journal of Fluid Mechanics*, *428*, 149–169.

Salazar, J. P. L. C., Jong, J. D., CAO, L., Woodward, S. H., Meng, H., and Collins, L. R. (2008). Experimental and numerical investigation of inertial particle clustering in isotropic turbulence. *Journal of Fluid Mechanics*, *600*, 245–256

Sardina G., Picano F., Schlatter P., Brandt L. and Casciola, C. (2011). Large scale accumulation patterns of inertial particles in wall-bounded turbulent flow. *Flow, Turbulence and Combustion (*doi:10.1007/s10494-010-9322-z), 1–14

Squires, K. D. and Eaton, J. K. (1991). Preferential concentration of particles by turbulence. *Physics of Fluids A*, *3*(5), 1169–1178.

Sundaram, S. and Collins, L. R. (1997). Collision statistics in an isotropic particle-laden turbulent suspension. Part 1. Direct numerical simulations. *Journal of Fluid Mechanics*, *335*, 75–109.

Tannehill, J. C., Anderson, D. A. and Pletcher, R. H. (1997). *Computational fluid mechanics and heat transfer*. Taylor Francis, 2^{nd} Edition

Wu, X., Squires, K. D. and Wang, Q. (1995). On extension of the fractional step method to general curvilinear coordinate system. *Numerical Hear Transfer*, *Part B 27*(2), 175–194.

Wu, X., Jacobs. R. G., Hunt, J. C. and Durbin, P. A. (1999). Simulation of boundary layer transition induced by periodically passing wakes. *Journal of Fluid Mechanics*, *281*, 193–218.

Yeung, P. K. (1994). Direct numerical simulation of two-particle relative diffusion in isotropic turbulence. *Physics of Fluids*, *6*, 3416–3428.

Yilmaz A. and Levy, E. K. (2001). Formation and dispersion of ropes in pneumatic conveying. *Powder Technology*, *114*, 168–185.

Young, J. and Leeming, A. (1997). A theory of particle deposition in turbulent pipe flow. *Journal of Fluid Mechanics*, *340*, 129–159.

Zaki, T. A. and Durbin, P. A. (2005). Mode interaction and the bypass route to transition. *Journal of Fluid Mechanics*, *531*, 85–111.